

The Paleoredox Context of the McArthur and Birrindudu Basins, Northern Territory, Australia

Le contexte rédox des bassins McArthur et Birrindudu, territoire du Nord,
Australie

Margaret Whelan

Master of Science
August 2022

Earth and Planetary Sciences

McGill University
Montréal, Québec

A thesis submitted to McGill University in partial fulfillment of the requirements of the degree of
Master of Science

© Margaret Whelan 2022

Acknowledgments

My primary source of support for this project was my supervisor, Galen Halverson, who provided me the funding, guidance, and encouragement necessary to complete this research among countless other opportunities. I would also like to thank Maxwell Lechte for his invaluable knowledge and incredible patience when answering my seemingly infinite number of questions. Furthermore, I would like to thank Thi Hao Bui for her instruction and counsel regarding laboratory analyses including iron speciation and total organic carbon. Thank you as well to Leigh Anne Riedman for providing me the samples analysed in this study when it was not possible to collect my own. Thank you to Marcus Kunzmann, Sam Carruthers, and Catherine Ross for the outline of this document. Lastly, thank you to the Precambrian Research Office and Publican Society (Maxwell Lechte, Angelo Dos Santos Jr., Charlotte Spruzen, Wilder Greenman, Pascal Daoust, Ajani Bissick, and William Wong) as well as the faculty, staff, and students of the department of Earth and Planetary Sciences at McGill for maintaining a safe and healthy work environment.

Contents

Contribution of authors	1
1 Middle Proterozoic Earth History	2
1.1 Introduction	2
1.2 The Middle Proterozoic (ca. 1.8 – 0.8 Ga) Environment	6
1.2.1 The Carbon Isotope Record	7
1.2.2 Low Oxygen Atmosphere	10
1.3 Proxies for Ancient Marine Chemistry	12
1.4 The Appearance of Eukaryotes	14
1.5 The Greater McArthur Basin	16
1.5.1 The McArthur Basin	18
1.5.2 The Birrindudu Basin	25
2 Geochemical Contributions and Discussion	31
2.1 Introduction	31
2.2 Methods	32
2.2.1 Sampling	32
2.2.2 Sequential Iron Extraction	32
2.2.3 Reduced Inorganic Sulfur Determination	34
2.2.4 Total Organic Carbon Content	35
2.2.5 Major Element Geochemistry	36
2.3 Results	36
2.3.1 Sedimentary Geochemistry of the Greater McArthur Basin	36
2.3.2 Major and Trace Element Distributions	44
2.3.3 Trace Metal Enrichment Factors	47
2.3.4 Chemical Index of Alteration	48
2.4 Interpretations and Discussion	49
2.4.1 Redox Structure of the Greater McArthur Basin	49
2.4.2 Local Controls on Iron Enrichment	52
2.4.3 Total Organic Carbon Content and Fossil Preservation	53
2.5 Conclusions	54
References	55

Appendices	66
Appendices	66
A Raw Data: Iron Speciation and Total Organic Carbon Content	67
B Raw Data: Major Element Geochemistry	71
C Correlation of Major Elements	76

List of Tables

A1	Total organic carbon, raw iron speciation data, and calculations recorded in weight % for drill core GSD7 from the McArthur Basin.	67
A2	Total organic carbon, raw iron speciation data, and calculations recorded in weight % for drill core MCDD0003 from the McArthur Basin.	67
A3	Total organic carbon, raw iron speciation data, and calculations recorded in weight % for drill core MCDD0005 from the McArthur Basin.	68
A4	Total organic carbon, raw iron speciation data, and calculations recorded in weight % for drill core McA5 from the McArthur Basin.	68
A5	Total organic carbon, raw iron speciation data, and calculations recorded in weight % for drill core Broughton-1 from the McArthur Basin.	69
A6	Total organic carbon, raw iron speciation data, and calculations recorded in weight % for drill core DD90VRB2 from the Birrindudu Basin.	69
A7	Total organic carbon, raw iron speciation data, and calculations recorded in weight % for drill core DD90VRB1 from the Birrindudu Basin.	70
A8	Total organic carbon, raw iron speciation data, and calculations recorded in weight % for drill core 99VRNTGSDD2 from the Birrindudu Basin.	70
A9	Internal replicates underwent identical sequential extraction of highly reactive iron and were analyzed alongside every sample batch. A summary of the weight percent iron at every step of extraction is shown above. Ext. 1 is the Acetate extraction of iron-carbonates, Ext. 2 represents the dithionite extraction of iron-oxides, and Ext. 3 is the extraction of iron in magnetite via oxalate. The average, standard deviation, percent standard deviation, and standard error of the mean are also shown.	70
A10	Major element geochemistry recorded in weight % for drill core GSD7 from the McArthur Basin.	71
A11	Major element geochemistry recorded in weight % for drill core MCDD0003 from the McArthur Basin.	71
A12	Major element geochemistry recorded in weight % for drill core MCDD0005 from the McArthur Basin.	72
A13	Major element geochemistry recorded in weight % for drill core McA5 from the McArthur Basin.	72
A14	Major element geochemistry recorded in weight % for drill core Broughton-1 from the McArthur Basin.	73

A15	Major element geochemistry recorded in weight % for drill core DD90VRB2 from the Birrindudu Basin.	73
A16	Major element geochemistry recorded in weight % for drill core DD90VRB1 from the Birrindudu Basin.	73
A17	Major element geochemistry recorded in weight % for drill core 99VRNTGSDD2 from the Birrindudu Basin.	74
A18	Reference materials and sample duplicates with associated % error for major element geochemical analyses.	75
A19	Correlation coefficients of major element oxides as well as highly reactive iron ratios and TOC for the entire Greater McArthur Basin.	76

List of Figures

1.1	The proposed timeline for eukaryogenesis as it relates to the defining events of the middle Proterozoic and the Greater McArthur Basin stratigraphy. Evolution of atmospheric oxygen is shown in relation to dated formations within the McArthur Basin while geochemical evolution of the ocean and associated evolutionary milestones as revealed by the fossil record are outlined in colour. The sampled interval pertaining to Chapter 2 of this study is also outlined in black.	3
1.2	Geologic map of modern Australia showing the current distribution of the 5 Archean cratons bounded by the dashed green lines that formed part of the Nuna supercontinent. The location of the correlative McArthur and Birrindudu Basins (and other early Proterozoic Basins) is shown in orange overlying the Northern Australian Craton. Map modified from (Ahmad et al., 2013).	5
1.3	Compilation of carbon isotope measurements from Proterozoic basins around the world. Major concomitant orogenic events are indicated by the black bars (Nag = Nagssugtoqidian; Trans-Hud = Trans-Hudson) while the average zircon population in 10 Myr bins is shown by the black line. The proposed rise in $\delta^{13}\text{C}$ values around 1900 Ma is hypothesized to be the result of peak accretionary orogenesis following the deposition of the Rowatt Formation in Northern Canada. There are no additional fluctuations around 0‰ during this 650 Myr timespan. Figure and caption adapted from Hodgskiss et al. (2019b).	9
1.4	Evolution of atmospheric oxygen throughout the Proterozoic from Lyons et al. (2014). The red curve indicates the standard two-step increase in oxygen during the Great Oxidation Event (GOE) and subsequent Neoproterozoic Oxygenation Event (NOE). The blue curve shows the emerging view of an oxygen overshoot and subsequent return to low oxygen values until the NOE.	11
1.5	Proposed model for Proterozoic ocean chemistry. Adapted from Lyons et al. (2021).	14

1.6	Schematic phylogenetic tree showing the evolution of the first eukaryotic common ancestor (FECA) to the last eukaryotic common ancestor (LECA). Branches labelled X represent now extinct clades which include the majority of the early Proterozoic fossil record including acritarchs as well as organic-walled microfossils. Photographs using transmitted light spectroscopy of the oldest known occurrence of these fossils are shown on the right with scale bars = 20 μm (Javaux and Lepot, 2018; Lamb et al., 2009). These cyst-like, rigid specimens are specifically from the 1800 Ma Changzhongou Formation (lowermost Changcheng Group) in the Pangjiapu Region of North China (Javaux and Lepot, 2018; Lamb et al., 2009). Similar structures have been identified in the roughly 1600 Ma McArthur Group in Northern Territory, Australia.	15
1.7	Simplified geologic map of the Greater McArthur Basin featuring the chronostratigraphically correlated McArthur and Limbunya Groups as well as major faults outlined in black. Adapted from Kunzmann et al. (2019) and Munson et al. (2020).	17
1.8	Stratigraphy of the correlative McArthur and Birrindudu Basins. Geochronological data (interpreted SHRIMP U-Pb zircon ages from various interbedded volcanics) for the Tawallah, McArthur, Nathan, and Roper Groups from Page et al. (2000) and Jackson et al. (1999). Minimum Re-Os age for the Velkerri Formation of the Roper Group from Kendall et al. (2009). SHRIMP U-Pb age of a single zircon in the Campbell Spring Dolostone from Cutovinos et al. (2002). Interpreted CA-IDTIMS U-Pb zircon age from the chronostratigraphically correlated the Fraynes Formation from Munson et al. (2020). SHRIMP U-Pb detrital zircon age of the Neave Formation from Carson (2010).	19
2.1	Simplified geologic map of the southern McArthur Basin emphasizing the major stratigraphic groups and the location of the drillcores (red points) sampled in this study. Major mapped faults are outlined in black while the black points represent nearby towns. Adapted from Ahmad et al. (2013) and Rawlings (1999).	33
2.2	Simplified geologic map of the Birrindudu Basin showing the major stratigraphic groups and the location of the drillcores (red points) sampled in this study. Mapped faults are outlined in black while inferred faults are denoted using dashed black lines. Adapted from Ahmad et al. (2013).	33
2.3	Redox proxy data and TOC of the drillhole GSD7 from the McArthur Basin spanning the middle Tawallah Group. Plots from left to right: highly reactive iron over total iron, pyrite iron over highly reactive iron, total iron over aluminum, total iron, total manganese normalized to aluminum, total phosphorous, and weight percent TOC. Dashed lines represent baseline values of 0.22 and 0.38 for Fe_{HR}/Fe_T , 0.5 for Fe_T/Al , and 0.8 for Fe_{Py}/Fe_{HR} . Depositional environments are overlain on each plot with colour references included in the stratigraphy legend on the right. Note x-axis scale relative to other sections.	38
2.4	Redox proxy data and TOC of the drillhole MCDD0003 from the McArthur Basin spanning the upper-middle Tawallah Group. Stratigraphic section adapted from Kunzmann et al. (2020). Legend as in Figure 2.3.	38
2.5	Redox proxy data and TOC of the drillhole MCDD0005 from the McArthur Basin spanning the lower and middle Umbolooga Subgroup of the lower McArthur Group. Stratigraphic section adapted from Kunzmann et al. (2020). Legend as in Figure 2.3.	39

2.6	Redox proxy data and TOC of the drillhole McA5 from the McArthur Basin spanning the Barney Creek Formation of the upper McArthur Group. Stratigraphic section adapted from Schmid (2016). Legend as in Figure 2.3. Note x-axis scale increase in the column representing Mn/Al.	40
2.7	Redox proxy data and TOC of the drillhole Broughton-1 from the McArthur Basin spanning the lower Roper Group. Legend as in Figure 2.3.	42
2.8	Redox proxy data and TOC of the drillhole DD90VRB2 from the Birrindudu Basin spanning the lower Limbunya Group. Legend as in Figure 2.3.	43
2.9	Redox proxy data and TOC of the drillhole DD90VRB1 from the Birrindudu Basin spanning the upper Limbunya Group. Legend as in Figure 2.3.	43
2.10	Redox proxy data and TOC of the drillhole 99VRNTGSDD2 from the Birrindudu Basin spanning the upper Bullita and lower Tijnuna Groups. Stratigraphic section adapted from Cutovinos et al. (2002). Legend as in Figure 2.3.	44
2.11	Ternary diagrams showing the relative abundances of (A) Al ₂ O ₃ , SiO ₂ , CaO, and (B) Al ₂ O ₃ , CaO, MgO in shales from the Greater McArthur Basin.	45
2.12	Cross plots displaying covariation between <i>FeHR/FeT</i> and (A) TOC; (B) Al ₂ O ₃ ; (C) CaO; (D) TiO ₂ and Al ₂ O ₃ and (E) K ₂ O; (F) TiO ₂ for all eight drillcores. Major element oxides and TOC are measured in weight % while <i>FeHR/FeT</i> is unitless. . .	46
2.13	Cross plots displaying covariation between MnO and (A) MgO; (B) CaO; (C) Fe ₂ O ₃ for all eight drillcores. All values are in weight %.	47
2.14	Average enrichment factors for selected redox sensitive elements for each drillcore. . .	49
2.15	Average CIA of each drillcore.	49
2.16	Interpretation of paleoredox environments in terms of the relative abundances of FeHR/FeT and FePy/FeHR. Triangles represent nearshore samples (supratidal to intertidal), square symbols show intertidal to subtidal facies, and circles indicate subtidal to offshore.	51

The c.a. 1.75 — 1.3 Ga Greater McArthur Basin of the Northern Australian Craton comprises multiple Proterozoic sedimentary basins in Northern Territory, Australia. The well-preserved, mixed carbonate–siliciclastic successions record deposition in a range of marine depositional environments from supratidal to offshore settings and host some of the oldest putative eukaryotic microfossils. In order to investigate the possible relationship between the interpreted paleoredox conditions of the depositional environment and the preserved microfossil assemblage, we present iron speciation data, total organic carbon content, and major element geochemistry for 194 samples across 8 cored drill holes and 19 sedimentary formations from the McArthur and Birrindudu basins. Paleoredox conditions can be inferred using iron speciation analysis, which indicates deposition in a range of anoxic (ferruginous or euxinic) to oxic marine paleoenvironments, consistent with the emerging model for redox stratified basins during the middle Proterozoic (i.e. ca. 1.8–0.8 Ga). In addition to expanding our knowledge of the early and middle Proterozoic oceans, this study explores the relationship between these paleoredox data and the environment in which the eukaryotic fossils were living at the time the rocks were deposited. This study provides an example of how performing high resolution geochemical analyses on the same rock samples known to contain microfossils can elucidate our understanding of the habitats of early eukaryotic life.

La c.a. 1,75 — 1,3 Ga bassin du Grand McArthur du craton du nord de l’Australie comprend plusieurs bassins sédimentaires protérozoïques dans le Territoire du Nord, en Australie. Les successions mixtes carbonates-silicylastiques bien conservées enregistrent des dépôts dans une gamme d’environnements de dépôt marins allant des milieux supratidaux aux milieux extracôtiers et abritent certains des microfossiles eucaryotes putatifs les plus anciens. Afin d’étudier la relation possible entre les conditions paléorédox interprétées de l’environnement de dépôt et l’assemblage de microfossiles préservés, nous présentons des données sur la spéciation du fer, la teneur totale en carbone organique et la géochimie des éléments majeurs pour 194 échantillons dans 8 trous de forage carottés et 19 formations sédimentaires de les bassins McArthur et Birrindudu. Les conditions paléorédoxes peuvent être déduites à l’aide d’une analyse de spéciation du fer, qui indique un dépôt dans une gamme de paléoenvironnements marins anoxiques (ferrugineux ou euxiniques) à oxiques, conformément au modèle émergent pour les bassins stratifiés redox au cours du Protérozoïque moyen. En plus d’élargir nos connaissances sur les océans du Protérozoïque ancien et moyen, cette étude analyse la relation entre ces données paléorédoxes et l’environnement dans lequel vivaient les fossiles eucaryotes au moment du dépôt des roches. Cette étude fournit un exemple de la façon dont l’exécution d’analyses géochimiques à haute résolution sur les mêmes échantillons de roche connus pour contenir des microfossiles peut élucider notre compréhension des habitats de la vie eucaryote précoce.

Contribution of authors

This document was written in full by Margaret Whelan, and edited by Galen Halverson and Maxwell Lechte. All analyses and interpretations in this thesis were completed by Margaret under the supervision of Thi Hao Bui at McGill University with the exception of XRF analyses performed by Activation Laboratories Ltd. in Ancaster, Ontario. Rock samples were provided by Dr. Leigh Anne Riedman of UC Santa Barbara.

Middle Proterozoic Earth History

1.1. Introduction

The Mesoproterozoic Era (1600 – 1000 Ma) featured the evolution of two supercontinents; Nuna and Rodinia. Even so, this 600 million years of Earth’s history is often overshadowed by the more ostensibly dynamic Paleoproterozoic (2500 – 1600 Ma) and Neoproterozoic (1000 – 541 Ma) eras, known for their series of glaciations, some global in extent, and a pair of oxygenation events (Lyons et al., 2014). By contrast, the Mesoproterozoic Era is known for its apparent environmental stasis. This long interval of repose began with the cessation of deposition of voluminous iron formation ca. 1800 Ma and abruptly concluded with an increase in biogeochemical instability and eukaryotic diversification ca. 800 Ma. This one billion years of Earth’s middle history is widely referred to as the “boring billion” (Brasier and Lindsay, 1998; Buick et al., 1995; Cox et al., 2016; Crockford et al., 2019; Lyons et al., 2014). Due in part to the more limited evidence of major paleoenvironmental fluctuations and transitions, this interval, hereafter referred to as the *middle Proterozoic*, remains relatively understudied. However, the importance of the middle Proterozoic in the long-term evolution of Earth’s environment is being reassessed with respect to the fundamental shifts in the biosphere that occurred during this time (Butterfield, 2015; Zhang et al., 2018). For example, it is becoming increasingly accepted that while stem group eukaryotes likely predate the Mesoproterozoic Era,

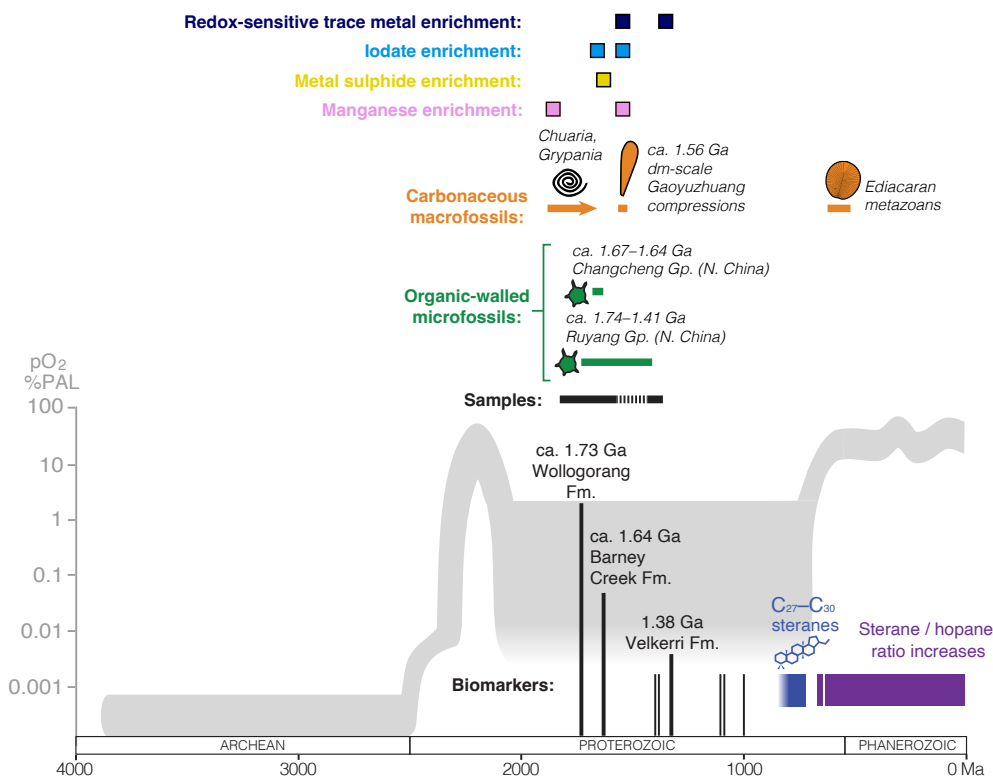


Figure 1.1. The proposed timeline for eukaryogenesis as it relates to the defining events of the middle Proterozoic and the Greater McArthur Basin stratigraphy. Evolution of atmospheric oxygen is shown in relation to dated formations within the McArthur Basin while geochemical evolution of the ocean and associated evolutionary milestones as revealed by the fossil record are outlined in colour. The sampled interval pertaining to Chapter 2 of this study is also outlined in black.

crown group eukaryotes apparently diversified from ca. 1100 – 800 Ma, with major implications for global biogeochemical cycles (Butterfield, 2015; Javaux et al., 2001; Javaux and Knoll, 2017; Porter, 2020). As such, early heterotrophic eukaryotes would have influenced the reprocessing, sedimentation, and preservation potential of organic matter, while the appearance and expansion of photosynthesizing eukaryotes would have altered nutrient flow and export production to sediments (Gibson et al., 2018b). It follows that tracking and understanding the paleoenvironmental significance of early eukaryotic diversification requires a more detailed and systematic characterization of middle Proterozoic environments, including those likely inhabited by early eukaryotes. Linking records of paleoenvironmental and paleobiological change will ultimately elucidate the living needs of early eukaryotes and their subsequent evolutionary trajectory from stem group eukaryotes to crown group eukaryotes containing a set of known characteristics.

Much of our understanding of Earth's paleoenvironments comes from the study of sedimentary successions preserved within basins that formed at that time. The canonical picture includes that

the Paleoproterozoic (2500 — 1600 Ma) experienced the transition to a permanently oxygenated atmosphere during the Great Oxidation Episode (GOE), which occurred between ca. 2400 – 2200 Ma (Figure 1.1; Gumsley et al., 2017; Holland, 2002; Kopp et al., 2005; Lyons et al., 2014; Poulton et al., 2021). Multiple lines of evidence support a rise of free oxygen to roughly 10^{-5} present atmospheric levels (PAL) during this 200 million year interval including U-Pb zircon dates of appropriately aged sedimentary rocks and the disappearance of mass-independently fractionated sulfur isotopes in the sedimentary record (Hodgskiss and Sperling, 2022; Holland, 2002; Poulton et al., 2021; Rasmussen et al., 2013; Warke et al., 2020). This oxygenation episode, although transformative for biology and the geochemistry of the Earth’s surface environment, was initially confined in the oceans to shallow marine environments while the deep oceans and some shelf environments remained anoxic for many hundreds of millions of years. The preponderance of deep ocean anoxia was largely the result of available reductants exceeding the availability of oxygen, while expansion of the marine sulfate reservoir supported increased bacterial sulfate reduction and associated anoxic and sulfidic (euxinic) water masses (Anbar and Knoll, 2002; Canfield, 1998; Lyons et al., 2014; Planavsky et al., 2011). How this oxygenation may have affected marine habitats remains poorly understood, thereby inviting further analysis of marine redox stratification and its direct relationship to the environments microorganisms inhabited.

Most of the early eukaryotic fossil record is derived from sedimentary basins that formed within the northwestern part of the ancient supercontinent Nuna (also referred to as Columbia), which saw the cratons that originated in the Archean Eon assemble through a series of collisional and accretionary events (Ernst et al., 2008; Gibson et al., 2018a; Hoffman, 1997; Meert, 2012; Pehrsson et al., 2016). Although it has been widely argued that Nuna subsequently broke up at the onset of the Mesoproterozoic Era, it is increasingly apparent that many of the continents remained attached, forming large continental amalgamations. Among the unseparated continents was Laurentia, which continued to grow through a long-lived phase of accretionary tectonics and juvenile continental growth on its southern to eastern margins (in present coordinates) that culminated when Baltica and Amazonia collided with this margin during the late Mesoproterozoic Grenville orogeny (Cawood and Pisarevsky, 2017; Evans and Mitchell, 2011; Kirscher et al., 2021). This collision event was one of several major continental collisional events around this time (e.g. the Albany-Fraser belt in Australia-Antarctica and the Namaqua-Natal-Kibaran in southern Africa), which gave rise to the

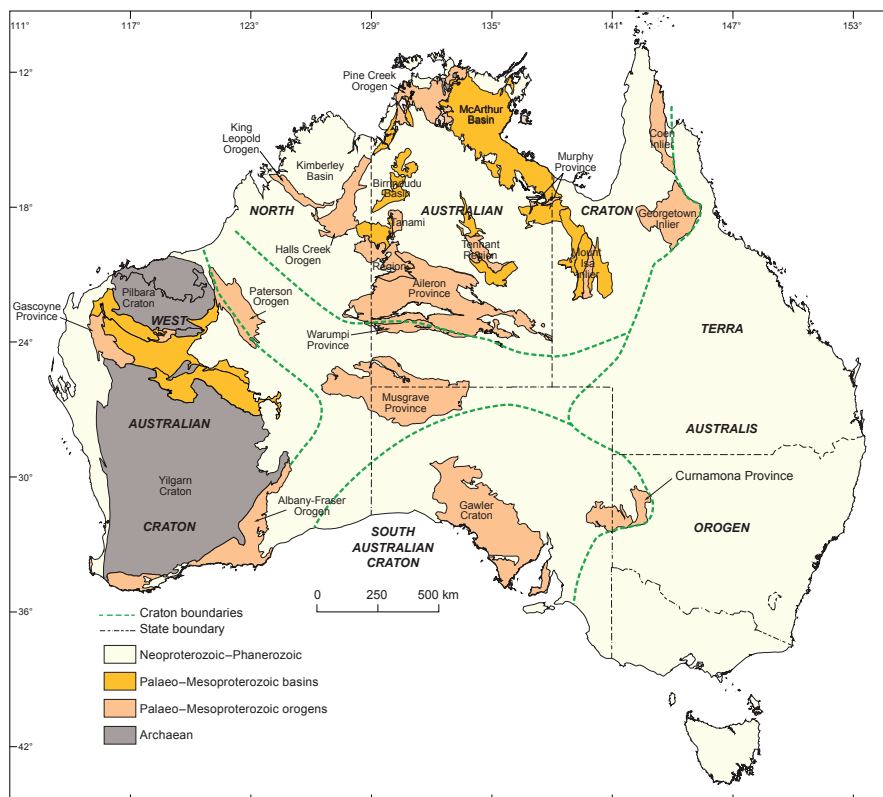


Figure 1.2. Geologic map of modern Australia showing the current distribution of the 5 Archean cratons bounded by the dashed green lines that formed part of the Nuna supercontinent. The location of the correlative McArthur and Birrindudu Basins (and other early Proterozoic Basins) is shown in orange overlying the Northern Australian Craton. Map modified from (Ahmad et al., 2013).

supercontinent Rodinia by ca. 1.05 Ga (Hoffman, 1997; Hou et al., 2008; Gibson and Champion, 2019; Zhang et al., 2012). During this long transition from Nuna to Rodinia, modern-day Australia (including the Pilbara Craton, the Yilgarn Craton, the Northern Australia Craton, and the Southern Australia Craton) likely resided proximal to Laurentia and Siberia (Figure 1.2; Hou et al., 2008). Recent paleogeographic reconstructions have also placed North China in this sector during the middle Proterozoic, with some suggestions it formed the conjugate margin to present-day northwestern Laurentia within Rodinia (Ding et al., 2020).

The focus of this particular study is the late Paleoproterozoic (Statherian) to middle Mesoproterozoic (Ectasian) McArthur and Birrindudu Basins, which directly overlie the metamorphic basement of the Northern Australia Craton (Ahmad et al., 2013; Munson et al., 2020; Kunzmann et al., 2019). The mixed carbonate and siliciclastic strata from these basins are ideal for exploring the habitats of early eukaryotes because they are relatively undeformed and thermally immature, and they are known to preserve abundant microfossils, including likely early eukaryotes (Javaux et al., 2001;

Javaux and Knoll, 2017; Kunzmann et al., 2019), as well as indigenous biomarkers (Brocks et al., 2005; Vinnichenko et al., 2020; Zumberge et al., 2020). Specifically, the aim of this project is to determine the redox conditions of possible eukaryotic habitats in the McArthur and Birrindudu basins in order to help constrain the tempo and setting of eukaryotic origins and early diversification.

The key technique applied in this thesis is iron speciation analysis, which provides a measure of water column redox conditions based on the distribution of iron between detrital and authigenic mineral phases. Iron speciation has been widely applied to the study of middle Proterozoic environments through which it has been established that deep oceans during this time —while containing sufficient sulfide to strongly influence ocean chemistry— were not uniformly euxinic but instead predominantly lightly ferruginous (Gilleaudeau and Kah, 2015; Poulton and Canfield, 2011; Shen et al., 2002; Sperling et al., 2015). Major element composition and total organic carbon (TOC) are regularly analyzed in combination with iron speciation to further refine water column redox conditions (Cumming et al., 2013; Poulton et al., 2010). The ultimate research objective is to apply redox proxies to test whether early eukaryotes inhabited anoxic or oxic environments, or both. The application of iron speciation as a proxy for biotic habitats is unique to this study. Furthermore, the results may have major implications for the tempo of acquisition of key eukaryotic traits in the process of eukaryogenesis, in particular the timing of mitochondrial endosymbiosis (Porter, 2020).

This chapter provides a review of the middle Proterozoic, with an emphasis on marine redox chemistry, the dominant geochemical cycles, and the biological drivers of change within these systems during this time. This review is followed by a description of the stratigraphy and geologic history of the (c.a. 1.8 – 1.3 Ga) Greater McArthur Basin, which is the focus of this study. I report data on 185 samples across 8 cored drill holes and 19 sedimentary formations from this basin. Chapter 2 contains a detailed description of the methods and contributions unique to this thesis, interpretations for the observed trends in the data, and a discussion of how they may relate to the overarching theme of the origin of the eukaryotic cell.

1.2. The Middle Proterozoic (ca. 1.8 – 0.8 Ga) Environment

Geochemical signatures preserved in sedimentary rocks provide valuable insights regarding Earth's environment at the time of their deposition. Multiple proxies are used to infer ancient surface

environments. Together with geological observations, these proxy data reveal that at the beginning of the Proterozoic Eon, life remained restricted to aquatic prokaryotes, the continents were barren, the oceans were only lightly surficially oxygenated, and the atmosphere lacked free oxygen (Butterfield, 2015; Fiorella and Sheldon, 2017; Javaux and Knoll, 2017; Porter, 2020). These conditions changed in a dramatic fashion with the Great Oxidation Event (GOE) and subsequent stabilization of atmospheric oxygen at a fraction of present atmospheric levels.

1.2.1. The Carbon Isotope Record

A widely applied proxy in the study of ancient environments is the ratio of stable carbon isotopes ($^{13}\text{C}/^{12}\text{C}$) preserved in sedimentary carbonates and organic matter. Typically expressed in per mil units (‰) using the standard delta (δ) notation, the ratio is normalized to the Vienna Pee Dee Belemnite (VPDB) reference ratio ($^{13}\text{C}/^{12}\text{C} = 0.0112372$; Coplen, 1988; Craig, 1957) according to the following equation:

$$\delta^{13}\text{C} = \left(\frac{\frac{^{13}\text{C}}{^{12}\text{C}}_{\text{samp}}}{\frac{^{13}\text{C}}{^{12}\text{C}}_{\text{std}}} - 1 \right) * 1000 \quad (1.1)$$

A rock is considered ^{13}C -enriched or positive when $\delta^{13}\text{C}$ values are above the VPDB reference standard, and depleted when values are below the VPDB standard (i.e. negative). During photosynthesis, carbon isotopes become fractionated between oxidized species, such as CO_2 , and reduced organic matter (Buick et al., 1995). Conversely, only minimal fractionation occurs between carbon in the dissolved inorganic carbon (DIC) reservoir and carbonate minerals. As such, carbonates should broadly reflect the composition of the marine DIC pool under stable conditions (roughly 0‰) while organic matter is consistently relatively depleted by 20 to 30‰ (Hayes et al., 1999). Although it is possible for $\delta^{13}\text{C}$ to be overprinted by post-depositional processes because carbon is a major element in carbonates, carbon isotope ratios are naturally more resistant to change when compared to many other isotopic systems including oxygen. Consequently, $\delta^{13}\text{C}$ is one of the most robust geochemical proxies available (Banner and Hanson, 1990; Guo et al., 2013).

Carbon is supplied to the atmosphere via volcanic outgassing of mantle- and metamorphic-derived CO_2 , while silicate weathering, carbonate weathering, oxidative weathering of sedimentary organic carbon, and diffusion between the atmosphere-ocean interface supplies carbon to the oceans. Carbon

dioxide concentrations are estimated to have been around 10 times PAL during the Mesoproterozoic (Fiorella and Sheldon, 2017). Carbon dioxide levels are regulated over long time scales by the temperature-dependent silicate weathering feedback in which hydrolysis reactions with silicate minerals generates clay minerals (i.e., incongruent weathering), as well as bicarbonate (HCO_3^-), and cations (Mg^{2+} and Ca^{2+}), which are delivered to the oceans via runoff and ultimately deposited as limestone and/or dolostone. The temperature dependence of this reaction is a negative feedback which regulates global climate on timescales $> 10^5$ years. For example, an increase in CO_2 will increase temperatures and precipitation rates, which together increase chemical weathering rates. Higher run off in turn will increase photic zone primary productivity (due to increased nutrient supply), therefore increasing the export of sedimentary organic matter (SOM) to the bottom of the ocean where it will either be consumed, remineralized to inorganic carbon through bacterial decay, or buried to form organic-rich sediments. Higher weathering and organic burial rates, will in turn, lead to global cooling, providing a check on rising CO_2 . As such, perturbations to any of the above contributing factors will be preserved in the carbon isotope record of contemporaneous sedimentary rocks.

The carbon isotope record of the Mesoproterozoic shows muted fluctuations compared to the anomalous perturbations associated with the global glaciations that are known to flank the Proterozoic Eon (c.a. 2.5 – 0.542 Ga) (Kah et al., 2004). Combined detailed carbon isotope profiles of marine carbonates spanning the late Paleo- and Mesoproterozoic in Northern Australia (Lindsay and Brasier, 2000, 2002), Western Australia (Wilson et al., 2010; Bekker et al., 2016), Northern China (Guo et al., 2013), and Northern Canada (Hodgskiss et al., 2019b; Hotinski et al., 2004) show isotopic values that deviate no more than 1 - 4‰ around a baseline of 0‰ (Figure 1.3; Buick et al., 1995; Brasier and Lindsay, 1998; Guo et al., 2013; Hodgskiss et al., 2019b; Kah et al., 2001). The peak in values around 1900 Ma has been attributed to a culmination of accretionary orogenesis associated with the assembly of Nuna (Hodgskiss et al., 2019b), while the overall subdued nature of this record has been traditionally invoked as evidence for a protracted interval of ocean-atmosphere stability linked to reduced availability of biolimiting nutrients, lower marine sulfate concentrations, tectonic quiescences, and lower $p\text{CO}_2$ following the GOE (Anbar and Knoll, 2002; Buick et al., 1995; Brasier and Lindsay, 1998; Hodgskiss et al., 2019a; Lindsay and Brasier, 2000). Furthermore, it has been hypothesized that in order to maintain 0.1% PAL of oxygen in the atmosphere, both the

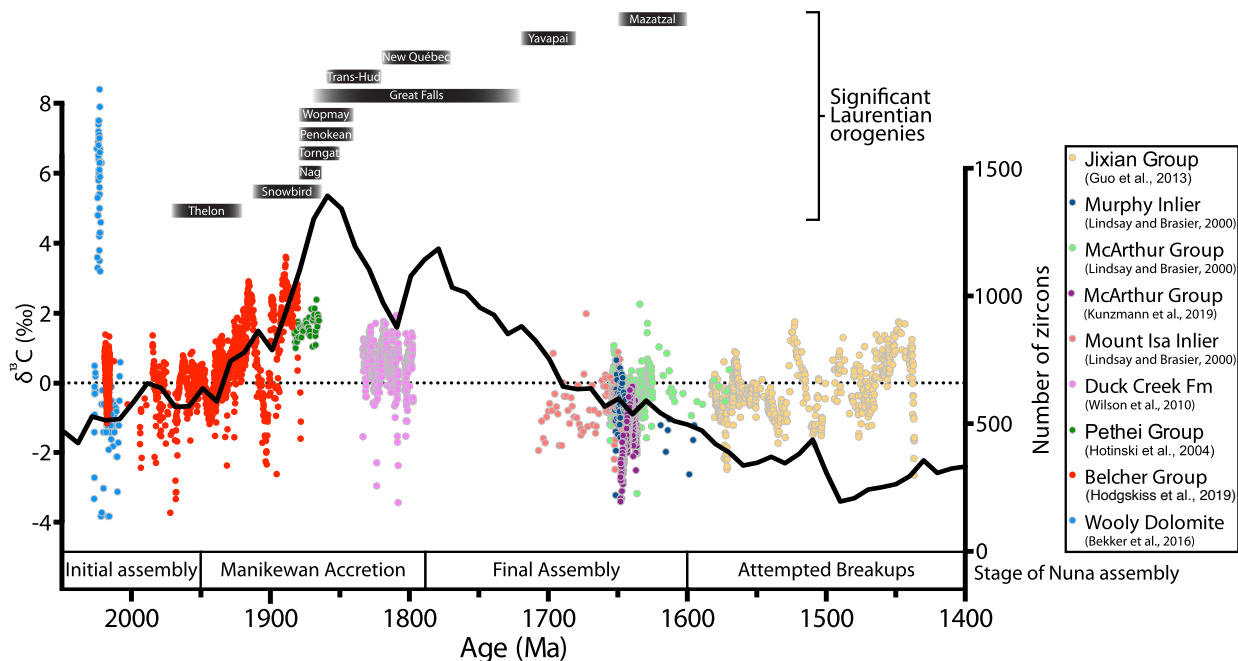


Figure 1.3. Compilation of carbon isotope measurements from Proterozoic basins around the world. Major concomitant orogenic events are indicated by the black bars (Nag = Nagssugtoquidian; Trans-Hud = Trans-Hudson) while the average zircon population in 10 Myr bins is shown by the black line. The proposed rise in $\delta^{13}\text{C}$ values around 1900 Ma is hypothesized to be the result of peak accretionary orogenesis following the deposition of the Rowatt Formation in Northern Canada. There are no additional fluctuations around 0‰ during this 650 Myr timespan. Figure and caption adapted from Hodgskiss et al. (2019b).

overall size of the biosphere and efficiency of microbial gross primary productivity (GPP) would have declined by more than 80% with respect to pre GOE levels (Hodgskiss et al., 2019a).

The $\delta^{13}\text{C}$ record has also been used to infer increasing biodiversity throughout the Mesoproterozoic (Butterfield, 2015; Guo et al., 2013; Kah et al., 2001; Kah and Bartley, 2011). In this scenario, the evolution of the atmosphere-ocean system throughout the middle Proterozoic is regarded not as a period of reduced tectonism or low GPP (Brasier and Lindsay, 1998; Buick et al., 1995; Crockford et al., 2018), but rather a continuation of biospheric evolution against the backdrop of steadily decreasing atmospheric CO_2 levels (Kah and Bartley, 2011). In other words, isotopic stability is interpreted as an indicator of the size of the DIC reservoir and the controls on organic carbon burial (Bartley and Kah, 2004; Guo et al., 2013; Kah and Bartley, 2011). It has been proposed that the absence of $\delta^{13}\text{C}$ variation throughout much of the middle Proterozoic reflects the inability of a high-DIC system to record change (Bartley and Kah, 2004). It can be further argued that the transient variations in $\delta^{13}\text{C}$ about the 0‰ average are the result of a redox stratified ocean wherein microbial communities with different metabolisms (i.e. autotrophs in shallow water and

heterotrophs in deeper water) produced contrasting isotopic signatures locally during fluctuations of relative sea level (Guo et al., 2013). Following these arguments, the increase in the magnitude and variability of $\delta^{13}\text{C}$ can be interpreted in terms of a long-term decrease in $p\text{CO}_2$ associated with a decrease in the size of the DIC reservoir, as well as increased biodiversity and associated organic carbon production (Bartley and Kah, 2004; Guo et al., 2013).

1.2.2. Low Oxygen Atmosphere

The global carbon isotope record has classically been interpreted alongside the oxygenation of Earth's atmosphere (des Marais et al., 1992). The rationale for this coupling is that organic carbon burial naturally influences the carbon cycle and simultaneously provides a source of atmospheric oxygen on geologic timescales (Cartapanis et al., 2016; Kah and Bartley, 2011). As such, the carbon isotope record can be used to quantify addition to or loss of oxygen from the ocean-atmosphere system. However, this system is complicated by the oxygen cycle's concurrent link to both the iron and sulfur cycles. Reduced species of each of these redox sensitive and abundant elements comprise a large fraction of oxygen-consuming sinks. During the middle Proterozoic, the deep ocean was pervasively ferruginous (Fe^{2+} -bearing but non-sulphidic) while deeper waters on the continental margins were predominantly euxinic (i.e. sulfidic; Canfield, 1998; Planavsky et al., 2011; Poulton and Canfield, 2011). These conditions likely served as substantial buffers in the deeper oceans.

Oxygenation of the atmosphere during the GOE saw O_2 released by oxygenic photosynthesis accumulate in the atmosphere and upper oceans to levels between > 0.0001 and 0.1% PAL, though the precise range remains highly debated and dependent upon the proxy used (Figure 1.4; Planavsky et al., 2014; Gilleaudeau et al., 2016; Zhang et al., 2016). Prior to the GOE, massive iron formations were a common feature of the geologic record. After a peak in deposition around the GOE, thick and extensive iron formation deposits disappeared at roughly 1.8 Ga, though they made a brief reappearance ca. 700 Ma associated with the Sturtian Snowball glaciation. Further corroboration for the transition from an anoxic early atmosphere is seen in the ca. 2.4 Ga disappearance of non-mass dependent fractionation of multiple sulfur isotopes (NMD-S) since incorporation and preservation of these signals into ancient sediment requires an atmosphere essentially devoid of oxygen (Farquhar et al., 2000; Lyons et al., 2014). Lastly, redox-sensitive detrital minerals such as pyrite, uraninite, and siderite also disappear from the sedimentary record, while redox sensitive elements released by

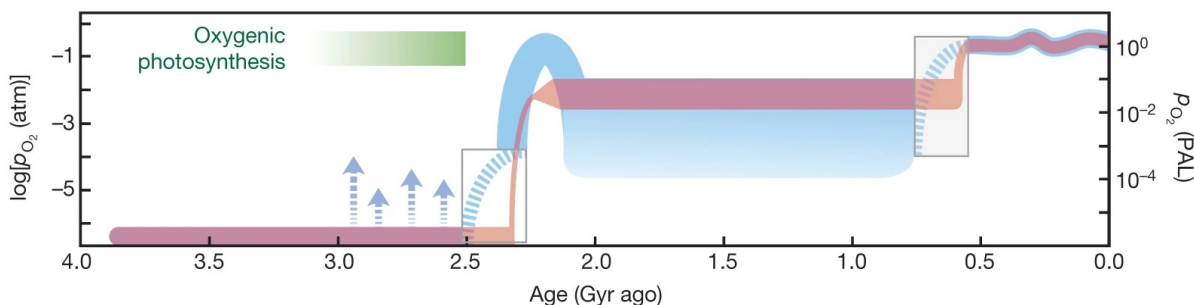


Figure 1.4. Evolution of atmospheric oxygen throughout the Proterozoic from Lyons et al. (2014). The red curve indicates the standard two-step increase in oxygen during the Great Oxidation Event (GOE) and subsequent Neoproterozoic Oxygenation Event (NOE). The blue curve shows the emerging view of an oxygen overshoot and subsequent return to low oxygen values until the NOE.

oxidative weathering (e.g. molybdenum and rhenium) increase in the sedimentary record (Canfield, 2005).

The first permanent accumulation of photosynthetically derived oxygen in the atmosphere was followed by a prolonged interval of very positive $\delta^{13}\text{C}$ values (as high as 10‰) during what is known as the Lomagundi carbon isotope excursion which lasted roughly 2.22 to 2.10 Ga (Bekker et al., 2008; Brasier and Lindsay, 1998; Buick et al., 1995; Hodgskiss et al., 2019b; Karhu and Holland, 1996; Schidlowski et al., 1975, 1976). Such positive isotopic values, if sustained over this entire time frame, imply increased organic carbon burial and the generation of 10 to 20 times the atmospheric oxygen levels proposed for the most of Proterozoic (Hodgskiss et al., 2019a; Planavsky et al., 2014; Wilson et al., 2010). An "oxygen overshoot" during the Siderian and early Rhyacian, followed by a drop to low oxygen levels in the late Rhyacian until the Neoproterozoic, has therefore been proposed (Crockford et al., 2018; Hodgskiss et al., 2019a; Lyons et al., 2014; Planavsky et al., 2014; Wang et al., 2022; Wilson et al., 2010). The exact mechanism for this rise and fall in oxygen and its global significance remains controversial. More recently, it has been proposed that the anomalous values of the Lomagundi event are restricted to facies representative of nearshore environments, while laterally adjacent offshore settings preserve more subdued trends (Prave et al., 2022).

Maintaining the low $p\text{O}_2$ atmosphere throughout the middle Proterozoic requires low primary productivity following the Lomagundi event (Hodgskiss et al., 2019a; Laakso and Schrag, 2019). Empirical evidence for this comes from triple oxygen isotopes ($\Delta^{17}\text{O}$) measured in sedimentary sulfate (SO_4) deposits, which provide a stoichiometric link between $p\text{O}_2$, $p\text{CO}_2$, and primary productivity on the basis that photosynthetic carbon fixation is proportional to oxygen production

(Crockford et al., 2018; Hodgskiss et al., 2019a). Values from the middle Proterozoic (specifically the ca. 1.5 Ga Sibley Group in Ontario and the Belcher Group in Nunanvut) are anomalously low (between 0‰ and -1.0‰) when compared to Phanerozoic (c.a. 541 Ma – present) values of around 0‰ (Crockford et al., 2018; Hodgskiss et al., 2019a). Such negative values could be caused by ultra-high $p\text{CO}_2$, as has been proposed to explain extremely negative oxygen isotope signatures during and immediately following the end-Cryogenian Marinoan glaciation. However, the middle Proterozoic, when compared to the Neoproterozoic glacial periods, had relatively low $p\text{CO}_2$, making limited GPP a more likely explanation (Bao et al., 2008; Crockford et al., 2018; Fiorella and Sheldon, 2017; Hodgskiss et al., 2019a). Furthermore, small negative shifts in the sulfur isotopes and $\delta^{18}\text{O}$ of marine SO_4 imply reduced microbial sulfur cycling and weak sulfide reoxidation (Crockford et al., 2018).

1.3. Proxies for Ancient Marine Chemistry

Understanding the processes that lead to oxic, ferruginous, or euxinic conditions is made possible by multiple geochemical proxies that quantify parts the global iron cycle. These approaches generally involve quantification of highly reactive authigenic iron pools relative to total iron content, which includes detrital phases (Poulton and Canfield, 2011; Planavsky et al., 2011; Raiswell and Canfield, 1998). In modern well-oxygenated oceans, reduced iron (ferrous, Fe^{2+}), released by submarine hydrothermal vents or during diagenesis of iron oxides, readily reacts with free oxygen, generally forming insoluble ferric (oxyhydr)oxide minerals, thereby removing it from the overlying water column (Canfield et al., 2008; Poulton and Canfield, 2011). Where ferruginous and sulfate-poor conditions are able to develop, ferrous iron can accumulate as Fe^{2+} (Poulton and Canfield, 2011; Planavsky et al., 2011). Consequently, highly reactive iron associated with carbonates and oxides will become relatively enriched and only partially sulfidized, therefore preserving a large portion of the authigenic phases relative to pyrite (Canfield, 2005; Canfield et al., 2008; Planavsky et al., 2011). In the case of euxinia, ferrous iron will readily form iron sulphide minerals causing enhanced pyrite enrichment of host sediments (Poulton and Canfield, 2011).

After the earlier hypothesis that the deep oceans become fully oxygenated following the end of BIF deposition ca. 1.8 Ga was overturned, it was widely thought that the deep oceans became

euxinic (Anbar and Knoll, 2002; Canfield, 1998; Lyons et al., 2009b,a; Poulton et al., 2004; Shen et al., 2002). This model, referred to informally as the “Canfield Ocean”, emerged as the paradigm for middle Proterozoic deep ocean chemistry. Geochemical evidence in support of the Canfield Ocean includes low trace metal concentrations and sulfur isotope values of roughly 45‰ recorded in marine sedimentary sulfides. This sulfide-dominated ocean was also deemed consistent with the delay in eukaryotic diversification and expansion because these geochemical conditions would have suppressed the availability of certain key nutrients (Anbar and Knoll, 2002; Canfield, 1998; Planavsky et al., 2014; Shen et al., 2002). However, it has been demonstrated that pervasive euxinia would require enhanced delivery of SO_4 to the deep oceans and increased biological productivity (Canfield, 1998; Crockford et al., 2018, 2019; Hodgskiss et al., 2019a). Furthermore, Mo enrichments measured in Proterozoic marine shales directly contradict widespread euxinia, although they do support higher than modern levels of marine H_2S (Planavsky et al., 2011; Reinhard et al., 2013; Scott et al., 2008). It is now evident that the sulfur isotope dataset upon which the Canfield ocean was proposed is strongly biased by data from continental margins, and does not account for offshore seawater (Planavsky et al., 2011; Reinhard et al., 2013).

The emerging view of the Proterozoic ocean is that it was redox stratified albeit with more widespread ferruginous anoxia and only localized euxinia along continental margins (Figure 1.5; Planavsky et al., 2011; Reinhard et al., 2013; Scott et al., 2008; Bekker et al., 2010; Canfield et al., 2008; Planavsky et al., 2014; Poulton et al., 2010; Poulton and Canfield, 2011). Iron speciation analysis of several middle Proterozoic sedimentary basins containing diverse palaeogeographic and depositional settings yielded dominantly anoxic and non-sulfidic conditions in the overlying water column (Planavsky et al., 2011). Even under a less sulfidic ocean, development of euxinia on continental margins would have resulted in efficient scavenging of some important nutrients, such as Mo. Anoxia was therefore likely maintained by decreased GPP (particularly bacterial sulfate reduction) resulting from limited nutrient fluxes into the ocean (Crockford et al., 2018; Hodgskiss et al., 2019a; Planavsky et al., 2011; Poulton et al., 2010). Low total organic carbon content (less than 1%) and limited sulfur isotope fractionation in the same rocks further corroborate this hypothesis (Planavsky et al., 2011).

Sulfate concentrations in the oceans were likely governed by organic matter fluxes as well as the interplay between oxidative weathering of the continents and the redox controlled burial of sulfur in

marine sediments (see Figure 1.5) (Canfield, 2005; Planavsky et al., 2011; Poulton and Canfield, 2011; Scott et al., 2014). Iron speciation data, coupled with triple sulfur isotope ratios on ca. 2.2 – 2.1 Ga sedimentary pyrite and contemporaneous marine sulfate deposits, indicate a 10-fold increase in the marine sulfate reservoir during the GOE and subsequent Lomagundi excursion (Planavsky et al., 2012; Scott et al., 2014). Following the Lomagundi event —around 2.05 Ga— sulfur

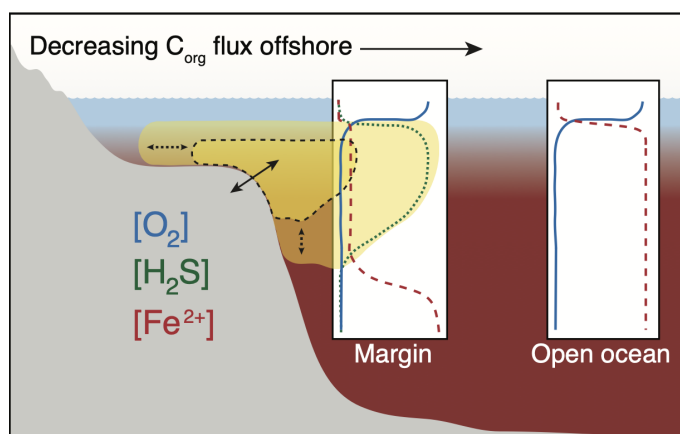


Figure 1.5. Proposed model for Proterozoic ocean chemistry. Adapted from Lyons et al. (2021).

isotopes and iron speciation imply a drastic contraction in the size of the marine sulfate reservoir, consistent with a return to low atmospheric oxygen and persisting for much of the early and middle Proterozoic (Scott et al., 2014). Strongly negative $\delta^{13}\text{C}$ values of coeval organic carbon further support a global collapse in marine sulfate concentrations (Bekker et al., 2016; Scott et al., 2014). The cause of this negative excursion may have been the result of either exhumation and oxidation of buried organic matter or an increase in microbial methane cycling in response to sulfate limitation (Scott et al., 2014; Qu et al., 2012). Modelling suggests marine sulfate concentrations slightly increased into the late Proterozoic, but did not reach or surpass Paleoproterozoic levels until much later in Earth’s history.

1.4. The Appearance of Eukaryotes

Against this backdrop of low $p\text{O}_2$, redox stratified oceans, nutrient limitations, and reduced marine sulfate concentrations, the evolution of complex, multi-cellular life was presumably inhibited until oxygen levels rose again during the NOE (Erwin et al., 2011; Javaux et al., 2004). Eukaryotes are distinguished from prokaryotes in that they possess usually larger, nucleated cells with a complex

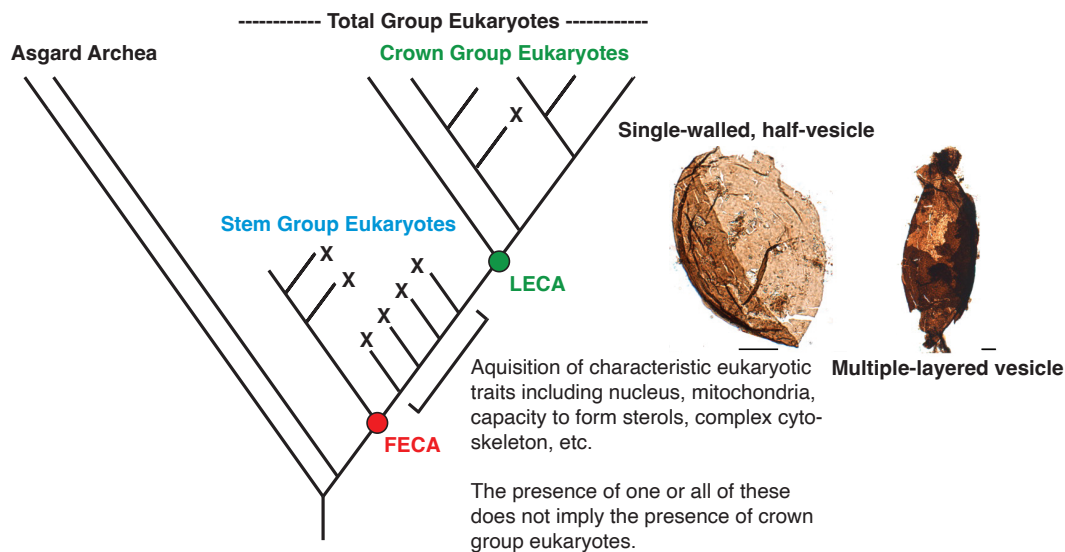


Figure 1.6. Schematic phylogenetic tree showing the evolution of the first eukaryotic common ancestor (FECA) to the last eukaryotic common ancestor (LECA). Branches labelled X represent now extinct clades which include the majority of the early Proterozoic fossil record including acritarchs as well as organic-walled microfossils. Photographs using transmitted light spectroscopy of the oldest known occurrence of these fossils are shown on the right with scale bars = 20 μm (Javaux and Lepot, 2018; Lamb et al., 2009). These cyst-like, rigid specimens are specifically from the 1800 Ma Changzhougou Formation (lowermost Changcheng Group) in the Pangjiapu Region of North China (Javaux and Lepot, 2018; Lamb et al., 2009). Similar structures have been identified in the roughly 1600 Ma McArthur Group in Northern Territory, Australia.

internal structure composed of various membrane-bound organelles including mitochondria, and they have the capacity to form sterols, which are important components of their cell walls (Embley and Martin, 2006; Porter, 2020). The delay in their diversification is reflected in the sedimentary rock record where microfossils inferred to represent crown group eukaryotes do not appear until 1.05 Ga, and biomarker evidence for eukaryotes does not appear until ca. 800 Ma (Anbar and Knoll, 2002; Butterfield, 2000; Brocks et al., 2017; Gibson et al., 2018b; Knoll, 2014; Love and Zumberge, 2021).

The oldest generally accepted microfossil of a distinct crown group eukaryote is the red alga *Bangiomorpha pubescens* from the Bylot Supergroup in northeastern Nunavut that was dated at 1.05 Ga (Butterfield, 2000; Gibson et al., 2018b). Although it is possible that earlier crown group fossils will be discovered, this singular constraint on the eukaryotic fossil record suggests that at least some and maybe most earlier purportedly eukaryotic fossils represent stem group eukaryotes that emerged sometime in the transition between the first eukaryotic common ancestor and the last eukaryotic common ancestor (Knoll, 2014; Porter, 2020). Unfortunately, while there are numerous large, ornamented, and structurally complex microfossils preserved in older Paleoproterozoic rocks,

the classification of these fossils is ambiguous such that they cannot be taxonomically assigned to a group, making them most likely but not unambiguously of eukaryotic origin (Knoll, 2014). These have been ascribed the name acritarchs as an all-inclusive term for large, organic-walled vesicles and fossils (Javaux and Lepot, 2018). The oldest acritarchs of probable eukaryotic origin are found in the $< 1673 \pm 10$ Ma Changzhougou Fm in China and the > 1.65 Ga Mallapunyah Formation of the McArthur Supergroup in Australia (Figure 1.6; Javaux and Lepot, 2018; Javaux, 2007; Lamb et al., 2009; Li et al., 2013). These organisms are embellished with concentric striations and are referred to as the form taxon *Valeria lophostriata* (Javaux and Lepot, 2018).

Much like the scarcity of the body fossil record of early eukaryotes, molecular fossils known as biomarkers produced during sterol synthesis are seemingly absent in middle Proterozoic rocks. These organic compounds degrade during diagenesis to form cyclic steranes and can be used to infer the presence of eukaryotes in paleoenvironments (Brocks et al., 1999; Porter, 2020). It has been established that Archaea (including the Asgard archaea, a recently identified clade that is thought to be the sister group to eukaryotes; Spang et al., 2015) lacked such a capability. Therefore, the capacity for sterol biosynthesis, like the mitochondria, must have evolved sometime during the transition from FECA to LECA via lateral gene transfer, potentially from a bacterium (Embley and Martin, 2006; Hoshino and Gaucher, 2021; Porter, 2020).

Putative sterane biomarkers were reported from the 2.7 Ga drill cores of the Pilbara Craton in Australia and used to infer the presence of distinct eukaryotes in the Neoarchaeon Era (c.a. 2.8 to 2.5 Ga) (Brocks et al., 1999). This work was more recently discredited as abundant anthropogenic contamination was found in the original drill cores (French et al., 2015). It is now accepted that the oldest indigenous eukaryotic steranes are found in various 900 to 720 Ma rocks (Brocks, 2018). The absence of steranes throughout the Mesoproterozoic is generally associated with a lack of diversity or preservational bias; however it is possible that their absence may simply indicate that sterol synthesis, and thus crown group eukaryotes, had not yet evolved (Porter, 2020).

1.5. The Greater McArthur Basin

The Northern Australian Craton (NAC) forms the northern tip of present-day Australia and is bounded by intracratonic orogens including the Terra Australis Orogen in the east and multiple

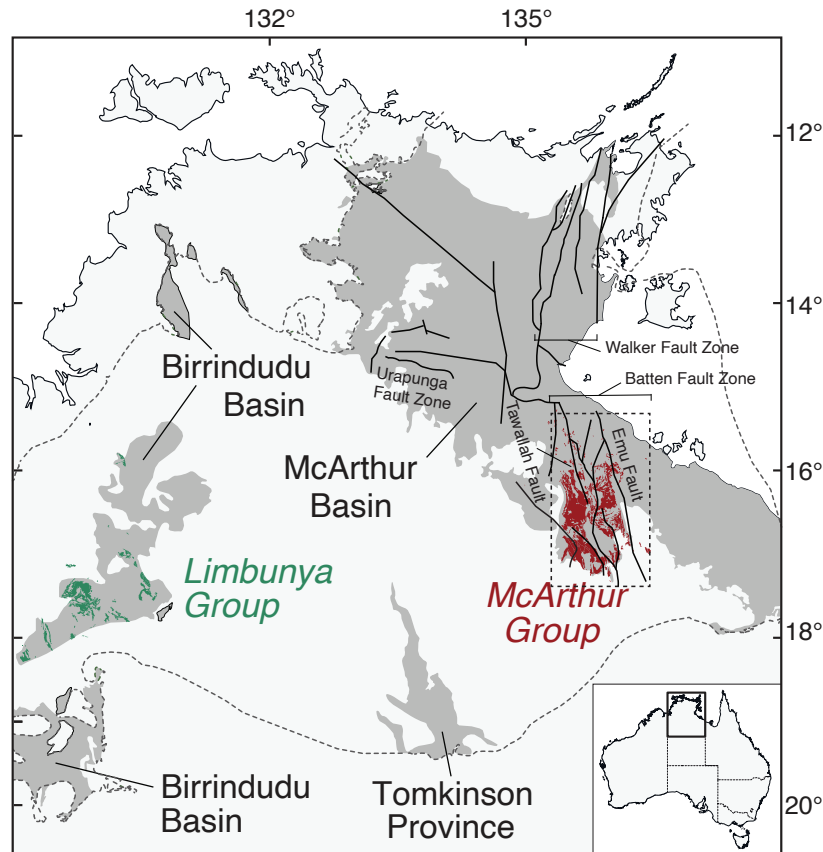


Figure 1.7. Simplified geologic map of the Greater McArthur Basin featuring the chronostratigraphically correlated McArthur and Limbunya Groups as well as major faults outlined in black. Adapted from Kunzmann et al. (2019) and Munson et al. (2020).

Proterozoic orogens in the south-southwest including the Musgrave, Warumpi and Paterson Provinces (Ahmad et al., 2013; Cawood and Korsch, 2008). The Neoproterozoic basement of the NAC is unconformably overlain by c.a. 1.8 Ga bimodal volcanics and a series of variably metamorphosed Paleoproterozoic sedimentary successions that are thought to be linked beneath stratigraphically younger sedimentary basins in the southwest and the Gulf of Carpentaria in the northeast (Kunzmann et al., 2019; Rawlings, 1999). This master superbasin includes the Greater McArthur Basin which remains generally weakly deformed to sub-greenschist facies with the exception of localized areas of increased deformation (Ahmad et al., 2013; Kunzmann et al., 2019).

The (c.a. 1.8 – 1.3 Ga) Greater McArthur Basin is bounded by the Pine Creek Inlier in the northwest, the Arnhem Inlier in the north, and the Murphy Inlier in the southeast (Ahmad et al., 2013; Kunzmann et al., 2019; Plumb et al., 1990; Rawlings, 1999; Scott et al., 2000). Its westernmost

exposure comprises the Birrindudu Basin, while the McArthur Basin proper is exposed in the northeast and is further divided by the east-west striking Urapunga Fault Zone into the northern McArthur Basin and the southern McArthur Basin (Figure 1.7; Ahmad et al., 2013; Kunzmann et al., 2019, 2020; Plumb and Wellman, 1987; Plumb et al., 1990; Rawlings, 1999). Major structural features of the McArthur Basin include the north-south striking Batten and Walker Fault Zones, which were active during deposition and controlled depositional geometries and facies. Despite its proximity to these faults zones, the Birrindudu Basin remains relatively structurally undeformed (Ahmad et al., 2013; Kunzmann et al., 2019; Plumb and Wellman, 1987). These faults were originally thought to be primary depositional features forming a graben-like depocenter (Plumb and Wellman, 1987; Rawlings et al., 2004). Based on more recent seismic data and structural mapping, these trough-like structures have been reinterpreted as small sub-basins that opened along the 80 to 200 km long Batten Fault Zone (Ahmad et al., 2013; Rawlings et al., 2004; Blakie and Kunzman, 2020).

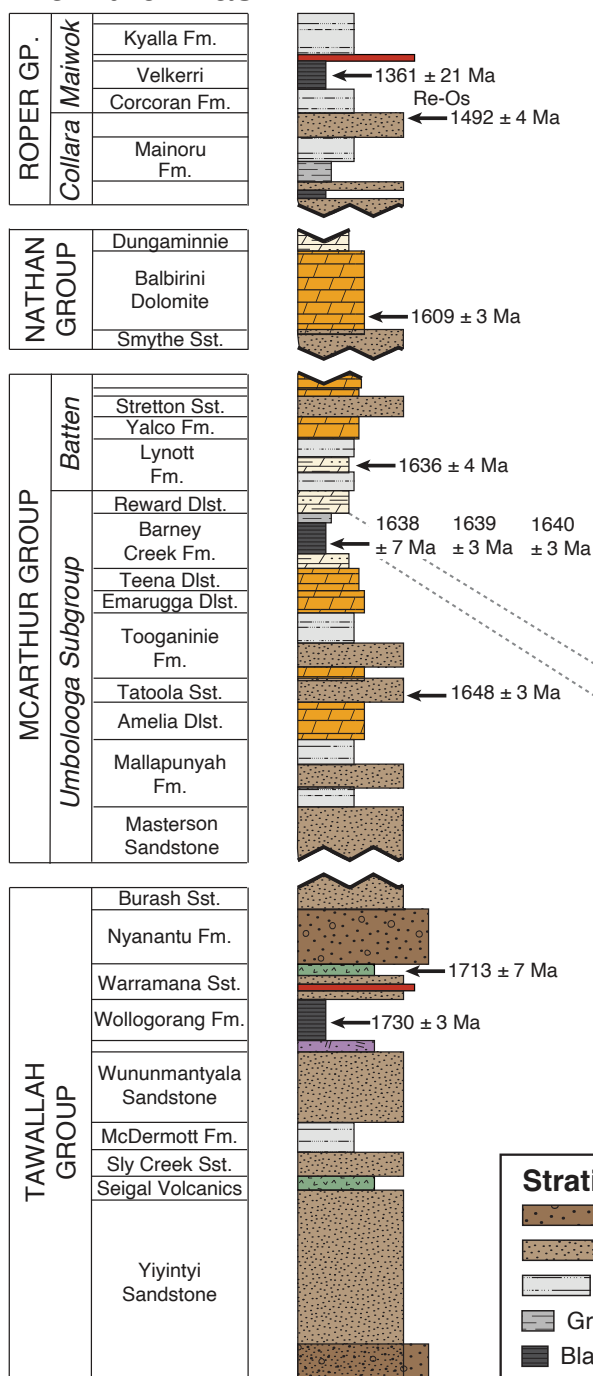
1.5.1. The McArthur Basin

The mixed carbonate and siliciclastic sedimentary succession with minor volcanics of the McArthur Basin has a preserved thickness of 5 to 15 km and can be subdivided into four first-order depositional sequences using a sequence stratigraphic approach (Jackson et al., 1999, 2000) or five unconformity-bound depositional packages (Rawlings, 1999). Both nomenclatures include the Tawallah Group, McArthur Group, Nathan Group, and Roper Group in ascending order (Figure 1.8; Ahmad et al., 2013; Cox et al., 2016; Plumb and Wellman, 1987; Spinks et al., 2016). These four groups are best exposed within the Batten Fault Zone in the southern McArthur Basin (with coeval formations in the north) where they are presumed to have been deposited within large scale, originally continuous, and gently eastward-dipping basins with cyclical sedimentation controlled by tectonism (Ahmad et al., 2013; Kunzmann et al., 2019; Rawlings et al., 2004; Rogers, 1996).

Tawallah Group

The c.a. 1850 – 1715 Ma basal Tawallah Group records the initial north-south extensional rifting stage of the McArthur Basin's intracratonic evolution in three main depositional cycles with intermittent volcanic activity (Ahmad et al., 2013; Rawlings, 1999; Rogers, 1996; Spinks et al., 2016). The lowermost Yiyintyi Sandstone (> 4 km thick) and Sly Creek Sandstone (320 m) record

McArthur Basin



Birrindudu Basin

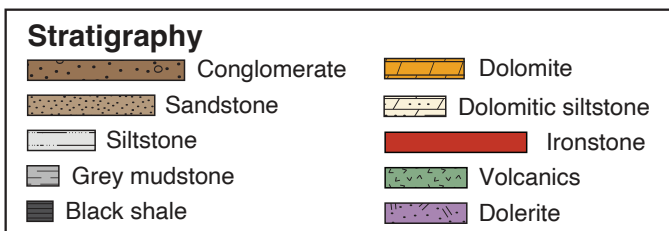
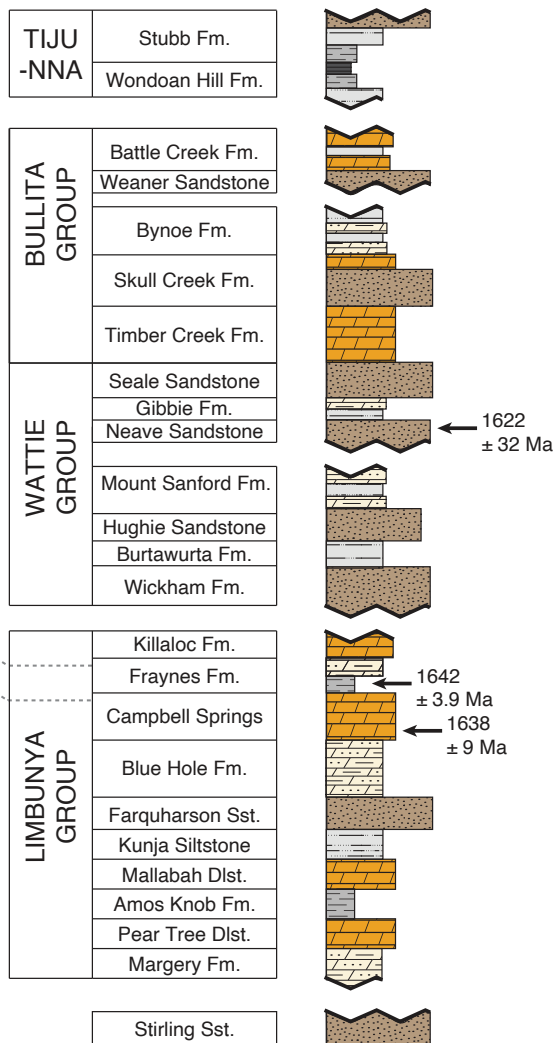


Figure 1.8. Stratigraphy of the correlative McArthur and Birrindudu Basins. Geochronological data (interpreted SHRIMP U-Pb zircon ages from various interbedded volcanics) for the Tawallah, McArthur, Nathan, and Roper Groups from Page et al. (2000) and Jackson et al. (1999). Minimum Re-Os age for the Velkerri Formation of the Roper Group from Kendall et al. (2009). SHRIMP U-Pb age of a single zircon in the Campbell Spring Dolostone from Cutovinos et al. (2002). Interpreted CA-IDTIMS U-Pb zircon age from the chronostratigraphically correlated the Fraynes Formation from Munson et al. (2020). SHRIMP U-Pb detrital zircon age of the Neave Formation from Carson (2010).

a transgressive transition from an alluvial braid plain to a shallow marine depositional environment (Ahmad et al., 2013; Rogers, 1996). These strata are separated by the mafic and broadly subaerial Seigal Volcanics with spatially variable thicknesses between 250 and 1100 m (Ahmad et al., 2013; Rawlings, 1999; Rogers, 1996). The overlying McDermott Formation (200 m), the Wununmantlyala Sandstone (> 800 m), and the Wollogorang Formation (> 350 m) together represent a second extensional sedimentary sequence and transgressive phase locally controlled by intrabasinal tectonic uplift along the Tawallah Fault (Ahmad et al., 2013; Rogers, 1996). This sedimentary succession consists of lowermost organic-rich mudstones and carbonate bearing siltstones of the McDermott Formation, overlain by the Wununmantlyala Sandstone followed by a sequence of organic-rich, stromatolitic dolomitic mudstones/siltstones with minor evaporites and sandstones characteristic of the lower fluvial and upper channelized intertidal facies of the Wollogorang Formation (Spinks et al., 2016). The Wollogorang Formation includes the mafic flows of the Settlement Creek and Gold Creek Volcanics at the base and top, respectively. These have yielded SHRIMP U-Pb zircon depositional ages between between 1730 ± 3 and 1729 ± 4 Ma (Page et al., 2000; Rogers, 1996; Spinks et al., 2016). The uppermost sequence in the Tawallah Group comprises the Warramana Sandstone, the Nyanantu Formation, and the Burash Sandstone, in ascending order (Ahmad et al., 2013; Rogers, 1996). This regressive depositional phase includes conglomeratic braided river deposits capped by quartz arenite deposited in response to deformation and uplift of older formations due to a period of east-west compression (Bull and Rogers, 1996; Rawlings, 1999; Rogers, 1996). This final succession is overlain locally by the Tanumbirini Rhyolite, which has been dated by U-Pb SHRIMP at c.a. 1713 ± 7 Ma (Ahmad et al., 2013; Page et al., 2000; Rogers, 1996).

McArthur Group

The McArthur Group unconformably overlies the Tawallah Group, indicating a maximum age of ca. 1710 Ma. It only occurs exclusively in the Batten Fault Zone (Ahmad et al., 2013; Jackson et al., 1987; Rawlings, 1999; Rawlings et al., 2004). Unlike the Tawallah Group, sediment accumulation of the McArthur Group was controlled by a period of thermal subsidence and is dominantly dolomitic and evaporitic in nature (Rawlings, 1999). It has been weakly to strongly deformed in most places and experienced a period of northeast-southwest compression midway through deposition that reactivated similarly oriented normal faults (Rawlings, 1999; Rogers, 1996). A proposed unconformity separates

the McArthur group into the lower Umbolooga Subgroup and the upper Batten Sugroup (Jackson et al., 1987; Rawlings, 1999).

The Umbolooga Subgroup includes the basal, ridge-forming Masterson Sandstone, which varies in thickness between 40 and 650 m and is composed primarily of variably coloured fluvial to shallow marine sandstones with minor mud and siltstones (Ahmad et al., 2013). It is conformably overlain by the recessive Mallapunyah Formation (100 to 450 m), which is dominated by desiccation features within interbedded mudstone, siltstone, stromatolitic dolostone, and dolomitic sandstones interpreted to be the product of shallow marine to coastal sabkha depositional environments (Ahmad et al., 2013; Jackson et al., 1987). The overlying 50 to 180 m-thick, marginal marine Amelia Dolostone is composed of stromatolitic dolostone and minor silty dololite with diagenetic siderite (Ahmad et al., 2013). The Tootla Sandstone overlies the Amelia Dolostone and is divided into a lower, storm affected deep water facies composed mostly of thinly bedded sandstone and dolomitic sandstone, which grades upwards into shallower marine to peritidal facies represented by medium-grained sandstone with evaporitic casts and molds (Ahmad et al., 2013; Jackson et al., 1987). The conformably overlying Tooganinie Formation is 200 m thick and includes peritidal to emergent shoreline deposits of dololite, stromatolitic and/or oolitic dolomite, dolarenite, dolomitic siltstone, and shale with abundant features indicating exposure and evaporation, including mudcracks, halite casts, teepee structures (Ahmad et al., 2013; Jackson et al., 1987; Kunzmann et al., 2019). It is conformably overlain by the 10 to 30 m thick Leila Sandstone that likely marks the transition between the shallow/emergent environment of the Tooganinie Formation and the 650 m thick, shallowing upwards succession of the Emerugga Dolostone (Ahmad et al., 2013; Kunzmann et al., 2019). The Emerugga Dolostone is subdivided within the Batten Fault Zone into the stromatolitic Mara Dolostone with interbedded dolarenite and dololite, which is overlain by the heavily altered Mitchell Yard Member (Ahmad et al., 2013; Kunzmann et al., 2019). Conformably overlying the Emerugga Dolostone is the Teena Dolostone which is composed of a lower, 60 m-thick member of thinly bedded stromatolitic dolostone, dololite, and dolarenite as well as the upper, 70 m-thick Coxco Member distinguished by the presence of radiating needles of gypsum pseudomorphs (Ahmad et al., 2013; Kunzmann et al., 2019; Walker et al., 1977).

The Barney Creek Formation conformably overlies the Teena Dolostone and marks a change in the tectonic controls on sediment deposition in the southern McArthur Basin from relative tectonic

quiescence to the opening of multiple sub-basins and a period of compression along northeast-southwest striking faults (Kunzmann et al., 2019; McGoldrick et al., 2010; Rogers, 1996). As a result, deposition of the organic-rich Barney Creek Formation in subtidal to deep marine settings was largely fault-controlled, accounting for its lateral variability in thickness from 10 to 900 m (Ahmad et al., 2013; Jackson et al., 1987; Kunzmann et al., 2019; McGoldrick et al., 2010). The Barney Creek Formation is subdivided into the W-Fold Shale, the HYC Pyritic Shale, and the Cooley Dolostone members, in ascending order (Jackson et al., 1987; Kunzmann et al., 2019). The W-Fold Shale comprises variably coloured dolomitic siltstones and dololutite, which grade upwards into the dolomitic and pyritic siltstones of the HYC Pyritic Shale, host of the world class Zn-Pb-Ag McArthur River deposit. It also contains three tuff beds with U-Pb SHRIMP ages of 1638 ± 7 Ma, 1639 ± 3 Ma, and 1640 ± 3 Ma (Kunzmann et al., 2019; Page et al., 2000). The Cooley Dolostone is a facies equivalent of the other two members and consists of mass flow deposits of fault-brecciated carbonate with clasts from the underlying dolostone units that interfinger with the shales (Ahmad et al., 2013; Kunzmann et al., 2019). The conformably overlying Reward Dolostone is 350 m thick and consists of dololutite, dolarenite, stromatolitic dolostone, and dolomitic sandstone inferred to have been deposited in a shallow marine setting (Ahmad et al., 2013; Kunzmann et al., 2019).

A prominent unconformity between the Umbolooga Subgroup and the Batten Subgroup is manifested by areas of paleoregolith observed overlying the Reward Dolostone and underlying the Lynott Formation (Ahmad et al., 2013). The 50 to 600 m-thick Lynott Formation comprises three conformable members collectively recording a shoaling upward sequences, from thinly bedded, fine-grained and variably dolomitic mudstone (locally pyritic and/or brecciated), into stromatolitic dolostone, dololutite, and dolomitic sandstone with evaporite pseudomorphs, and finally into dolomitic silt and sandstone with abundant cauliflower and enterolithic chert (Ahmad et al., 2013; Jackson et al., 1987). Associated depositional environments began as deep marine, shoaling upwards into intertidal then peritidal to supratidal sabkha (Ahmad et al., 2013). The Yalco Formation overlies the Lynott Formation and varies laterally in thickness from < 50 to 250 m thick. It comprises ridge forming, commonly interbedded layers of stromatolitic dololutite, silty dololutite, and dolarenite with abundant chert nodules, collectively implying a shallow marine to emergent depositional environment (Ahmad et al., 2013). The overlying Stretton Sandstone has a maximum thickness of 270 m (Ahmad et al., 2013). This fine- to medium-grained sandstone is distinctly wavy bedded with ripple marks and

hummocky cross stratification implying deposition in a sub-wave base environment (Ahmad et al., 2013). Two thin formations known as the Looking Glass Formation (30 to 70 m) and the overlying Amos Formation (< 70 m) form the uppermost Batten Subgroup. The Looking Glass Formation is a distinctly silicified sequence of stromatolitic dolostone, sandy dololite, and dolarenite (Ahmad et al., 2013). An erosional surface is inferred between the Looking Glass Formation and the overlying Amos Formation, which comprises distinctly terrestrial red beds in its lower portion. These are then overlain by shallow marine, karstified, and recrystallized dolostone (Ahmad et al., 2013).

Nathan Group

Another regional unconformity separates McArthur Group from the overlying Nathan Group, which in turn is unconformably overlain by the Roper Group (Jackson et al., 1987; Plumb and Brown, 1973). Within the Batten Fault Zone, the Nathan Group is divided into three members: the Smythe Sandstone, the Balbirini Dolostone, and the Dungaminnie Formation, in ascending order (Ahmad et al., 2013). The Smythe Sandstone is < 100 to 250 m thick, comprising fluvial conglomerates overlain by massive, terrestrial, coarse-grained sandstone (Ahmad et al., 2013), transitioning upwards into shallow marine dololite, dolomitic siltstone and shale facies of the Balbirini Dolostone (Ahmad et al., 2013). This unit is conformably overlain by the < 240 m-thick Dungaminnie Formation characterized by fine sand and siltstone at the base and stromatolitic dolostone with prominent ooids at the top (Ahmad et al., 2013).

Roper Group

The Mesoproterozoic Roper Group is exposed throughout the northern and southern McArthur Basin and can be divided into six progradational (coarsening upwards) units that fluctuate laterally in thickness as a whole (Rogers, 1996; Abbott and Sweet, 2000; Ahmad et al., 2013; Cox et al., 2016; Jackson et al., 1987; Rogers, 1996). Generally, the Roper Group is thinnest within both the Urapunga and Batten Fault Zones (roughly 1500 m) and is laterally continuous towards the southwest where it thickens into the Beetaloo sub-basin, reaching a maximum thickness of > 5 km (Ahmad et al., 2013; Abbott and Sweet, 2000; Jackson et al., 1987; Rawlings et al., 2004). Correlations have been made between the Roper Group and other Mesoproterozoic marine successions of northern Australia including the South Nicholson Group in the South Nicholson Basin and the Renner Group in the

Tomkinson Province making it significantly younger than the unconformably underlying Nathan Group (Figure 1.7; Ahmad et al., 2013). These correlations, in conjunction with substantial lateral continuity, support deposition during a sag phase (i.e. thermal subsidence) of basin development likely within in a marine continental shelf environment or an intracratonic ramp system (Abbott and Sweet, 2000; Cox et al., 2016; Jackson et al., 1987).

The Collara Subgroup is the oldest of two subgroups making up the Roper Group. The lowermost exposure comprises either the roughly 40 - 80 m thick Phelps Sandstone in the northwest or the stratigraphically younger Mantungula Formation (< 150 m) and Limmen Sandstone (20 to 100 m) (Ahmad et al., 2013). The Phelps Sandstone is primarily a quartz sandstone and siltstone with minor conglomerate and breccia interpreted to be fluvial in origin. The conformably overlying Mantungula Formation represents a short recessive interval of storm-dominated marine muds and silts (Ahmad et al., 2013). The Limmen Sandstone forms an erosive contact with the underlying Mantungula Formation and represents a return to fluvial, quartz-rich sandstones with increased lithic fragments and minor pebble intervals towards its base (Ahmad et al., 2013). It is overlain by the Mainoru Formation (maximum thickness of 921.5 m) which can be subdivided into six lithological members: the Gibb, Wadjeli Sandstone, Nullawun, Mountain Valley Limestone, Wooden Duck, and Showell (from oldest to youngest) (Abbott and Sweet, 2000; Ahmad et al., 2013). The lower Mainoru Formation comprises storm-dominated marine mudstones that coarsen upwards into storm-dominated shelf sandstones with minor oolitic ironstones (Abbott and Sweet, 2000). These are conformably overlain by pedogenic mudstones of the Nullawun Member interpreted to be fluvial floodplain deposits (Abbott and Sweet, 2000; Sweet et al., 1988). The Mountain Valley Limestone Member marks a transition back to shallow marine mudstones, now interbedded with intraclast limestone (Abbott and Sweet, 2000; Jackson et al., 1999). The conformable Wooden Duck Member is dominated by green shelf mudstones and fine glauconitic sands and includes tuffaceous bands that yielded a single U-Pb SHRIMP zircon age of 1492 ± 4 Ma (Jackson et al., 1999). The uppermost Showell Member represents a more distal facies of laminated, variably calcareous muds and glauconitic sands. The Mainoru Formation grades upwards into the 0 to 235 m thick Crawford Formation which comprises trough cross bedded glauconitic sandstones and likely marks the onset of deposition of tidally dominated sandstones known to cap the third-order progradational sequences within the Roper Group (Ahmad et al., 2013; Abbott and Sweet, 2000; Sweet et al., 1988). Where

present, the white, quartz-rich, Arnold Sandstone forms an erosive contact with the upper Crawford Formation, which is locally disconformably overlain by the interbedded sands and silts of the Jalboi Formation (Ahmad et al., 2013). The Hodgson Sandstone is a pink to white resistant bed of quartz-rich sands that variably gradationally or erosively overlies the Jalboi Formation and concludes the Collara Subgroup.

The Maiwok Subgroup represents a transition back to fine-grained deposits and the increased presence of ironstone (Ahmad et al., 2013; Abbott and Sweet, 2000; Dunn, 1963; Walpole, 1968). The lowermost red fluvial muds and psolitic ironstones of the 180 to 225 m thick Corcoran Formation are disconformable with the underlying Hodgson Sandstone (Ahmad et al., 2013). These grade upwards into laminated green and grey marine muds which are disconformably overlain by the tidal sands of the Bessie Creek Sandstone (20 to 56 m thick) (Ahmad et al., 2013). The distal Velkerri Formation and overlying tidally influenced Moroak Sandstone comprise another third-order progradational sequence of the Roper Group (Abbott and Sweet, 2000). The 330 to 880 m thick Velkerri Formation is dominantly composed of massive to laminated, organic-rich, pyritic grey mudstones and glauconitic siltstones with three characteristic horizons of > 5% TOC (of highly variable thermal maturity) known to host abundant oil likely stemming from a prokaryotic source (Abbott and Sweet, 2000; Crick et al., 1988; Kendall et al., 2009; Jackson et al., 1986; Jackson and Raiswell, 1991; Sweet et al., 1988). The 3 to 420 m thick Moroak Sandstone disconformably overlies this and grades upwards within the formation from bedded fine-grained sands to coarse sands with granule intervals which eventually give way to the fluvial Sherwin Formation (maximum thickness 100 m) composed of interbedded sands, silts, and muds with distinctive local ironstone lenses (Ahmad et al., 2013). Conformably above this is the Kyalla Formation dominated by interbedded sands, silts, and muds which extend stratigraphically for 250 m and are interpreted as storm-dominated shelf deposits (Abbott and Sweet, 2000; Ahmad et al., 2013). These are sharply overlain by the youngest formation of the Roper Group, the Bukalorkmi Sandstone, composed of 10 to 20 m of coastal, trough cross-bedded quartz sandstone (Abbott and Sweet, 2000; Ahmad et al., 2013).

1.5.2. The Birrindudu Basin

The Birrindudu Basin comprises the westernmost exposure of the Greater McArthur Basin and unconformably overlies the metamorphic basement rocks of the Pine Creek Orogen in the

North, the Tanami Region in the south, and the Halls Creek Orogen in the west (Ahmad et al., 2013; Kunzmann et al., 2019). While comparatively understudied, it has been broadly correlated with the McArthur Basin using lithological similarities, confirmed by recent chronostratigraphic correlation between the 1642 ± 3.9 Ma Fraynes Formation (Munson et al., 2020) and the c.a. 1640 Ma Barney Creek Formation of the McArthur Basin (Page et al., 2000). These findings further support the interpretation that the basins are likely linked beneath younger sedimentary cover and were conterminous at the time of deposition (Ahmad et al., 2013; Kunzmann et al., 2019; Munson, 2016). The Birrindudu Basin can also be further subdivided into 6 unconformity-bound groups: the Birrindudu Group, the Limbunya Group, the Wattie Group, the Bullita Group, the Tjunna Group, and the Victoria Basin Ahmad et al. (2013). This study in particular focuses on the Limbunya through the Tjunna Groups (Figure 1.8).

Limbunya Group

The Limbunya Group unconformably overlies either the Birrindudu Group or the metamorphic basement of the Northern Australian Craton (Ahmad et al., 2013; Cutovinos et al., 2002; Dunster et al., 2000). It comprises a cyclical succession of siliciclastic and carbonate rock that begins with the 120 m-thick Stirling Sandstone, which is composed of massive to bedded quartz sandstone with abundant interference ripples and dewatering structures suggesting a tidal origin (Ahmad et al., 2013; Cutovinos et al., 2002). The Margery Formation is a 125 m-thick succession beginning with oxidized terrestrial clays overlain by variably dolomitic sands and muds with abundant biohermal stromatolites and dewatering/emergent structures indicative of intertidal with localized emergent depositional conditions (Ahmad et al., 2013). A large unconformity separates the Margery Formation from the overlying Pear Tree Dolostone (80 m thick) which includes a coarsening upwards dolomitic sequence with distinct stromatolites near the top (Ahmad et al., 2013; Sweet et al., 1974). The 50 m-thick Amos Knobb Formation is conformable with the Pear Tree Dolostone and is dominantly red or green mudstones with interbedded dolomitic bioherms (Ahmad et al., 2013; Cutovinos et al., 2002). The overlying Mallabah Dolostone is up to 100 m thick and made up of ferruginous, laminated dolostone with local silicified conical and biostromal stromatolites that cumulatively grades into dolomitic mudstone (Ahmad et al., 2013; Cutovinos et al., 2002). The presence of stromatolites and local breccias would suggest a storm-influenced, shallow marine depositional environment,

but, carbonaceous black shales found only in drill core stipulate deeper marine (Ahmad et al., 2013; Cutovinos et al., 2002). The overlying Kunja Siltstone (60 m thick) comprises laminated mudstones and fissile shales interpreted to record a maximum flooding surface (Cutovinos et al., 2002). Drillcores have revealed water-lain tuff beds in the Kunja Sandstone with, one of which has yielded a SHRIMP U-Pb zircon ages of 1635 ± 19 Ma that has yet to be successfully correlated with the corresponding McArthur Basin (Fanning, 1991).

Conformably above the Kunja Sandstone is the 115 m-thick, massive and blocky Farquharson Sandstone. This formation includes mudstone interbeds, abundant ripples, desiccation features, and variably stromatolitic dolostone near the top indicative of a fluvial to shallow-marine or evaporitic depositional environment (Cutovinos et al., 2002). This is succeeded by the > 300 m-thick Blue Hole Formation composed primarily of dolomitic mudstone, dolomitic siltstone, stromatolitic dolostone, and dolomitic sandstone (Ahmad et al., 2013; Dunster et al., 2000). Within this formation are bottom-nucleated acicular crystal pseudomorphs similar to those found in the Teena Dolostone of the McArthur Group, suggesting a potential lithostratigraphic correlation (Ahmad et al., 2013; Walker et al., 1977). Possible depositional environments include quiet, shallow marine as evidenced by the alignment of stromatolites, with some intervals of deeper water deposition. The overlying Campbell Springs Dolostone is commonly 170 m thick, but exceeds 300 m in some localities (Ahmad et al., 2013). It is composed mainly of stromatolitic (both biohermal and biostromal) dolostone, dolomitic sandstone, oolitic dolostone, plate breccia, dolorudite, and dolomitic siltstone (Ahmad et al., 2013; Sweet et al., 1974). Coxco Needles have also been identified in the middle to upper portions while zircons found in minor water-lain tuff beds yield a U-Pb SHRIMP age of 1638 ± 9 Ma (Cutovinos et al., 2002) providing grounds for correlation with the Teena Dolostone (Ahmad et al., 2013).

The Fraynes Formation is conformable with the underlying Campbell Springs Dolostone and is generally less than 100 m thick (Ahmad et al., 2013; Munson et al., 2020). It is composed of laminated dolomitic silt- and mudstone, minor silty dolostone, dolostone, siliciclastic siltstone, very fine sandstone, and minor tuffaceous sediments/tuffites deposited in a nearshore shallow marine environment (Ahmad et al., 2013; Cutovinos et al., 2002; Munson et al., 2020). Carbonate content noticeably increases upsection, and pressure solution as well as preferential compaction features are common throughout (Ahmad et al., 2013; Cutovinos et al., 2002; Sweet et al., 1974). The $1642 \pm$

3.9 Ma age was measured using U-Pb CA-IDTIMS on zircons from tuffaceous silts near the base of the formation (Munson et al., 2020; Page et al., 2000). The Killaloc Formation is the youngest member of the Limbunya Group and conformably overlies the Fraynes Formation (Ahmad et al., 2013; Munson et al., 2020). It comprises a 60 m-thick, fining upwards succession of variably dolomitic and variably stromatolic sands and silts, into dololutite and dolomitic siltstone (Ahmad et al., 2013). The abundance of shallow water to emergent features including ripples, mudcracks, rip-up breccias, halite casts, gypsum pseudomorphs, and 30 cm wide cauliflower chert nodules suggests a hypersaline lagoon or evaporative shallow marine depositional environment (Ahmad et al., 2013).

Wattie Group

In contrast with the Limbunya Group, the Wattie Group is interpreted to be generally recessive and largely siliciclastic. The two are mostly separated by a large angular unconformity; however, a gradational contact has been observed in drillcore (Ahmad et al., 2013). The lowermost Wickham Formation is roughly 175 m thick and consists mainly of fine- to medium-grained sandstone with pebbly intervals, as well as conglomerates and cherts (Ahmad et al., 2013; Beier et al., 2002b). There is commonly a basal conglomerate, as well as evaporite pseudomorphs, ripples, and mudcracks suggesting evaporitic or subaerial conditions during deposition (Ahmad et al., 2013; Beier et al., 2002b). A maximum depositional age is provided by a U-Pb SHRIMP detrital zircon weighted mean age of 1639 ± 16 Ma (Carson, 2010). The conformably overlying Burtawurta Formation is considered to be less than 60 m thick and composed primarily of siltstone with minor interbeds of sandstone, mudstone, and dolostone. A quiet, shallow marine depositional environment with intermittent exposure is inferred from ripple marks, mudcracks, and halite casts (Ahmad et al., 2013). Where the Burtawurta Formation is present, it is conformable with the overlying the Hughie Sandstone. In its absence, the roughly 90 m thick Hughie Sandstone, composed of near to shallow marine, rippled and cross bedded fine- to medium-grained sandstone, conformably overlies the Wickham Formation (Ahmad et al., 2013). The Mount Sanford Formation is conformable above the Hughie Sandstone and varies locally and regionally in both composition and thickness with thicknesses reaching 200 m in the north (Ahmad et al., 2013; Sweet et al., 1974). It comprises interbedded siltstone, dolostone, fine sandstone, dolomitic mudstone, chert, and infrequent claystone and tuff interpreted to be shallow marine in nature (Ahmad et al., 2013).

A local unconformity separates the 1622 ± 32 Ma (U-Pb SHRIMP detrital zircon age; Carson, 2010) Neave Sandstone and the Mount Sanford Formation (Ahmad et al., 2013). The Neave Sandstone comprises a 20 m-thick succession beginning with a basal conglomerate containing chert and quartzite clasts into gray/purple medium-grained sandstones composed mainly of quartz with abundant feldspar, chert, clay, and lithic fragments deposited in a shallow marine environment (Ahmad et al., 2013). It is conformably overlain by the 25 to 70 m-thick Gibbie Formation characterized by thinly bedded, heterogenous siltstones, sandstones, and dolostones deposited in a low energy, potentially lagoonal environment (Ahmad et al., 2013). Above, the conformable Seale Sandstone marks the onset of high energy, transgressive depositional conditions (Ahmad et al., 2013). The formation varies from 5 to 111 m thick and consists of medium-grained quartz sandstone rich in live oil (Ahmad et al., 2013; Dunster and Cutovinos, 2002).

Bullita Group

Unconformably above the Wattie Group is the Bullita Group which records a transition back to carbonate deposition with the onset of the > 300 m thick Timber Creek Formation (Ahmad et al., 2013; Beier et al., 2002b). Thin interbeds of siltstone, mudstone, and dolostone containing abundant desiccation features, disseminated pyrite, reduction spots, epigenetic galena, and various stromatolites indicative of deposition in a shallow marine, intermittently evaporitic setting (Ahmad et al., 2013; Beier et al., 2002a). The Skull Creek Formation (160 to 230 m thick) generally overlies the Timber Creek Formation but is at times interpreted as its lateral facies equivalent (Ahmad et al., 2013). Carbonate content generally increases upsection from medium-grained sandstones into dolarenite, into stromatolitic dolostone, dolomitic siltstone, oolitic grainstone, and chert (Ahmad et al., 2013; Beier et al., 2002a). Sedimentary structures akin to those of the Timber Creek Formation imply deposition within an analogous shallow marine context with flake breccias indicating increased storm action (Ahmad et al., 2013; Beier et al., 2002a,b). This formation is capped by the distinct Supplejack Dolostone comprising 60 meters of dark grey recrystallized biostromal/biohermal dolostone likely deposited during a brief marine transgression (Ahmad et al., 2013; Beier et al., 2002b,c).

The 243 m thick Bynoe Formation is characterized by dolomitic siltstone with increased prevalence of massive siltstone and sandstone towards the middle of the formation (Ahmad et al., 2013; Beier et al., 2002a). A subsequent return to silt- and mudstones towards the top of the formation along

with the presence of halite casts, ripples, and vugs of gypsum indicative of occasional subaerial exposure, has been interpreted to indicating fluctuating shallow and deeper marine environments (Ahmad et al., 2013; Beier et al., 2002a). The Weaner Sandstone lies unconformably above this in drillcore but is locally conformable in outcrop (Ahmad et al., 2013; Beier et al., 2002a). It is no more than 15 m thick and composed of cross bedded sandstone with minor conglomerate containing clasts of oolitic grainstone and volcanics deposited during a period of increased energy in a shallow marine environment. Conformably on top of the Weaner Sandstone, the Battle Creek Formation (80 m thick in outcrop, 179 m thick in drillcore) is composed of interbedded stromatolitic dolostone, mudstone, and siltstone with minor sandstone and chert (Ahmad et al., 2013; Beier et al., 2002a). It is interpreted to be shallow to moderately deeper marine in origin and terminates the Bullita Group (Beier et al., 2002a).

Tijunna Group

Deposition of the Tijunna Group was controlled by basin inversion which resulted in broad lateral thickness variations (Ahmad et al., 2013). Generally, it is thickest in the north-northwest (up to 300 m) and thinnest or absent in the southeast (Ahmad et al., 2013). The Wondoan Hill Formation (30 to 140 m thick) is the older of two formations associated with the Tijunna Group. Its basal cross bedded sandstone unconformably overlies the Bullita Group and grades into thinly bedded glauconitic sandstone, siltstone, mudstone, and black shale commonly containing diagenetic nodules, disseminated pyrite, and galena filled fractures (Ahmad et al., 2013; Beier et al., 2002c). It is interpreted to have been deposited in a shallow to deeper marine environment (Beier et al., 2002c). The uppermost Stubb Formation reaches a maximum thickness of 210 m in the east-central part of the Birrindudu Basin (Ahmad et al., 2013). It is composed of a coarsening upwards sequence of interbedded gray/red claystone, mudstone, and siltstone overlain by sandstone (Ahmad et al., 2013; Beier et al., 2002c). Micro-hummocky cross stratification and slump folding indicate deposition in storm influenced deep waters that inevitably shallowed to a shelf environment and experienced rapid sedimentation (Beier et al., 2002c).

Geochemical Contributions and Discussion

2.1. Introduction

Motivation for reconstructing the paleoenvironments preserved in the ca. 1.7–1.6 Ga McArthur and Birrindudu basins initially arose from the search for viable petroleum reservoirs and economic base metal deposits. The McArthur Basin specifically is host to the worldclass McArthur River lead-zinc deposit and also contains economic hydrocarbon reserves, despite its age (Munson et al., 2020). Putatively eukaryotic microfossils (specifically within the Mallapunyah Formation of the lower McArthur Group) and evidence of hydrocarbon biomarkers in drill core samples have been recovered from the uppermost McArthur, Nathan, and Roper Groups (Brocks, 2018; Javaux and Knoll, 2017). By contrast with the well studied McArthur Basin, the Birrindudu Basin has remained relatively understudied, and the integrated environmental context of both basins has yet to be fully characterized in terms of their overall geochemistry. Investigating the rocks specifically in which microfossils are preserved will therefore provide insight into the habitat and evolution of the earliest complex microorganisms while also contributing to the rapidly changing understanding of the middle Proterozoic oceans and atmosphere.

This chapter presents new iron speciation, total organic carbon content (TOC), and major element geochemistry on shale samples from both the McArthur and Birrindudu Basins. The basins span a

range of depositional environments, and their lack of deformation, metamorphic overprinting, and surficial oxidative weathering make them ideal for geochemical analysis and the preservation of microfossils. The data from this study is presented and discussed within the context of the depositional environments as inferred by the lithofacies encountered in multiple drillcores. Furthermore, the redox conditions at the time of deposition and the preservation potential of individual samples as it relates to TOC are considered, setting up future integration with palaeontological data.

2.2. Methods

2.2.1. Sampling

The suite of shales used in this study consists of 194 samples collected by Leigh Anne Riedman of the University of California, Santa Barbara from 8 exploration drill cores stored at the Northern Territory Geological Survey core repository in Darwin. The samples span the entire stratigraphy of both the McArthur and Birrindudu basins (Figures 2.1 and 2.2). These samples were collected with an emphasis on grey shales considered prospective for microfossils based on previous microfossil studies on Proterozoic rocks (e.g., Woltz et al., 2021). Half of each sample was crushed into a fine ($< 5 \mu\text{m}$) powder using a tungsten carbide ring mill that was cleaned between each sample with pure silica gel and isopropyl alcohol.

2.2.2. Sequential Iron Extraction

The analytical procedure for sequential iron extraction was based on protocols developed by Poulton and Canfield (2005, 2011) and Kunzmann et al. (2015). In addition to the samples in this study, independently analyzed sample powders from the Neoproterozoic black shales in Svalbard were analyzed as quality control standards (Appendix A9; Kunzmann et al., 2015). For each set of analysis, roughly 150 mg of sample powder was weighed directly into a 15 ml centrifuge tube, with the exact mass of the material recorded to 4 four decimal places. At each of the subsequent steps involving pipetting, the reagent or leachate sampled for analysis was also weighed and the exact mass recorded (Appendix A).

The sodium acetate extraction, which targets iron bound to carbonates (FeCarb), was completed first. This extraction was performed by first pipetting 10 ml of 1 M sodium acetate reagent buffered

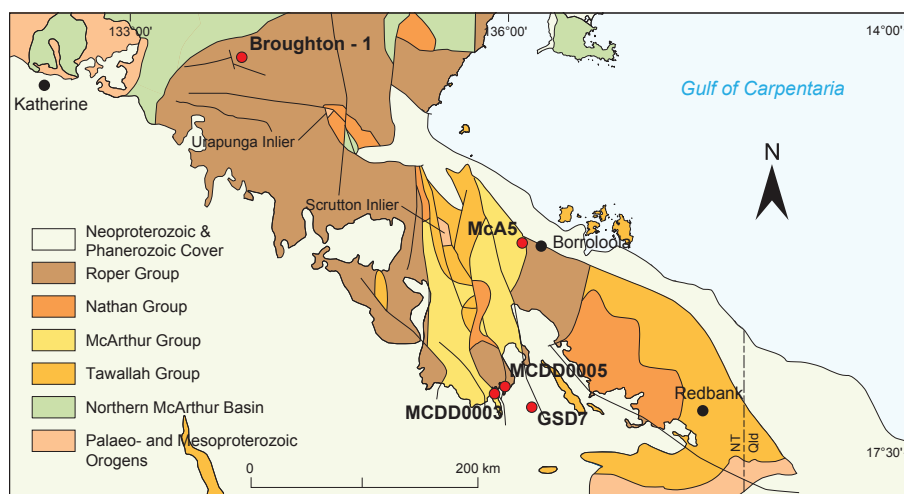


Figure 2.1. Simplified geologic map of the southern McArthur Basin emphasizing the major stratigraphic groups and the location of the drillcores (red points) sampled in this study. Major mapped faults are outlined in black while the black points represent nearby towns. Adapted from Ahmad et al. (2013) and Rawlings (1999).

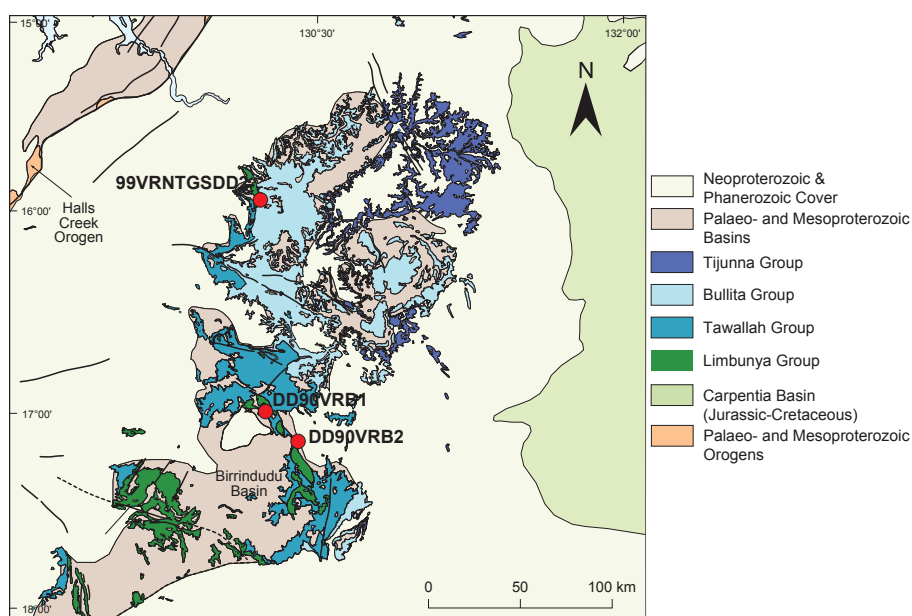


Figure 2.2. Simplified geologic map of the Birrindudu Basin showing the major stratigraphic groups and the location of the drillcores (red points) sampled in this study. Mapped faults are outlined in black while inferred faults are denoted using dashed black lines. Adapted from Ahmad et al. (2013).

with acetic acid to pH 4.5 into each tube. The samples were shaken vigorously to ensure homogenous mixing of the powder, placed vertically on a shake table at 45 °C for 24 hours, then re-placed horizontally on the shake table for another 24 hours at the same temperature. Following the extraction, the samples were centrifuged for roughly 5 minutes at 5000-7000 rpm. Next, without disturbing the solid material, 1 ml of each leachate was transferred to a clean 15 ml tube. The

remaining leachate was then discarded and the residual solid material was rinsed, agitated, and re-centrifuged with 10 ml of nano pure water.

The second extraction requires 50 g/l sodium dithionite buffered with 0.35 M acetic acid and 0.2 M sodium citrate to pH 4.8. This reagent preferentially dissolves Fe-oxyhydroxides (FeOx). First, 10 ml of new leachate is pipetted into the centrifuge tubes from the previous extraction. These are agitated manually to ensure complete mixing, then placed horizontally on a shake table at room temperature for 2 hours. The samples are centrifuged anew before transferring 1 ml of leachate from each sample to a clean tube. The extra leachate is again discarded and the undisturbed solid material rinsed.

For the final extraction, the sample powders are leached using 10 ml of a reagent composed of 0.2 M ammonium oxalate and 0.17 M oxalic acid buffered with ammonium hydroxide to pH 3.2. This step targets the mixed-valence iron minerals, particularly magnetite in ancient shales (FeMag). The tubes are placed on a shake table at room temperature for at least 6 hours before they are centrifuged and 1 ml of leachate is removed for analysis.

The leached solutions were analyzed using a PerkinElmer AAnalyst 100 Flame Atomic Adsorption Spectrometer (AAS) that was calibrated using eight calibration solutions with iron concentrations ranging from 0 to 30 ppm prepared by diluting SCP iron element solution with an initial concentration of 1003 ppm +/- 6 µg/ml in 2% nitric acid. Each sample was prepared for analysis by adding 9 ml of 2% nitric acid (with the exact mass of the added acid weighed and recorded) to each of the tubes. Using the masses recorded from each of the above steps, the dilution factor and the concentration of iron was calculated for every leachate (Appendix A).

Measurement precision was generally better than 3 % (standard error of the mean) for all analyses, with the exception of G306-150 which is due to one anomalous extraction in Ext. 2 (Appendix A9) rather than an inherent problem in the reproducibility of the results. Machine accuracy was calculated to be within 2% based on replicate measurements of reference materials. Other sources of error include inherent sampling biases which are discussed in detail in Section 2.4.1.

2.2.3. Reduced Inorganic Sulfur Determination

Reactive iron is commonly replaced by pyrite in sulfate-rich marine environments. As a proxy for euxinia, reduced inorganic sulfur phases (i.e. pyrite sulfur) in ancient shales can be liberated and

quantified using a chromium chloride digestion procedure developed by Canfield et al. (1986). For this procedure, a series of five glass digestion vessels are attached to glass condensers and individual nitrogen gas bubbling tubes using ground glass and/or teflon attachments. The condensers are themselves attached using teflon tubes to individual glass traps containing roughly 30 ml of zinc acetate solution used to trap gaseous H₂S generated during the reduction procedure.

The reaction is performed by flushing the system with N₂ and injecting roughly 12 ml of both 1.0 M chromous chloride solution and concentrated HCl to the digestion flasks containing roughly 0.2 to 2.0 g of sample powder, the mass varying based on the estimated pyrite content of each sample. The samples are then heated to roughly 80 °C while N₂ is continuously bubbled through the system at roughly 2-3 bubbles per second for approximately 1.5 to 2 hours.

The resulting zinc precipitate is then tritrated from the trapping solution by adding roughly 1 ml of Ag-nitrate to the glass vessel to form Ag₂S. The traps are then sealed and stored in a dark place until the samples are rinsed and filtered using roughly 2-5 mL of NaOH and a vacuum pump to ensure all Ag₂S is collected. The samples are dried overnight in an oven and then weighed with the exact mass of Ag₂S recorded for each sample (FePy) (Appendix A).

The amount of highly reactive iron (FeHR) for each sample can then be calculated using the equation $FeHR = FeCarb + FeOx + FeMag + FePy$ (Appendix A). By comparing the highly reactive iron pool calculated above (iron available for reductive dissolution processes) to the total iron pool measured from bulk rock geochemistry (including unreactive iron via detrital fluxes) using the ratio $FeHR/FeT$ oxic or anoxic conditions can be determined. Samples with ratios < 0.22 are considered oxic and ratios > 0.38 are considered anoxic while intermediate values between 0.22 and 0.38 are ambiguously oxic or anoxic (Raiswell and Canfield, 1998). Samples can be further quantified as anoxic and euxinic using the proportion of highly reactive iron that has been sulfidized according to the ratio $FePy/FeHR$, where ratios > 0.8 in conjunction with $FeHR/FeT > 0.38$ imply euxinia at the time of deposition (Raiswell and Canfield, 1998; Sperling et al., 2013).

2.2.4. Total Organic Carbon Content

The total organic carbon (TOC) for each sample was measured after first decarbonating the samples using 10 ml of 6 M HCl and 1 g of sample material to remove carbonate-bound carbon. The samples were then agitated for 12 hours and centrifuged, after which the acid was discarded. This

step was repeated as necessary for samples with high carbonate contents. After all carbonate was removed, the samples were rinsed multiple times with 15 ml of distilled water, agitated, centrifuged, and decanted until the pH reached about 5, after which they were dried overnight at 60 °C. In preparation for analyses, between 10 and 12 mg of decarbonated sample was weighed into tin capsules. Individual concentrations of carbon and nitrogen were then measured using an Eltra CS 800 Elemental Analyzer at Geotop Laboratories. Research are reported as weight percentages (Appendix A).

2.2.5. Major Element Geochemistry

For whole rock major elemental analysis, approximately 3 g splits of sample powders were sent to Actlabs (Ancaster, Ontario) where they were prepared as fused glass beads using a mixed lithium metaborate/tetraborate flux. The beads were then digested in a weak nitric acid solution to ensure complete digestion of major oxides, refractory minerals, and rare earth elements. Prepared samples were analyzed for major element concentrations by X-Ray Fluorescence (XRF) and the results recorded in weight % (Appendix B). Internationally certified reference materials that were processed along with samples during X-ray fluorescence analyses reported measured values within 10 % of their reported values for elements that were well above the analytical detection limits including Si, Al, Fe, Mn, Mg, Ca, Na, K, Ti, P, and V (Appendix B18). Trace elements including Cu, and Co were below the XRF detection limit and were analyzed separately alongside Mo, Cr, V, Ni, Zn, and Mo however this data is not included here and will not be discussed.

2.3. Results

2.3.1. Sedimentary Geochemistry of the Greater McArthur Basin

Raw analytical data, standard error, and conversions are recorded in tables A1 through A19 included in Appendices A, B, and C. Iron speciation chemistry was applied in this study as the primary proxy for water-column redox state at the time of sediment deposition. The highly reactive iron to total iron ratios (Fe_{HR}/Fe_T) are presented alongside the ratio of iron in pyrite to highly reactive iron (Fe_{Py}/Fe_{HR}), the ratio of total iron to aluminum (Fe_T/Al), total manganese normalized to aluminum, total phosphorous, and TOC measured in weight % (wt. %). Depositional

environments inferred from sedimentary structures and lithologies indicative of water depth are included on each plot (Figures 2.3 to 2.10).

The ratio of $FePy/FeHR$ is a measure of how much reactive iron has been converted to pyrite. For an environment to be considered euxinic, $FePy/FeHR$ ratios must exceed 0.8, implying close to full pyritization of reactive iron, which is only possible where free sulfide exists in the water column due to bacterial sulfate reduction (Poulton et al., 2004; Poulton and Canfield, 2011). FeT/Al serves as an additional measure of oceanic redox state by normalizing FeT to the aluminum content, thereby accounting for detrital iron contribution. Relative to modern sediments, FeT/Al ratios < 0.5 are considered oxic, whereas ratios above 0.5 are considered anoxic due to excess iron mainly via the addition of hydrogenous iron (Lyons and Severmann, 2006), though as discussed below, this threshold should be considered variable depending on lithology and provenance.

The Tawallah Group (McArthur Basin)

The lowermost Tawallah Group of the McArthur Basin is represented in drillcores GSD7 and MCDD0003, which together span roughly 565 m of stratigraphy. Samples for this study are primarily from light to dark grey fissile siltstones, mudstones, and shales, some of which contain cm-scale carbonate nodules and structures and textures indicative of evaporative conditions (Figures 2.3 and 2.4). Based on the iron speciation data and sedimentological observations, the lower Tawallah Group records deposition in a range of settings from oxic to anoxic and/or euxinic in environments spanning supratidal to offshore. The majority of samples exceeding $FeHR/FeT$ ratios of 0.38 are found to represent deeper water facies with reactive iron largely associated with carbonates. Samples with $FeHR/FeT < 0.38$ predominantly represent supratidal to intertidal zones, though there are some anoxic outliers in these settings. FeT/Al values show minor variations that are generally consistent with iron speciation data. Collectively, the data indicate that the basin was effectively sulphide-depleted at this time but experienced a transient interval of deep water euxinia during the deposition of the organic-rich shale of Unit 3 of the Wollgorang Formation. This period is associated with increases in TOC to values as high as 4.4 wt. % and concurrent manganese depletion (Figure 2.3), followed by a return to low TOC and recovery of Mn concentrations. Phosphorus content appears to be decoupled from TOC enrichments in the lower Tawallah Group, although the highest TOC values recorded in Wollgorang Unit 3 are associated with P as high as 231 ppm (P

2. Geochemical Contributions and Discussion

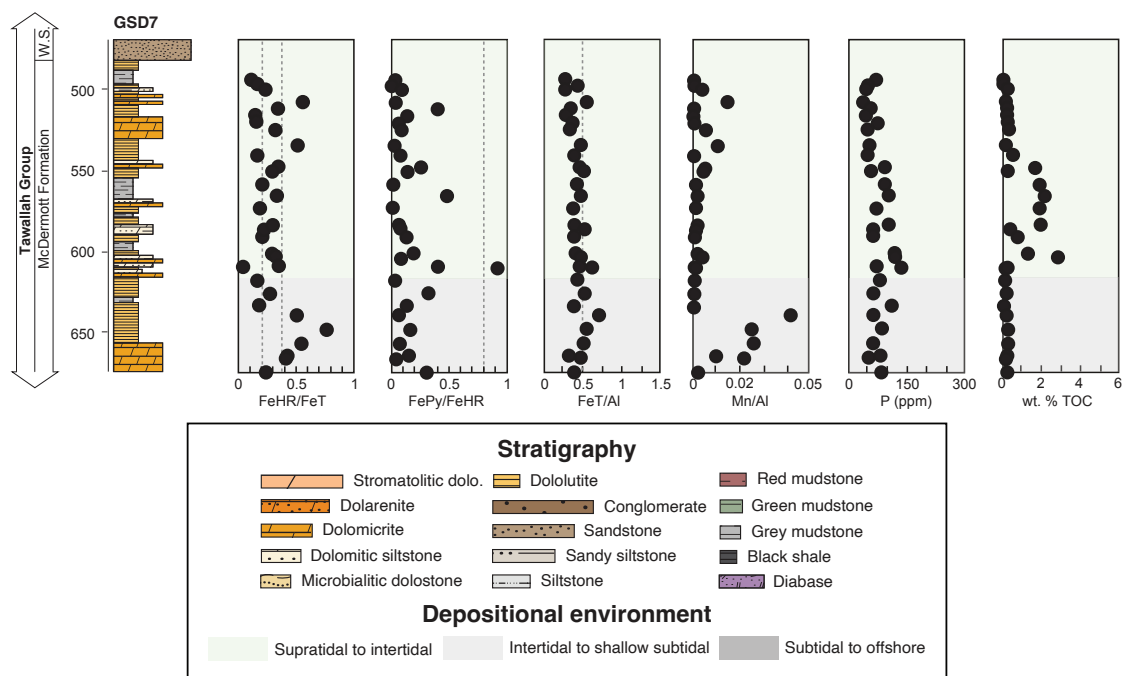


Figure 2.3. Redox proxy data and TOC of the drillhole GSD7 from the McArthur Basin spanning the middle Tawallah Group. Plots from left to right: highly reactive iron over total iron, pyrite iron over highly reactive iron, total iron over aluminum, total iron, total manganese normalized to aluminum, total phosphorous, and weight percent TOC. Dashed lines represent baseline values of 0.22 and 0.38 for $FeHR/FeT$, 0.5 for FeT/Al , and 0.8 for $FePy/FeHR$. Depositional environments are overlain on each plot with colour references included in the stratigraphy legend on the right. Note x-axis scale relative to other sections.

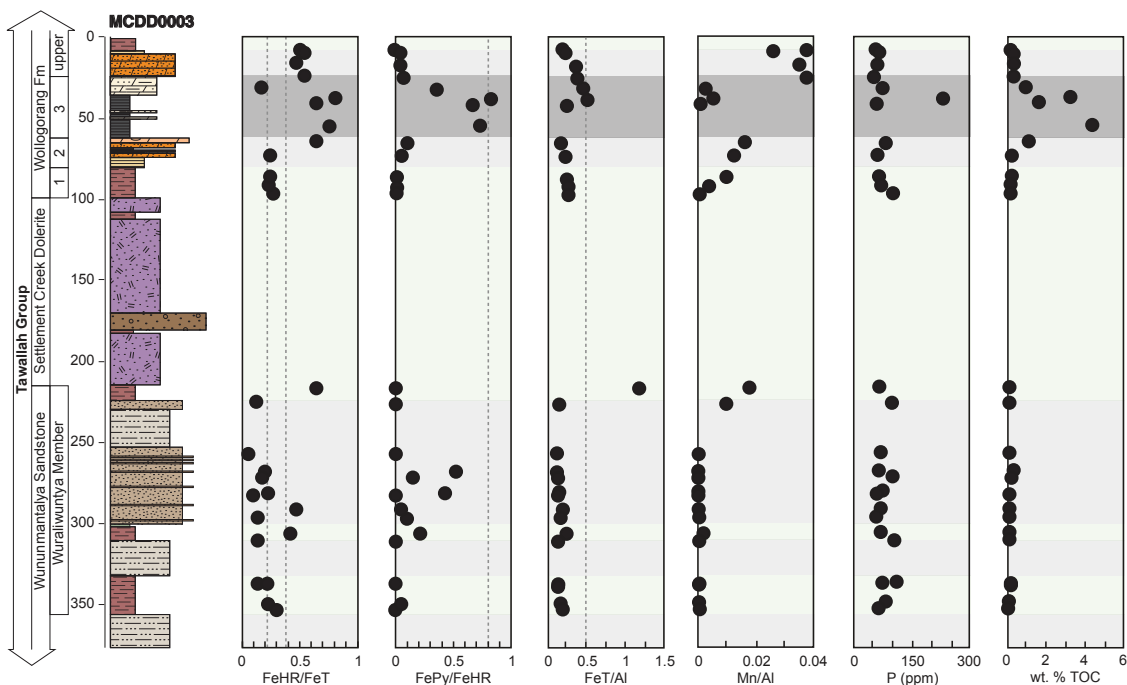


Figure 2.4. Redox proxy data and TOC of the drillhole MCDD0003 from the McArthur Basin spanning the upper-middle Tawallah Group. Stratigraphic section adapted from Kunzmann et al. (2020). Legend as in Figure 2.3.

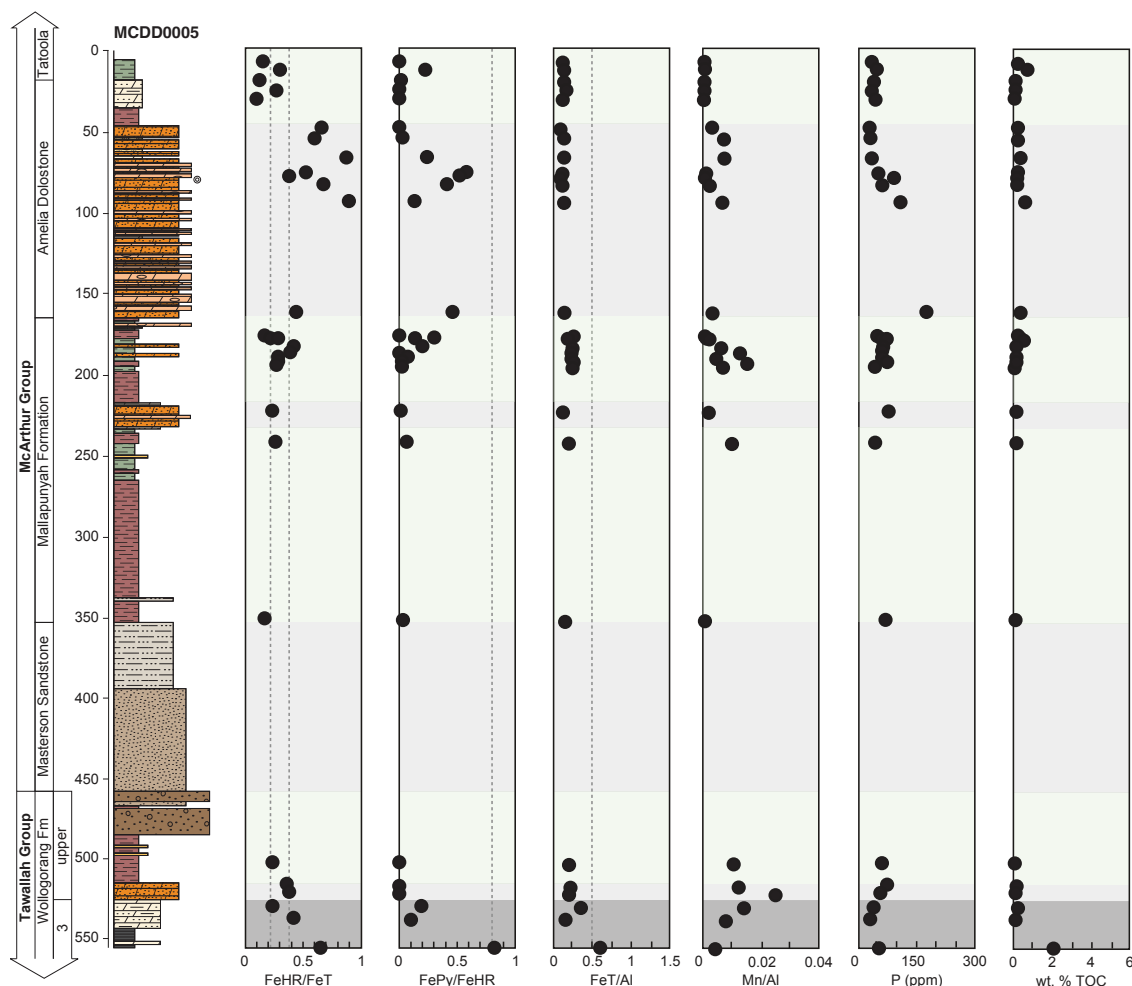


Figure 2.5. Redox proxy data and TOC of the drillhole MCDD0005 from the McArthur Basin spanning the lower and middle Umblooga Subgroup of the lower McArthur Group. Stratigraphic section adapted from Kunzmann et al. (2020). Legend as in Figure 2.3.

data is unavailable for one of the high TOC samples) while the average hovers around 75.8 ppm ($n = 59$) otherwise.

The McArthur Group (McArthur Basin)

Drillcores MCDD0005 and McA5 span the uppermost Tawallah Group as well as the McArthur Group of the McArthur Basin (Figures 2.5 and 2.6). They intersect approximately 925 m of stratigraphy and a broad range of facies that overall record deepening upsection into drillcore McA5. Geochemistry was performed on samples consisting of light grey/green or medium grey, finely laminated mudstones with occasional evaporitic textures and flecks of dark material inferred to be organic matter in drillcore MCDD0005 and primarily medium to dark grey silty mudstones and

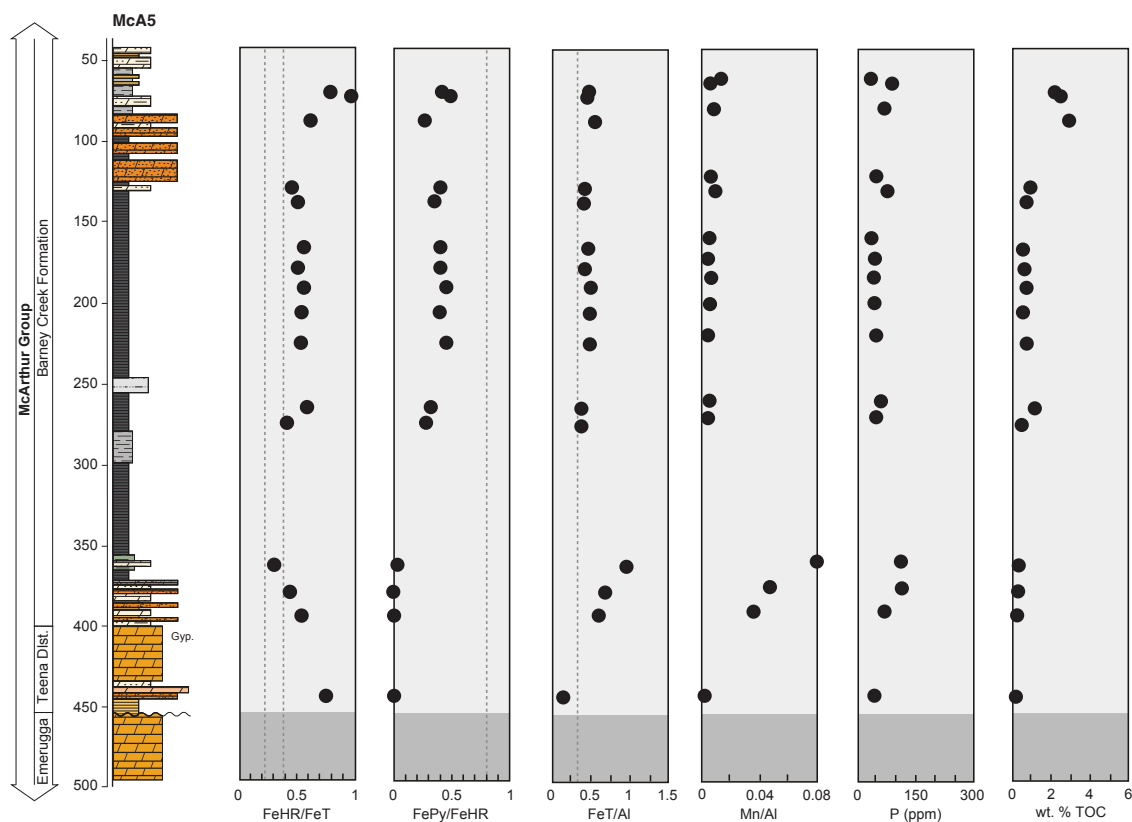


Figure 2.6. Redox proxy data and TOC of the drillhole McA5 from the McArthur Basin spanning the Barney Creek Formation of the upper McArthur Group. Stratigraphic section adapted from Schmid (2016). Legend as in Figure 2.3. Note x-axis scale increase in the column representing Mn/Al.

shales throughout McA5. Iron speciation results coupled with FeT/Al , Mn, and low TOC indicate deposition of the Wunnumantyalu Sandstone in an oxic realm, although anoxic and ferruginous values persist upsection into the deep water shales of the uppermost Tawallah Group and the black shales of the Barney Creek Formation, which is generally organic-rich, was deposited below storm wave base, and is locally mineralized (Pb and Zn). $FeHR/FeT$ values below 0.38 are generally associated with low $FePy/FeHR$, while anoxic samples have higher $FePy/FeHR$. FeT/Al values remain below 0.5 for the bulk of drillcore MCDD0005 despite the associated presence of anoxic values produced via sequential extraction of iron. These values become more consistent throughout drillcore McA5 where they generally remain above 0.5. Mn/Al ratios return to values generally below 100 ppm throughout the greater part of the deposition of the lower McArthur Group. Low TOC (ave = 0.20; n = 26) is also noted, while P content increases at the base of the Amelia Dolostone (Figure 2.5). The Barney Creek Formation also shows increased Fe, Mn, and P that is decoupled from TOC, which increases to values above 2 wt. % in the uppermost portion of the formation (Figure 2.6).

The Roper Group (McArthur Basin)

The Broughton-1 drillcore covers roughly 550 m of stratigraphy through the Roper Group, 380 m of which is represented by samples in this study that comprise medium to dark grey siltstones and wavy-laminated, red and green shales associated with carbonate breccias (Figure 2.7). Facies indicate that samples were deposited at increasing water depths upsection, while iron speciation data imply primarily oxic conditions with no correlation to water depth. $FePy/FeHR$ ratios are consistently very low (ave = 0.0501; n = 36) indicating the continued persistence of a sulphide depleted water column. FeT/Al results in this drillcore are in contradiction with iron speciation findings: samples inferred to represent oxic depositional settings based on $FeHR/FeT$ at 112.92 m, 122.3 m, 158.1 m, and 307.1 m display $FeT/Al > 0.5$, whereas ferruginous samples display $FeT/Al > 0.5$. Manganese and P are notably depleted throughout the Roper Group with average values of 27 ppm and 28 ppm respectively. TOC in these samples does not exceed 1 wt. % with an average of 0.18 wt. % and a maximum of 0.73 around 250 m depth.

Limbunya Group (The Birrindudu Basin)

Together, drillcores DD90VRB2 and DD90VRB1 intersect approximately 495 m of the Limbunya Group, the lowermost strata in the Birrindudu Basin (Figures 2.8 and 2.9). Sampled lithologies include grey/green mudstones and shales sometimes further associated with red mudstone, dolomicrite, dolostone, and/or dolomite. Depositional settings alternate between supratidal to subtidal throughout the lower Limbunya Group, which then transition upsection towards offshore environments in the Fraynes Formation. Iron speciation data indicate redox conditions that fluctuated from oxic to anoxic, while sulfate was generally depleted throughout deposition of the Margery Formation and into the Amos Knob Formation. However, lack of enrichment in Mn and associated low TOC values likely indicate a persistently oxygenated setting. This inference is further supported by $FeT/Al < 0.5$. Oxic deposition probably continued upsection into the Blue Hole Formation, whereas black shales in the uppermost Fraynes Formation display $FeT/FeHR$ ratios exceeding 0.38 but FeT/Al values well below 0.5. They are interpreted to have been deposited under an anoxic water column with the low FeT/Al ratios indicating a decrease in detrital iron content. Phosphorus shows some variability in the Margery Formation, although values are generally low. TOC follows this trend

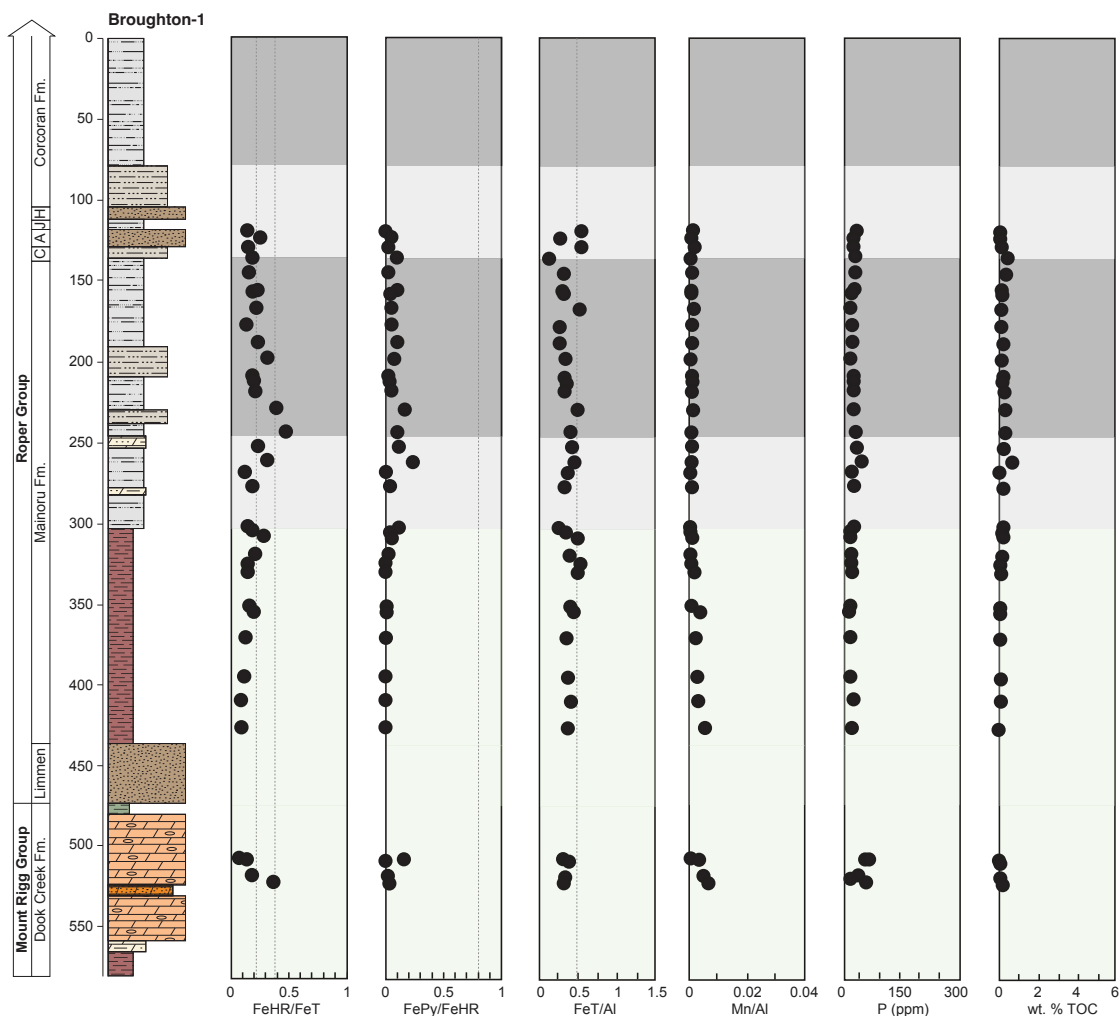


Figure 2.7. Redox proxy data and TOC of the drillhole Broughton-1 from the McArthur Basin spanning the lower Roper Group. Legend as in Figure 2.3.

with an overall average of 0.2 wt. % throughout the Limbunya Group that increases in Fraynes Formation black shales.

Bullita and Tjunna Groups (The Birrindudu Basin)

The Bullita and Tjunna groups of the upper Birrindudu Basin are intersected by drillcore 99VRNTGSD2. Samples included in this study span roughly 277 m and comprise mainly grey/green to dark grey fissile mudstones and siltstones. Iron speciation data indicate only oxic depositional settings, corresponding to intertidal to shallow subtidal environments. Two equivocal samples have $FeHR/FeT$ ratios of 0.24 and 0.27. $FePy/FeHR$ ratios are lowest in this subset with an average of approximately 0.02, indicating negligible free sulfide in the water column at the time of deposition.

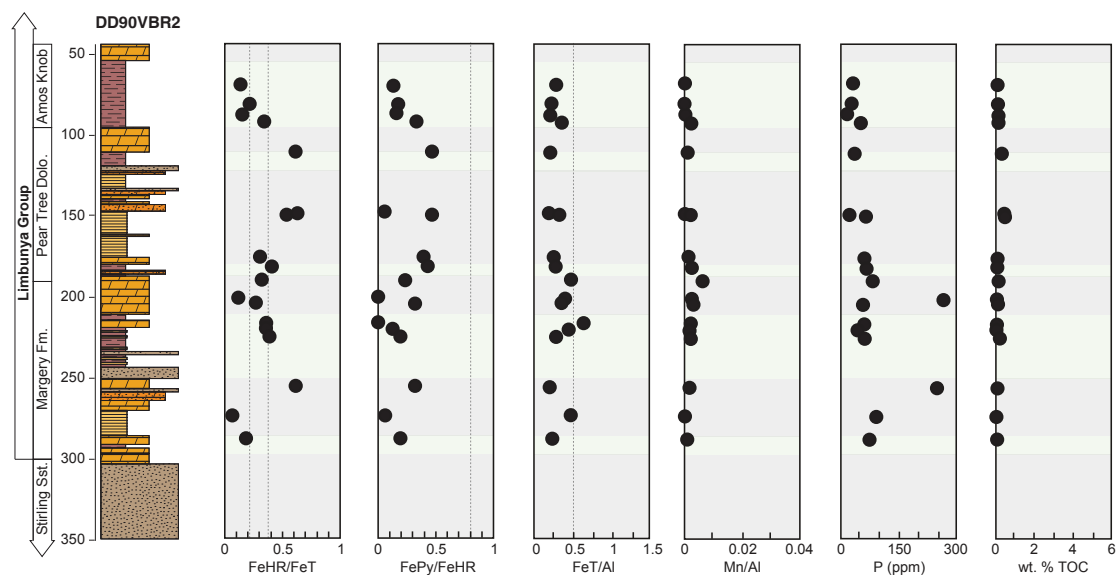


Figure 2.8. Redox proxy data and TOC of the drillhole DD90VRB2 from the Birrindudu Basin spanning the lower Limbunya Group. Legend as in Figure 2.3.

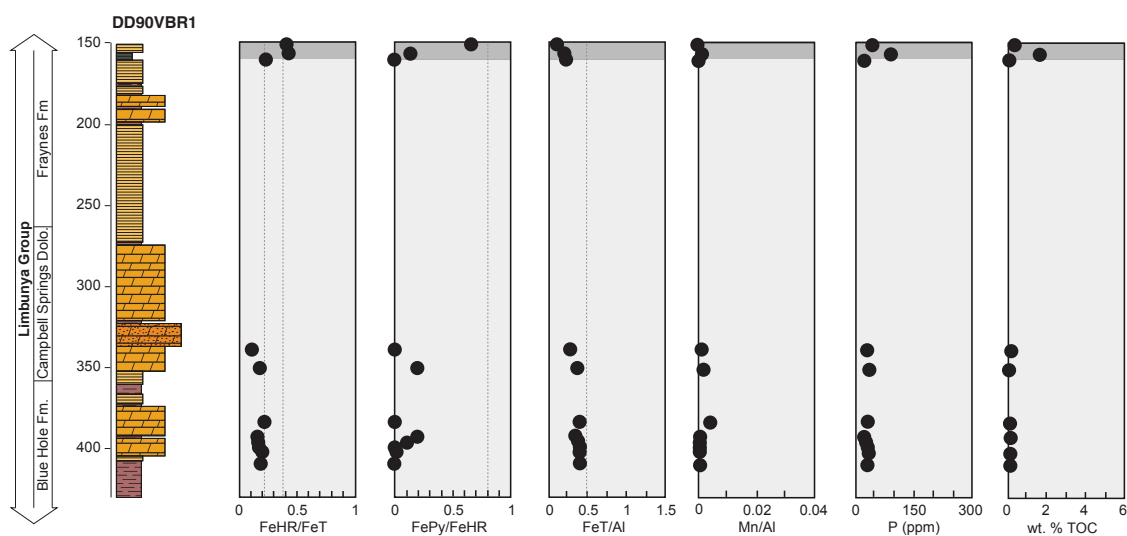


Figure 2.9. Redox proxy data and TOC of the drillhole DD90VRB1 from the Birrindudu Basin spanning the upper Limbunya Group. Legend as in Figure 2.3.

FeT/Al values are mostly consistent with iron speciation results, although four anoxic samples are observed at 94.7 m, 115.6 m, 122.27 m, and 216.9 m. The values, however, are directly correlated with increased total iron, likely reflecting an increase in detrital rather than authigenic iron phases. This is further supported by a lack of associated enrichment in Mn. TOC content of the Bullita and Tijnuna groups is markedly low with an average of 0.18 wt % and a maximum of 0.64 wt. %. P displays essentially no variation throughout deposition of the Bullita and Limbunya Groups with

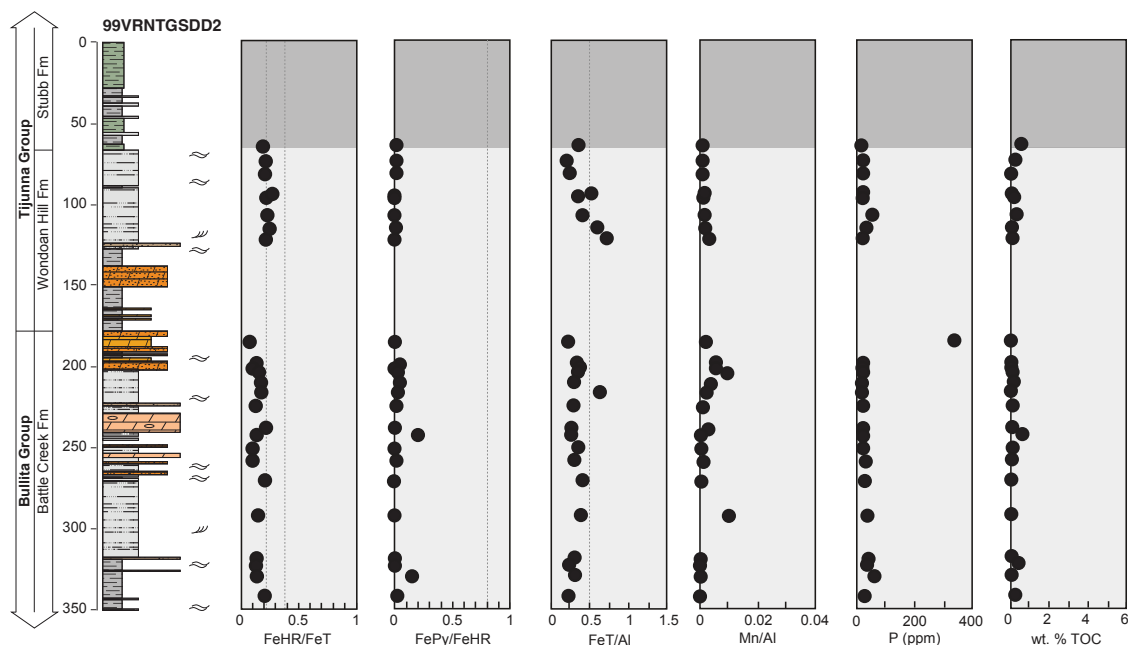


Figure 2.10. Redox proxy data and TOC of the drillhole 99VRNTGSDD2 from the Birrindudu Basin spanning the upper Bullita and lower Tijunna Groups. Stratigraphic section adapted from Cutovinos et al. (2002). Legend as in Figure 2.3.

the exception of a single point in the upper Battle Creek Formation with a P concentration of 266 ppm (Fig. 2.3).

2.3.2. Major and Trace Element Distributions

Whole rock geochemical data is presented using cross-plots of major element oxides showing strong positive or negative correlation based on their interelemental Pearson correlation coefficients (r) as shown in the correlation matrices in Appendix C (Lee Rodgers and Nicewander, 1988). Where r is less than or equal to -0.5 a strong negative correlation is inferred, while r values greater than or equal to 0.5 are considered strongly positively correlated. Shales are generally composed of a mixture of three major end member oxides including SiO_2 representing detrital or biogenic quartz, Al_2O_3 indicative of clay content, and CaO reflecting the carbonate content. In the Greater McArthur Basin, silica concentrations maintain an average of 54.8 %, which is similar to the 58.9 % of the average shale described by Wedepohl (1971). The samples examined also display an overall enrichment in silica compared to Al_2O_3 and CaO , which present averages of around 15.6 % and 3.94 %, respectively (Figure 2.11A). While variably elevated silica concentrations are found throughout the dataset, drillcores Broughton-1 and 99VRNTGSDD2 have a higher proportion of values

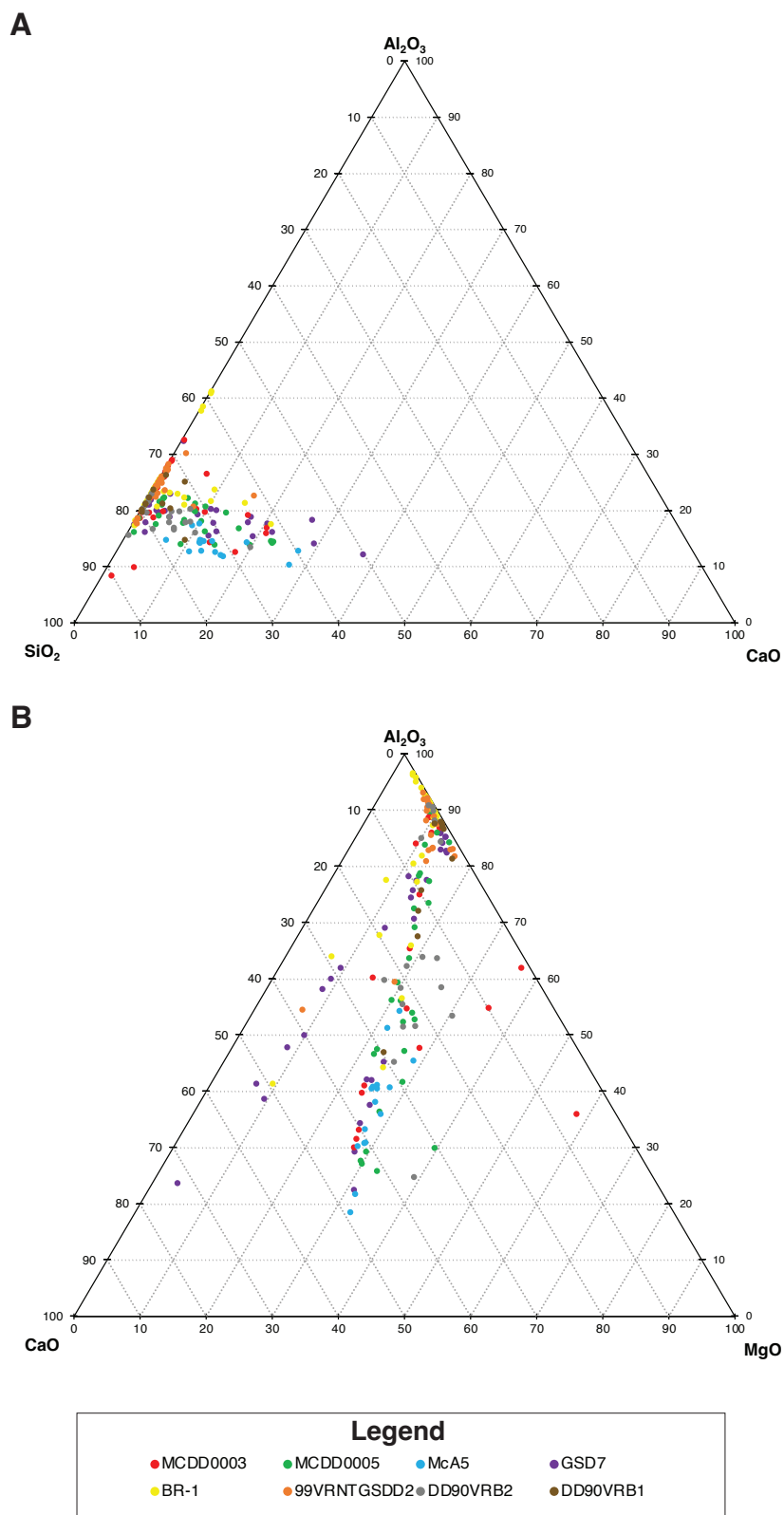


Figure 2.11. Ternary diagrams showing the relative abundances of (A) Al_2O_3 , SiO_2 , CaO , and (B) Al_2O_3 , CaO , MgO in shales from the Greater McArthur Basin.

2. Geochemical Contributions and Discussion

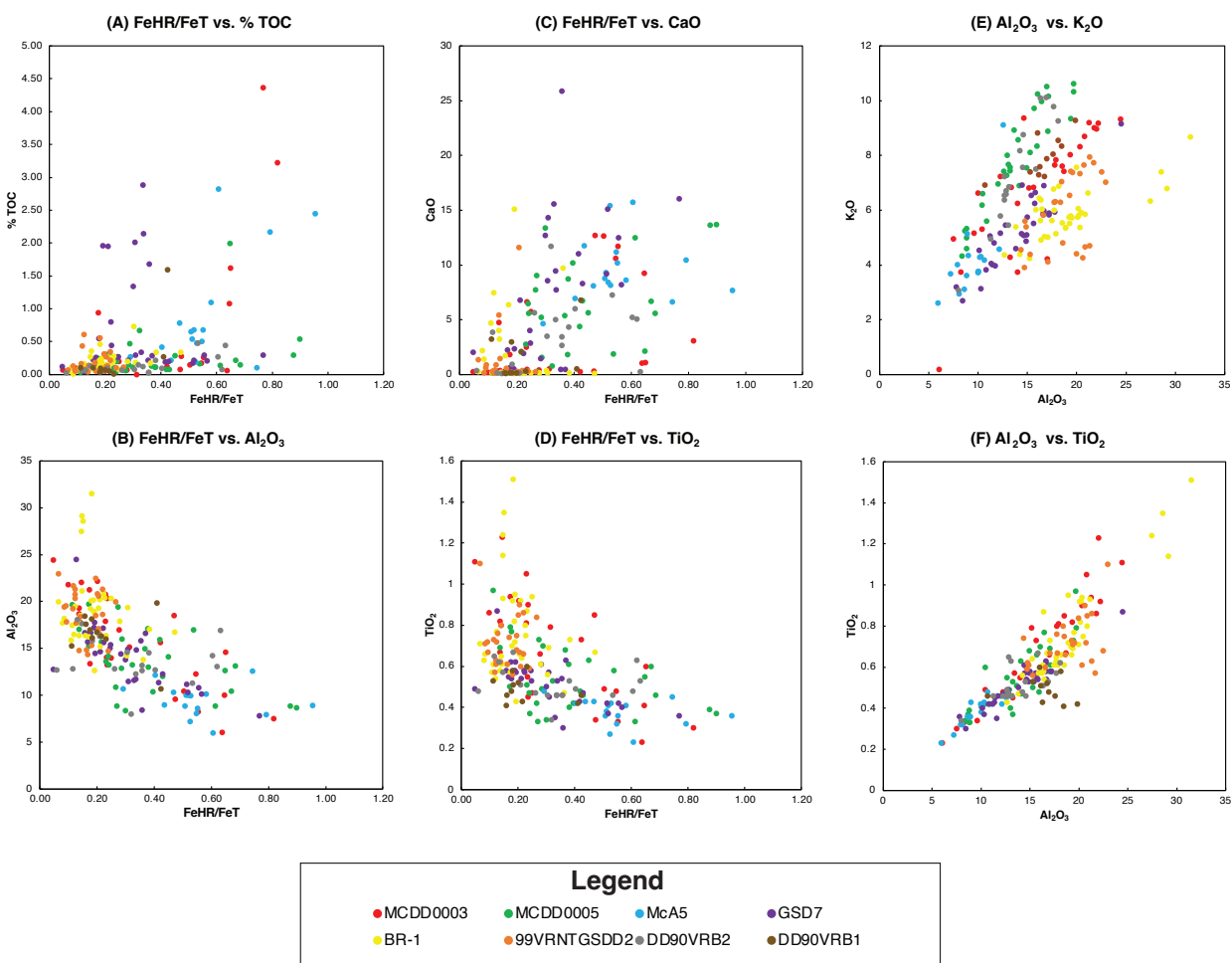


Figure 2.12. Cross plots displaying covariation between $FeHR/FeT$ and (A) TOC; (B) Al_2O_3 ; (C) CaO; (D) TiO_2 and Al_2O_3 and (E) K_2O ; (F) TiO_2 for all eight drillcores. Major element oxides and TOC are measured in weight % while $FeHR/FeT$ is unitless.

exceeding the average, whereas consistently lower values ($< 54\%$) are observed in drillcores McA5 and GSD7. Clay content, inferred from Al_2O_3 abundance, varies throughout the dataset, though the highest values (as high as 31.51%) are again observed in drillcore Broughton-1. Elevations in CaO abundance are present in almost every subset of samples possibly illustrating sampling of dolomitic siltstones and/or dolomite interbeds given an association with higher MgO (Figure 2.11B).

Reactive iron ratios are positively correlated with TOC (ave $r = 0.590$) throughout the stratigraphy, with the exception of drillcores GSD7 and 99VRNTGSD2, which display r values of -0.053 and 0.097, respectively (Figure 2.12A). A weaker positive correlation is observed between $FeHR/FeT$ and CaO ($r = 0.57$; Figure 2.12B). Furthermore, highly reactive iron is shown to be decoupled from

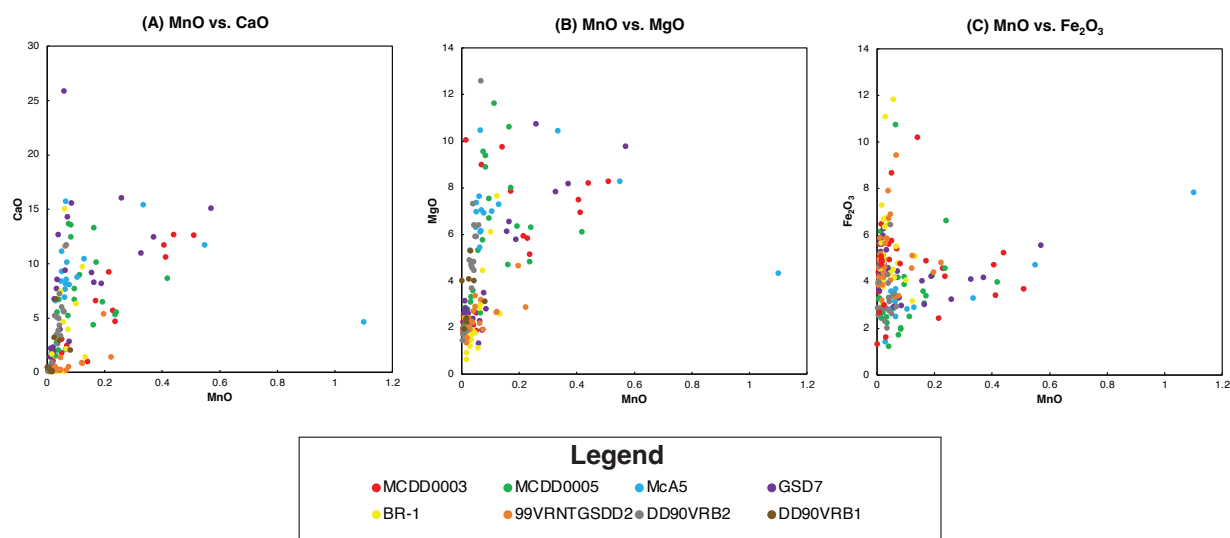


Figure 2.13. Cross plots displaying covariation between MnO and (A) MgO; (B) CaO; (C) Fe₂O₃ for all eight drillcores. All values are in weight %.

Al₂O₃ ($r = -0.67$) and TiO₂ ($r = -0.53$) (Figures 2.12C and 2.12D). These results suggest increased iron associated with calcareous samples and an inverse relationships for increased siliciclastic input. Detrital influence is further reflected in the strong coupling of Al₂O₃ and TiO₂ ($r = 0.88$) as well as Al₂O₃ and K₂O ($r = 0.52$; Figures 2.12E and 2.12F). These data confirm a relatively constant detrital source and limited winnowing effects (Ross and Bustin, 2009).

Manganese is a redox sensitive trace element that is commonly present at higher concentrations in ferruginous environments and can also be easily incorporated into carbonate minerals. A trend is observed between MnO and both CaO and MgO, indicating some free dissolved manganese is incorporated into carbonate rocks (Figures 2.13A and 2.13B). A weak positive correlation is seen between MnO and Fe₂O₃ where increased Mn is associated with increased iron, although increases in iron do not necessarily equate to an enrichment of manganese. This pattern is likely a result of the tendency for Mn to diffuse back into the water column in reducing environments (Tribovillard et al., 2006).

2.3.3. Trace Metal Enrichment Factors

Average trace metal enrichment factors (EF) relative to the average shale (AS) as defined by (Wedepohl, 1971) for each drillcore are also shown according to equation 2.1 where X is the

$$EF_X = \frac{\frac{X}{Al\ Sample}}{\frac{X}{Al\ AS}} \quad (2.1)$$

concentration of any trace element measured in parts per million (ppm) normalized to aluminum content in the same sample. Where $EF > 1$, an element is considered enriched relative to average shales, while $EF < 1$ indicates depletion.

While there is a general decreasing upsection trend in the average EF's calculated for trace metals in both the McArthur and Birrindudu basins, values overall indicate trace metal depletion (Figure 2.14). Both Co and Cr are omitted in the compilation due to concentrations below detection limits (Appendix B). A notable exception to the overall depletion is enrichments in Mn in drillcore McA5. Variable enrichments also occur on a sample-by-sample basis throughout the older strata in both basins, particularly in samples determined to have been deposited in anoxic environments based on iron speciation data.

2.3.4. Chemical Index of Alteration

The chemical index of alteration (CIA) was calculated for each sample using equation 2.2 where CaO^* represents the molar fraction of CaO in silicates quantified by $Na_2O/(0.9286)$ assuming CaO

$$CIA = \left(\frac{Al_2O_3}{Al_2O_3 + CaO^* + Na_2O + K_2O} \right) * 100 \quad (2.2)$$

behaves conservatively with respect to sodium (Kronberg et al., 1986; Nesbitt and Young, 1982). The CIA is a measure of the degree weathering experienced by the source material of a sediment sample. The principle behind this proxy is that during chemical weathering, Ca, Na, and K are preferentially leached by hydrolysis reactions, while Al is retained. Therefore, high CIA values are indicative of higher levels of chemical weathering. Values less than 70 are typically considered relatively unweathered, while values above 75 indicate a more weathered provenance (Nesbitt and Young, 1982; Sperling et al., 2013). In this study however, samples were only decarbonated for TOC analyses therefore making CaO content an overestimation resulting in the calculated CIA representing a minimum estimate of the degree of weathering.

The CIA calculated for each sample remain low (below 75) with averages for each drillcore shown in Figure 2.15. Values above 70 occur in drillcores Broughton-1 and 99VRNTGSDD2, while slightly

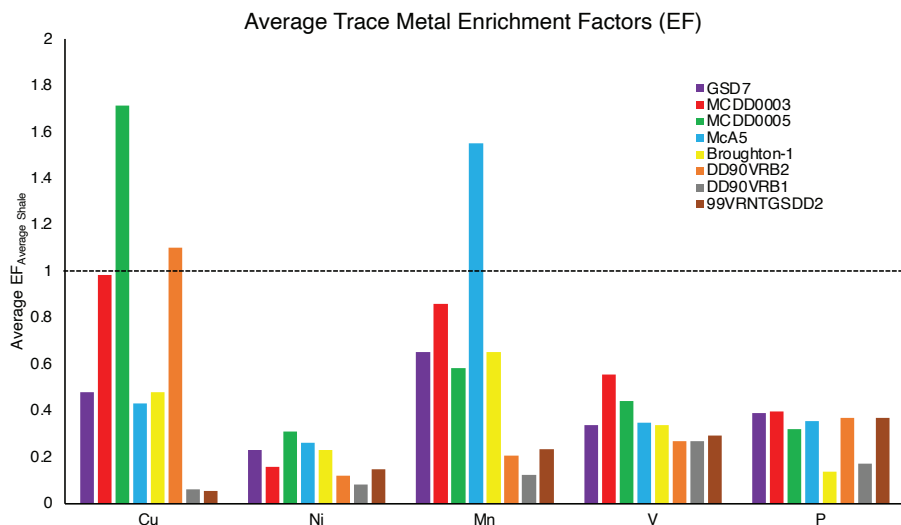


Figure 2.14. Average enrichment factors for selected redox sensitive elements for each drillcore.

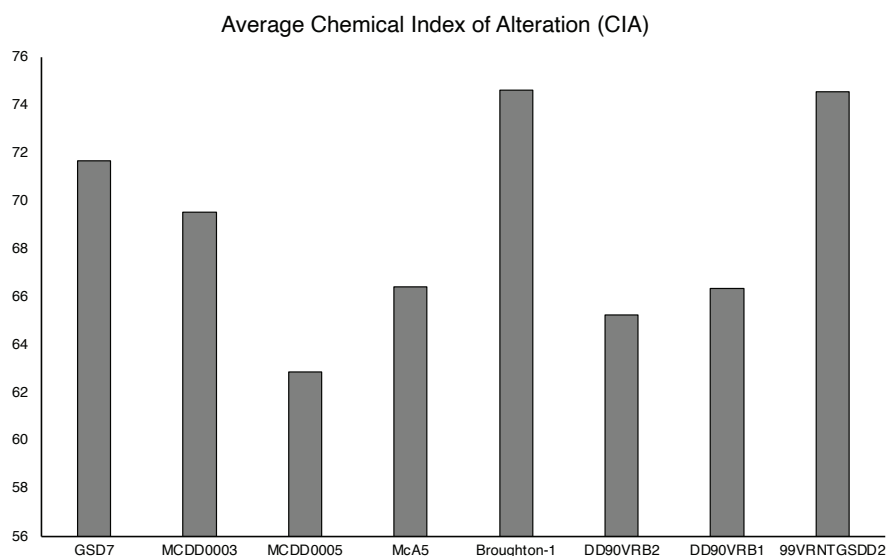


Figure 2.15. Average CIA of each drillcore.

less intensely weathered samples are found in GSD7.

2.4. Interpretations and Discussion

2.4.1. Redox Structure of the Greater McArthur Basin

Due to its excellent preservation and the abundance of drill core available, the McArthur Basin is a common target for studies aiming to reconstruct middle Proterozoic environments. Several previous

studies have applied the iron speciation method to the McArthur basin in order to reconstruct Paleoproterozoic marine redox stratification although data is still very scarce (Planavsky et al., 2011; Poulton et al., 2010; Shen et al., 2002). Early studies, based mainly on analyses of black shales of the Barney Creek Formation, suggested pervasive euxinia, which was cited as evidence in support of a broadly euxinic middle Proterozoic deep ocean (Canfield, 1998; Shen et al., 2002). However, iron speciation methods have since been updated (Poulton and Canfield, 2005) and more recent studies seem to support localized euxinic episodes, consistent with the now more accepted view that the middle Proterozoic deep ocean was not everywhere euxinic (Cox et al., 2016; Planavsky et al., 2011). However, all of the previous studies, like many studies of Proterozoic ocean redox, have targeted organic-rich, deepwater sediments, such as the black shale members of the Wollongorang Formation, the Barney Formation, and the Roper Group and included measurements of sulfur isotopes as well as the degree of pyritization (Cox et al., 2016; Johnston et al., 2008; Shen et al., 2002). While a reasonable approach to inferring deepwater conditions, this approach does not provide a three-dimensional picture of basin redox structure for the basin at any given time and risks missing synoptic variability between anoxic and euxinic conditions.

The sampling method used in this study was designed to target facies most likely to contain microfossils. As such we have analyzed sediments deposited in nearshore, siliciclastic settings, as well as deep water settings, thereby providing a more complete view of the redox structure across environments. The nature of this sampling method provides a source of error and an inherent bias towards siliclastic rocks which are prone to oxic results through overwhelming siliclastic as opposed to authigenic iron. Some samples contain elevated calcite or dolomite relative to the average shale (Wedepohl, 1971, Figures 2.11A and 2.11B;) which is known to affect iron speciation readings as the method is designed for siliciclastic rocks. However, it was recently discovered, that should carbonaceous shales contain enough iron, interpretation of the data should not be affected (Clarkson et al., 2014).

Samples displaying evidence of deposition under oxic conditions are generally associated with deposition in the intertidal zone in the Greater McArthur Basin (Figure 2.16). This may also suggest a shallow redoxcline, which would be expected if atmospheric oxygen was low during this time (Wang et al., 2022). In aggregate our results indicate that throughout most of its history, the McArthur Basin was a redox stratified basin with generally oxic surface waters and anoxic and ferruginous

bottom waters (Figure 2.16). These results are consistent with the emerging view of the middle Proterozoic ocean (Planavsky et al., 2011; Reinhard et al., 2013), and provide concrete evidence aligning with prior redox studies on the McArthur Basin (Cox et al., 2016; Poulton et al., 2010; Shen et al., 2002).

Deep water black shales are found in the Tawallah Group (Figure 2.5) as well as in the Barney Creek Formation (Figure 2.6). Multiple redox proxies recorded in the upper Tawallah Group suggest a change in the redox conditions or depositional environment sometime around 1730 Ma (Page et al., 2000), where it is possible the basin underwent a period of localized euxinia. This period is further associated with higher TOC —likely related to elevated primary productivity— as well as high P

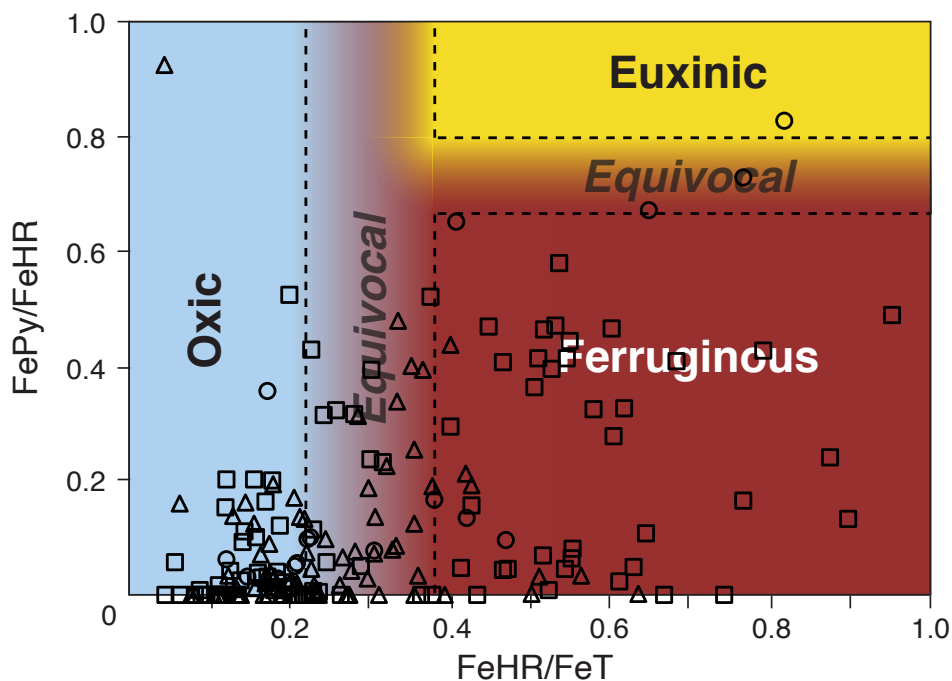


Figure 2.16. Interpretation of paleoredox environments in terms of the relative abundances of FeHR/FeT and FePy/FeHR. Triangles represent nearshore samples (supratidal to intertidal), square symbols show intertidal to subtidal facies, and circles indicate subtidal to offshore.

contents, which could explain the high productivity as P is considered to be the limiting nutrient for primary productivity (Reinhard et al., 2017; Van Cappellen and Ingall, 1996). Development of euxinia is often linked to increases in primary productivity because high fluxes of organic matter can lead to the reduction of Fe^{3+} which, when coupled with H_2S generation by bacterial sulfate reduction, can result in the precipitation of iron sulfides (Johnston et al., 2010). In any case, euxinia was transient, and deep waters returned to anoxic and ferruginous as indicated by the consistently

elevated Fe_{HR}/Fe_T and low Fe_{Py}/Fe_{HR} values in the Barney Creek Formation, one of the only other units in this study that records deposition at or below the storm wave base.

2.4.2. Local Controls on Iron Enrichment

Whereas both new data presented here and previously published data are consistent with oxygenated surface waters and mainly anoxic and ferruginous deep waters, in some cases shallow water facies plot in anoxic space in the traditional interpretive framework of iron speciation data (Figure 2.16), while sediments deposited in subtidal to offshore environments plot as oxic. While conventional interpretations based on iron speciation data alone may be correct in some cases, it should be noted that both sedimentation rate and sediment source can exert an important role in the chemical composition and associated redox signatures of sediments.

Overall, the sediment source of the Greater McArthur Basin was relatively unweathered as indicated by the relatively low CIA values calculated for all eight drillcores (Figure 2.15). Elevated values above 70 are noted in drillcores with increases in siliciclastic content and a tendency towards oxic values. While increased chemical weathering is known to provide additional reactive iron to the highly reactive iron pool, our result likely indicate robust oxygenation of the deep water, which highlights the need for a more in depth study on the relationships between source rock weathering material, detrital iron supply, and iron speciation data in nearshore marine sedimentary rocks in the Proterozoic.

An apparent temporal evolution from anoxic deep waters to oxic shallow waters is observed in the data set whereby older drillcores show a more obvious division between oxic shallow waters and anoxic deep waters while younger strata (particularly the Roper Group as well as the Bullita and Tijnuna Groups) display increased oxic values in deep water settings (Figures 2.7 and 2.10 respectively). Based on the increased CIA also noted in these drillcores, it is likely that the Greater McArthur Basin did not see a temporal evolution in oceanic redox state but rather a change to a more weathered source or an increase in sedimentation rates. Anomalously low Fe_T/Al as well as the decoupling of iron and aluminum (Figure 2.12B) seem to support this interpretation, although original lithology could play a role as well. For example, mafic lithologies would be expected to have relatively high Fe_T/Al compared to felsic lithologies because they are richer in iron and have lower Al contents. Consequently, Fe_T/Al of the source region may vary by as much as a factor of

three (Wedepohl, 1995), and such variability could be magnified by winnowing and sorting during sediment transport. By contrast, it is suggested the middle Proterozoic was prone to fluctuations in redox state due to overall low concentrations of O_2 , Fe^{2+} , and sulfate, leading to a weak redox buffer which could be consistent with the results of this study (Planavsky et al., 2018). A more focused study, applying Nd isotopes, for example, to track provenance lithology (Cox et al., 2016) would be required to determine the true nature of low FeT/Al values which have also been measured in some younger Neoproterozoic basins (Sahoo et al., 2012; Sperling et al., 2013).

Some nearshore samples displaying anoxic characteristics tend to show elevated proportions of Fe-oxides in the highly reactive iron pool (Appendix A1 through A8) indicative of active nearshore trapping of oxides as has been observed in modern settings (Raiswell, 2011; Sperling et al., 2013). Such is most likely the case with the variability noted in the upper McDermott Formation and middle Tawallah Group (Appendix A1 and A2).

Anoxic samples that do not show an elevated fraction of iron-oxides could represent the development of a lagoonal setting in which organic matter is able to accumulate and oxygen is depleted. This is most likely true in the Birrindudu Basin where the Limbunya Group records enrichments up to 0.48 wt. % TOC compared to an otherwise TOC depleted sample subset (Appendix A6). The McArthur Basin however, rarely shows notable TOC enrichments where shallow water anoxia is concerned. It is possible instead that transient fluctuations in water depth caused episodic increases in the degree of anoxia in the water column. Such variations highlight the importance of constraining nearshore environments and the factors that can affect their overall chemistry from primary productivity to the supply of iron from the continents.

2.4.3. Total Organic Carbon Content and Fossil Preservation

High TOC values reflect a combination of high primary productivity and efficient burial of organic carbon (versus efficient remineralization). These two factors are commonly linked through a positive feedback since high productivity leads to oxygen depletion, which in turns favours organic carbon preservation, as happens in modern oxygen minimum zones on upwelling continental margins such as offshore Peru. High TOC is therefore typically linked to anoxic marine environments. Counter-intuitively, these same sediments, though organic-rich, are commonly poor settings for preserving microfossils. Although the reason for this negative association between TOC and microfossil oc-

currence is uncertain (Woltz et al., 2021), it sufficiently well established for Proterozoic rocks that high TOC samples are commonly avoided in microfossil studies. As such, the low overall TOC contents documented here may represent another inherent bias in the sampling method whereby samples with medium TOC were targeted under the assumption they were more likely to contain and preserve a greater number of fossils (Woltz et al., 2021).

Anoxic samples measured here show an elevated TOC content (ave = 0.64 wt. %; n = 54) as do samples likely reflecting euxinia in the Tawallah Group, but these values are low in comparison to many samples studied in focused redox studies (Algeo and Maynard, 2004). While many of the samples used in this study are known to contain eukaryotic microfossils, it is possible the fossils themselves are more readily preserved in oxic samples regardless of where they were living in the water column. In future studies, a greater number of high TOC samples should be collected regardless of their potential for fossil preservation in order to present a more complete picture of redox conditions and organic carbon preservation.

2.5. Conclusions

The main goal of this study comprises integrating multiple data sets including iron speciation, total organic carbon, and major and trace element geochemistry as a means of reconstructing redox conditions within different paleoenvironmental settings in a long-lived sedimentary basin known to preserve early eukaryotic microfossils. Our results largely corroborate previous redox studies of the Greater McArthur Basin (Cox et al., 2016; Planavsky et al., 2011; Shen et al., 2002), but also provide a more complete and nuanced picture of the redox structure by sampling more lithologies than are typically targeted in paleoredox investigations. The middle Proterozoic was a previously relatively undocumented period of marine evolution with earlier work at best providing speculations into redox conditions based on minimal data from limited lithologies and therefore produced conflicting models (Sperling et al., 2015).

The Greater McArthur Basin was superficially oxic and anoxic at depth but experience a transient episode of euxinia, probably driven by high productivity, itself sustained by high P availability and efficient nutrient recycling. This appears to show that euxinia was much less prevalent in the middle Proterozoic than previously thought (Shen et al., 2002). Another result emerging from the

chemical index of alteration is the trend towards increasing degrees of weathering of the source material up-section. These findings are consistent with the evolving view of the Proterozoic ocean being redox stratified (Lyons et al., 2014), sulphate-poor (Planavsky et al., 2011), and deficient in phosphorus (Reinhard et al., 2017) and with northern Australia being generally tectonically stable in the early Mesoproterozoic.

The samples used in this study are known to contain some of the oldest eukaryotic microfossils (Javaux and Lepot, 2018; Javaux, 2007; Javaux and Knoll, 2017; Porter, 2020), and the results of this study can be used to provide a redox dimension to the environments these early eukaryotes inhabited whereby microbial metabolic processes are dependent on their surrounding environment. The early part of the middle Proterozoic marks an evolutionary milestone in which eukaryotes definitively inhabited oxic settings, perhaps indicating that they had already acquired mitochondria and the capacity for sterol biosynthesis (Porter, 2020). Therefore, notwithstanding preservational biases, this study, combined with radiometric ages on strata of the McArthur basin, provide a time constraint for the acquisition of these key traits that can be applied to other globally correlated sedimentary basins.

Future studies on these strata should aim to elucidate the association of fossils in anoxic environments, as well as explore trace metal enrichments, for example of Mo, U, Cr, and Co, as a means to further investigate local versus global influences on redox conditions. Because there are lithological and chemical biases present with respect to fossil preservation, expanding redox datasets throughout the Paleo- and early Mesoproterozoic with the intention to further understand the microfossils preserved therein, will inevitably elucidate the evolutionary trajectory of multicellular life and the oxygenation of the atmosphere.

Bibliography

- S. Abbott and I. Sweet. Tectonic control on third-order sequences in a siliciclastic ramp-style basin: An example from the roper superbasin (mesoproterozoic), northern australia. *Australian Journal of Earth Sciences*, 47(3):637–657, 2000.
- M. Ahmad, J. Dunster, and T. Munson. *Ahmad M, Dunster JN and Munson TJ, 2013. Chapter 15: McArthur Basin: in Ahmad M and Munson TJ (compilers). 'Geology and mineral resources of the Northern Territory'. Northern Territory Geological Survey, Special Publication 5., pages 15:1–15:72.* Northern Territory Geological Survey, 06 2013. ISBN 978-0-7245-7257-1.
- T. J. Algeo and J. B. Maynard. Trace-element behavior and redox facies in core shales of upper pennsylvanian kansas-type cyclothems. *Chemical geology*, 206(3-4):289–318, 2004.
- A. D. Anbar and A. H. Knoll. Proterozoic ocean chemistry and evolution: a bioinorganic bridge? *science*, 297(5584):1137–1142, 2002.
- J. L. Banner and G. N. Hanson. Calculation of simultaneous isotopic and trace element variations during water-rock interaction with applications to carbonate diagenesis. *Geochimica et Cosmochimica Acta*, 54(11):3123–3137, 1990.
- H. Bao, J. Lyons, and C. Zhou. Triple oxygen isotope evidence for elevated co2 levels after a neoproterozoic glaciation. *Nature*, 453(7194):504–506, 2008.
- J. K. Bartley and L. C. Kah. Marine carbon reservoir, corg-ccarb coupling, and the evolution of the proterozoic carbon cycle. *Geology*, 32(2):129–132, 2004.
- P. Beier, A. Cutovinos, and J. Dunster. Detailed wellsite logs for 99VRNTGSDD1 and 99VRNTGSDD2, Victoria Basin, Northern Territory, 2002a.
- P. Beier, J. Dunster, A. Cutovinos, and B. Pietsch. Victoria River Downs, northern territory (second edition), 1:250 000 geological map series explanatory notes, se 52-04., 2002b.
- P. Beier, J. Dunster, A. Cutovinos, and B. Pietsch. Delamere, Northern Territory (second edition), 1:250 000 geological map series explanatory notes, sd 52-16., 2002c.
- A. Bekker, C. Holmden, N. Beukes, F. Kenig, B. Eglinton, and W. Patterson. Fractionation between inorganic and organic carbon during the lomagundi (2.22–2.1 ga) carbon isotope excursion. *Earth and Planetary Science Letters*, 271(1-4):278–291, 2008.
- A. Bekker, J. F. Slack, N. Planavsky, B. Krapez, A. Hofmann, K. O. Konhauser, and O. J. Rouxel. Iron formation: the sedimentary product of a complex interplay among mantle, tectonic, oceanic, and biospheric processes. *Economic Geology*, 105(3):467–508, 2010.

- A. Bekker, B. Krapež, S. G. Müller, and J. A. Karhu. A short-term, post-lomagundi positive $\delta^{13}\text{C}$ isotope excursion at c. 2.03 ga recorded by the woolly dolomite, western australia. *Journal of the Geological Society*, 173(4):689–700, 2016.
- T. Blakie and M. Kunzmann. Geophysical interpretation and tectonic synthesis of the Proterozoic southern McArthur Basin, northern Australia. *Precambrian Research*, 343:105728, 2020.
- M. Brasier and J. Lindsay. A billion years of environmental stability and the emergence of eukaryotes: New data from northern australia. *Geology*, 26(6):555–558, 1998.
- J. J. Brocks. The transition from a cyanobacterial to algal world and the emergence of animals. *Emerging Topics in Life Sciences*, 2(2):181–190, 2018.
- J. J. Brocks, G. A. Logan, R. Buick, and R. E. Summons. Archean molecular fossils and the early rise of eukaryotes. *science*, 285(5430):1033–1036, 1999.
- J. J. Brocks, G. D. Love, R. E. Summons, A. H. Knoll, G. A. Logan, and S. A. Bowden. Biomarker evidence for green and purple sulphur bacteria in a stratified palaeoproterozoic sea. *Nature*, 437(7060):866–870, 2005.
- J. J. Brocks, A. J. Jarrett, E. Sirantoine, C. Hallmann, Y. Hoshino, and T. Liyanage. The rise of algae in cryogenian oceans and the emergence of animals. *Nature*, 548(7669):578–581, 2017.
- R. Buick, D. J. Des Marais, and A. H. Knoll. Stable isotopic compositions of carbonates from the mesoproterozoic bangemall group, northwestern australia. *Chemical Geology*, 123(1-4):153–171, 1995.
- S. W. Bull and J. R. Rogers. Recognition and significance of an early compressional deformation event in the tawallah group, mcarthur basin, nt. In *MIC'96: New developments in metallogenic research*, volume 55, pages 28–32, 1996.
- N. J. Butterfield. *Bangiomorpha pubescens* n. gen., n. sp.: implications for the evolution of sex, multicellularity, and the mesoproterozoic/neoproterozoic radiation of eukaryotes. *Paleobiology*, 26(3):386–404, 2000.
- N. J. Butterfield. Early evolution of the eukaryota. *Palaeontology*, 58(1):5–17, 2015.
- D. E. Canfield. A new model for proterozoic ocean chemistry. *Nature*, 396(6710):450–453, 1998.
- D. E. Canfield. The early history of atmospheric oxygen: homage to robert m. garrels. *Annu. Rev. Earth Planet. Sci.*, 33:1–36, 2005.
- D. E. Canfield, R. Raiswell, J. T. Westrich, C. M. Reaves, and R. A. Berner. The use of chromium reduction in the analysis of reduced inorganic sulfur in sediments and shales. *Chemical geology*, 54(1-2):149–155, 1986.
- D. E. Canfield, S. W. Poulton, A. H. Knoll, G. M. Narbonne, G. Ross, T. Goldberg, and H. Strauss. Ferruginous conditions dominated later neoproterozoic deep-water chemistry. *Science*, 321(5891):949–952, 2008.
- C. Carson. The victoria and birrindudu basins: a u-pb shrimp study and review of resource potential, 2010.
- O. Cartapanis, D. Bianchi, S. L. Jaccard, and E. D. Galbraith. Global pulses of organic carbon burial in deep-sea sediments during glacial maxima. *Nature communications*, 7(1):1–7, 2016.
- P. A. Cawood and R. Korsch. Assembling australia: Proterozoic building of a continent. *Precambrian Research*, 166(1-4):1–35, 2008.
- P. A. Cawood and S. A. Pisarevsky. Laurentia-baltica-amazonia relations during rodinia assembly. *Precambrian Research*, 292:386–397, 2017.

- M. Clarkson, S. Poulton, R. Guilbaud, and R. Wood. Assessing the utility of fe/al and fe-speciation to record water column redox conditions in carbonate-rich sediments. *Chemical Geology*, 382:111–122, 2014.
- T. B. Coplen. Normalization of oxygen and hydrogen isotope data. *Chemical Geology: Isotope Geoscience Section*, 72(4):293–297, 1988.
- G. M. Cox, A. Jarrett, D. Edwards, P. W. Crockford, G. P. Halverson, A. S. Collins, A. Poirier, and Z.-X. Li. Basin redox and primary productivity within the mesoproterozoic roper seaway. *Chemical Geology*, 440:101–114, 2016.
- H. Craig. Isotopic standards for carbon and oxygen and correction factors for mass-spectrometric analysis of carbon dioxide. *Geochimica et cosmochimica acta*, 12(1-2):133–149, 1957.
- I. Crick, C. Boreham, A. Cook, and T. Powell. Petroleum geology and geochemistry of middle proterozoic mcarthur basin, northern australia ii: Assessment of source rock potential. *AAPG bulletin*, 72(12):1495–1514, 1988.
- P. W. Crockford, J. A. Hayles, H. Bao, N. J. Planavsky, A. Bekker, P. W. Fralick, G. P. Halverson, T. H. Bui, Y. Peng, and B. A. Wing. Triple oxygen isotope evidence for limited mid-proterozoic primary productivity. *Nature*, 559(7715):613–616, 2018.
- P. W. Crockford, M. Kunzmann, A. Bekker, J. Hayles, H. Bao, G. P. Halverson, Y. Peng, T. H. Bui, G. M. Cox, T. M. Gibson, et al. Claypool continued: Extending the isotopic record of sedimentary sulfate. *Chemical Geology*, 513:200–225, 2019.
- V. M. Cumming, S. W. Poulton, A. D. Rooney, and D. Selby. Anoxia in the terrestrial environment during the late mesoproterozoic. *Geology*, 41(5):583–586, 2013.
- A. Cutovinos, P. Beier, P. Kruse, S. Abbott, J. Dunster, and R. Brescianini. Limbunya, northern territory (second edition), 1:250 000 geological map series explanatory notes, se 52-07., 2002.
- D. J. D. des Marais, H. Strauss, R. E. Summons, and J. Hayes. Carbon isotope evidence for the stepwise oxidation of the proterozoic environment. *Nature*, 359(6396):605–609, 1992.
- J. Ding, S. Zhang, H. Zhao, H. Xian, H. Li, T. Yang, H. Wu, and W. Wang. A combined geochronological and paleomagnetic study on 1220 ma mafic dikes in the north china craton and the implications for the breakup of nuna and assembly of rodinia. *American Journal of Science*, 320(2):125–149, 2020.
- P. Dunn. Urapunga, northern territory . 1: 250 000 geological map series explanatory notes, sd 53-10, 1963.
- J. Dunster and A. Cutovinos. Drillhole completion report - 99VRNTGSDD1 and 99VRNTGSDD2, Victoria River Downs, Northern Territory, 2002.
- J. Dunster, P. Beier, J. Burgess, and A. Cutovinos. Auvergne, northern territory (second edition), 1:250 000 geological map series explanatory notes, se 52-07., 2000.
- T. M. Embley and W. Martin. Eukaryotic evolution, changes and challenges. *Nature*, 440(7084):623–630, 2006.
- R. Ernst, M. Wingate, K. Buchan, and Z.-X. Li. Global record of 1600–700 ma large igneous provinces (lips): implications for the reconstruction of the proposed nuna (columbia) and rodinia supercontinents. *Precambrian Research*, 160(1-2):159–178, 2008.
- D. H. Erwin, M. Laflamme, S. M. Tweedt, E. A. Sperling, D. Pisani, and K. J. Peterson. The cambrian conundrum: early divergence and later ecological success in the early history of animals. *science*, 334(6059):1091–1097, 2011.
- D. A. Evans and R. N. Mitchell. Assembly and breakup of the core of paleoproterozoic–mesoproterozoic supercontinent nuna. *Geology*, 39(5):443–446, 2011.

- C. Fanning. Ion microprobe u–pb zircon dating of a tuffaceous horizon within the kunja siltstone, victoria river basin, northern territory. report for pacific oil and gas pty ltd, 1991.
- J. Farquhar, H. Bao, and M. Thiemens. Atmospheric influence of earth’s earliest sulfur cycle. *Science*, 289(5480):756–758, 2000.
- R. P. Fiorella and N. D. Sheldon. Equable end mesoproterozoic climate in the absence of high co₂. *Geology*, 45(3):231–234, 2017.
- K. L. French, C. Hallmann, J. M. Hope, P. L. Schoon, J. A. Zumberge, Y. Hoshino, C. A. Peters, S. C. George, G. D. Love, J. J. Brocks, et al. Reappraisal of hydrocarbon biomarkers in archean rocks. *Proceedings of the National Academy of Sciences*, 112(19):5915–5920, 2015.
- G. Gibson and D. Champion. Antipodean fugitive terranes in southern laurentia: How proterozoic australia built the american west. *Lithosphere*, 11(4):551–559, 2019.
- G. Gibson, D. Champion, I. Withnall, N. Neumann, and L. Hutton. Assembly and breakup of the nuna supercontinent: Geodynamic constraints from 1800 to 1600 ma sedimentary basins and basaltic magmatism in northern australia. *Precambrian Research*, 313:148–169, 2018a.
- T. M. Gibson, P. M. Shih, V. M. Cumming, W. W. Fischer, P. W. Crockford, M. S. Hodgskiss, S. Wörndle, R. A. Creaser, R. H. Rainbird, T. M. Skulski, et al. Precise age of bangiomorpha pubescens dates the origin of eukaryotic photosynthesis. *Geology*, 46(2):135–138, 2018b.
- G. J. Gilleaudeau and L. C. Kah. Heterogeneous redox conditions and a shallow chemocline in the mesoproterozoic ocean: Evidence from carbon–sulfur–iron relationships. *Precambrian Research*, 257:94–108, 2015.
- G. J. Gilleaudeau, R. Frei, A. Kaufman, L. Kah, K. Azmy, J. Bartley, P. Chernyavskiy, and A. H. Knoll. Oxygenation of the mid-proterozoic atmosphere: clues from chromium isotopes in carbonates. *Geochemical Perspectives Letters*, 2016.
- A. P. Gumsley, K. R. Chamberlain, W. Bleeker, U. Söderlund, M. O. de Kock, E. R. Larsson, and A. Bekker. Timing and tempo of the great oxidation event. *Proceedings of the National Academy of Sciences*, 114(8):1811–1816, 2017.
- H. Guo, Y. Du, L. C. Kah, J. Huang, C. Hu, H. Huang, and W. Yu. Isotopic composition of organic and inorganic carbon from the mesoproterozoic jixian group, north china: Implications for biological and oceanic evolution. *Precambrian Research*, 224:169–183, 2013.
- J. M. Hayes, H. Strauss, and A. J. Kaufman. The abundance of ¹³c in marine organic matter and isotopic fractionation in the global biogeochemical cycle of carbon during the past 800 ma. *Chemical Geology*, 161(1-3):103–125, 1999.
- M. S. Hodgskiss and E. A. Sperling. A prolonged, two-step oxygenation of earth’s early atmosphere: Support from confidence intervals. *Geology*, 50(2):158–162, 2022.
- M. S. Hodgskiss, P. W. Crockford, Y. Peng, B. A. Wing, and T. J. Horner. A productivity collapse to end earth’s great oxidation. *Proceedings of the National Academy of Sciences*, 116(35):17207–17212, 2019a.
- M. S. Hodgskiss, O. M. Dagnaud, J. L. Frost, G. P. Halverson, M. D. Schmitz, N. L. Swanson-Hysell, and E. A. Sperling. New insights on the orosirian carbon cycle, early cyanobacteria, and the assembly of laurentia from the paleoproterozoic belcher group. *Earth and Planetary Science Letters*, 520:141–152, 2019b.
- P. Hoffman. Tectonic genealogy of north america. *Earth structure: An introduction to structural geology and tectonics.*, pages 459–464, 1997.
- H. D. Holland. Volcanic gases, black smokers, and the great oxidation event. *Geochimica et Cosmochimica Acta*, 66(21):3811–3826, 2002.

- Y. Hoshino and E. A. Gaucher. Evolution of bacterial steroid biosynthesis and its impact on eukaryogenesis. *Proceedings of the National Academy of Sciences*, 118(25), 2021.
- R. Hotinski, L. Kump, and M. A. Arthur. The effectiveness of the paleoproterozoic biological pump: A $\delta^{13}\text{C}$ gradient from platform carbonates of the pethei group (great slave lake supergroup, nwt). *Geological Society of America Bulletin*, 116(5-6):539–554, 2004.
- G. Hou, M. Santosh, X. Qian, G. S. Lister, and J. Li. Configuration of the late paleoproterozoic supercontinent columbia: insights from radiating mafic dyke swarms. *Gondwana Research*, 14(3):395–409, 2008.
- M. Jackson and R. Raiswell. Sedimentology and carbon-sulphur geochemistry of the velkerri formation, a mid-proterozoic potential oil source in northern australia. *Precambrian Research*, 54(1):81–108, 1991.
- M. Jackson, T. Powell, R. Summons, and I. Sweet. Hydrocarbon shows and petroleum source rocks in sediments as old as 1.7×10^9 years. *Nature*, 322(6081):727–729, 1986.
- M. Jackson, M. D. Muir, and K. A. Plumb. *Geology of the southern McArthur basin, Northern Territory*, volume 223. Australian Government Pub. Service, 1987.
- M. Jackson, I. Sweet, R. Page, and B. Bradshaw. The south nicholson and roper groups: evidence for the early mesoproterozoic roper superbasin. *Integrated Basin Analysis of the Isa Superbasin using Seismic, Well-log, and Geopotential Data: An Evaluation of the Economic Potential of the Northern Lawn Hill Platform: Canberra, Australia, Australian Geological Survey Organisation Record*, 19, 1999.
- M. Jackson, D. Scott, and D. Rawlings. Stratigraphic framework for the leichhardt and calvert superbasins: Review and correlations of the pre-1700 ma successions between mt isa and mcarthur river. *Australian Journal of Earth Sciences*, 47(3):381–403, 2000.
- E. J. Javaux. The early eukaryotic fossil record. *Eukaryotic membranes and cytoskeleton*, pages 1–19, 2007.
- E. J. Javaux and A. H. Knoll. Micropaleontology of the lower mesoproterozoic roper group, australia, and implications for early eukaryotic evolution. *Journal of Paleontology*, 91(2):199–229, 2017.
- E. J. Javaux and K. Lepot. The paleoproterozoic fossil record: implications for the evolution of the biosphere during earth’s middle-age. *Earth-Science Reviews*, 176:68–86, 2018.
- E. J. Javaux, A. H. Knoll, and M. R. Walter. Morphological and ecological complexity in early eukaryotic ecosystems. *Nature*, 412(6842):66–69, 2001.
- E. J. Javaux, A. H. Knoll, and M. R. Walter. Tem evidence for eukaryotic diversity in mid-proterozoic oceans. *Geobiology*, 2(3):121–132, 2004.
- D. T. Johnston, J. Farquhar, R. E. Summons, Y. Shen, A. J. Kaufman, A. L. Masterson, and D. E. Canfield. Sulfur isotope biogeochemistry of the proterozoic mcarthur basin. *Geochimica et Cosmochimica Acta*, 72(17):4278–4290, 2008.
- D. T. Johnston, S. W. Poulton, C. Dehler, S. Porter, J. Husson, D. E. Canfield, and A. H. Knoll. An emerging picture of neoproterozoic ocean chemistry: Insights from the chuar group, grand canyon, usa. *Earth and Planetary Science Letters*, 290(1-2):64–73, 2010.
- L. C. Kah and J. K. Bartley. Protracted oxygenation of the proterozoic biosphere. *International Geology Review*, 53(11-12):1424–1442, 2011.
- L. C. Kah, T. W. Lyons, and J. T. Chesley. Geochemistry of a 1.2 ga carbonate-evaporite succession, northern baffin and bylot islands: implications for mesoproterozoic marine evolution. *Precambrian Research*, 111(1-4):203–234, 2001.
- L. C. Kah, T. W. Lyons, and T. D. Frank. Low marine sulphate and protracted oxygenation of the proterozoic biosphere. *Nature*, 431(7010):834–838, 2004.

- J. A. Karhu and H. D. Holland. Carbon isotopes and the rise of atmospheric oxygen. *Geology*, 24(10):867–870, 1996.
- B. Kendall, R. A. Creaser, G. W. Gordon, and A. D. Anbar. Re–os and mo isotope systematics of black shales from the middle proterozoic velkerri and wollogorang formations, mcarthur basin, northern australia. *Geochimica et Cosmochimica Acta*, 73(9):2534–2558, 2009.
- U. Kirscher, R. N. Mitchell, Y. Liu, A. R. Nordsvan, G. M. Cox, S. A. Pisarevsky, C. Wang, L. Wu, J. B. Murphy, and Z.-X. Li. Paleomagnetic constraints on the duration of the australia-laurentia connection in the core of the nuna supercontinent. *Geology*, 49(2):174–179, 2021.
- A. H. Knoll. Paleobiological perspectives on early eukaryotic evolution. *Cold Spring Harbor Perspectives in Biology*, 6(1):a016121, 2014.
- R. E. Kopp, J. L. Kirschvink, I. A. Hilburn, and C. Z. Nash. The paleoproterozoic snowball earth: a climate disaster triggered by the evolution of oxygenic photosynthesis. *Proceedings of the National Academy of Sciences*, 102(32):11131–11136, 2005.
- B. Kronberg, H. Nesbitt, and W. Lam. Upper pleistocene amazon deep-sea fan muds reflect intense chemical weathering of their mountainous source lands. *Chemical Geology*, 54(3-4):283–294, 1986.
- M. Kunzmann, G. P. Halverson, C. Scott, W. G. Minarik, and B. A. Wing. Geochemistry of neoproterozoic black shales from svalbard: Implications for oceanic redox conditions spanning cryogenian glaciations. *Chemical Geology*, 417:383–393, 2015.
- M. Kunzmann, S. Schmid, T. N. Blaikie, and G. P. Halverson. Facies analysis, sequence stratigraphy, and carbon isotope chemostratigraphy of a classic zn-pb host succession: The proterozoic middle mcarthur group, mcarthur basin, australia. *Ore Geology Reviews*, 106:150–175, 2019.
- M. Kunzmann, V. Crombez, O. Catuneanu, T. N. Blaikie, G. Barth, and A. S. Collins. Sequence stratigraphy of the ca. 1730 ma wollogorang formation, mcarthur basin, australia. *Marine and Petroleum Geology*, 116:104297, 2020.
- T. A. Laakso and D. P. Schrag. A small marine biosphere in the proterozoic. *Geobiology*, 17(2):161–171, 2019.
- D. Lamb, S. Awramik, D. Chapman, and S. Zhu. Evidence for eukaryotic diversification in the 1800 million-year-old changzhougou formation, north china. *Precambrian Research*, 173(1-4):93–104, 2009.
- J. Lee Rodgers and W. A. Nicewander. Thirteen ways to look at the correlation coefficient. *The American Statistician*, 42(1):59–66, 1988.
- H. Li, S. Lu, W. Su, Z. Xiang, H. Zhou, and Y. Zhang. Recent advances in the study of the mesoproterozoic geochronology in the north china craton. *Journal of Asian Earth Sciences*, 72:216–227, 2013.
- J. F. Lindsay and M. Brasier. A carbon isotope reference curve for ca. 1700–1575 ma, mcarthur and mount isa basins, northern australia. *Precambrian Research*, 99(3-4):271–308, 2000.
- J. F. Lindsay and M. D. Brasier. Did global tectonics drive early biosphere evolution? carbon isotope record from 2.6 to 1.9 ga carbonates of western australian basins. *Precambrian Research*, 114(1-2):1–34, 2002.
- G. D. Love and J. A. Zumberge. *Emerging patterns in proterozoic lipid biomarker records*. Cambridge University Press, 2021.
- T. W. Lyons and S. Severmann. A critical look at iron paleoredox proxies: New insights from modern euxinic marine basins. *Geochimica et Cosmochimica Acta*, 70(23):5698–5722, 2006.
- T. W. Lyons, A. D. Anbar, S. Severmann, C. Scott, and B. C. Gill. Tracking euxinia in the ancient ocean: a multiproxy perspective and proterozoic case study. *Annual Review of Earth and Planetary Sciences*, 37:507–534, 2009a.

- T. W. Lyons, C. Reinhard, and C. Scott. Redox redux. *Geobiology*, 7(5):489–494, 2009b.
- T. W. Lyons, C. T. Reinhard, and N. J. Planavsky. The rise of oxygen in earth’s early ocean and atmosphere. *Nature*, 506(7488):307–315, 2014.
- T. W. Lyons, C. W. Diamond, N. J. Planavsky, C. T. Reinhard, and C. Li. Oxygenation, life, and the planetary system during earth’s middle history: An overview. *Astrobiology*, 21(8):906–923, 2021.
- P. McGoldrick, P. Winefield, S. Bull, D. Selley, and R. Scott. Sequences, synsedimentary structures, and sub-basins: the where and when of sedex zinc systems in the southern mcarthur basin, australia. *Soc. Econ. Geol. Spec. Publ*, 15:1–23, 2010.
- J. G. Meert. What’s in a name? the columbia (paleopangaea/nuna) supercontinent. *Gondwana Research*, 21(4):987–993, 2012.
- T. Munson. Sedimentary characterisation of the wilton package, greater mcarthur basin, northern territory. northern territory geological survey, record 2016-003. *Northern Territory Geological Survey, Record*, 2016-003, 12 2016.
- T. Munson, S. Denyszyn, J. Simmons, and M. Kunzmann. A 1642 ma age for the fraynes formation, birrindudu basin, confirms correlation with the economically significant barney creek formation, mcarthur basin, northern territory. *Australian Journal of Earth Sciences*, 67(3):321–330, 2020.
- H. Nesbitt and G. Young. Early proterozoic climates and plate motions inferred from major element chemistry of lutites. *nature*, 299(5885):715–717, 1982.
- R. Page, M. Jackson, and A. Krassay. Constraining sequence stratigraphy in north australian basins: Shrimp u–pb zircon geochronology between mt isa and mcarthur river. *Australian Journal of Earth Sciences*, 47(3):431–459, 2000.
- S. J. Pehrsson, B. M. Eglington, D. A. Evans, D. Huston, and S. M. Reddy. Metallogeny and its link to orogenic style during the nuna supercontinent cycle. *Geological Society, London, Special Publications*, 424(1):83–94, 2016.
- N. J. Planavsky, P. McGoldrick, C. T. Scott, C. Li, C. T. Reinhard, A. E. Kelly, X. Chu, A. Bekker, G. D. Love, and T. W. Lyons. Widespread iron-rich conditions in the mid-proterozoic ocean. *Nature*, 477(7365):448–451, 2011.
- N. J. Planavsky, A. Bekker, A. Hofmann, J. D. Owens, and T. W. Lyons. Sulfur record of rising and falling marine oxygen and sulfate levels during the lomagundi event. *Proceedings of the National Academy of Sciences*, 109(45):18300–18305, 2012.
- N. J. Planavsky, C. T. Reinhard, X. Wang, D. Thomson, P. McGoldrick, R. H. Rainbird, T. Johnson, W. W. Fischer, and T. W. Lyons. Low mid-proterozoic atmospheric oxygen levels and the delayed rise of animals. *science*, 346(6209):635–638, 2014.
- N. J. Planavsky, J. F. Slack, W. F. Cannon, B. O’Connell, T. T. Isson, D. Asael, J. C. Jackson, D. S. Hardisty, T. W. Lyons, and A. Bekker. Evidence for episodic oxygenation in a weakly redox-buffered deep mid-proterozoic ocean. *Chemical Geology*, 483:581–594, 2018.
- K. Plumb and M. Brown. Revised correlations and stratigraphic nomenclature in the proterozoic carbonate complex of the mcarthur group, northern territory. *Geology and Geophysics Bulletin*, 139:103–115, 1973.
- K. Plumb and P. Wellman. Mcarthur basin, northern territory: mapping of deep troughs using gravity and magnetic anomalies. *BMR Journal of Australian Geology & Geophysics*, 10(3):243–251, 1987.
- K. Plumb, M. Ahmad, and A. Wygralak. Mid-proterozoic basins of the north australian craton—regional geology and mineralisation. *Geology of the mineral deposits of Australia and Papua New Guinea*, 1:881–902, 1990.

- S. M. Porter. Insights into eukaryogenesis from the fossil record. *Interface Focus*, 10(4):20190105, 2020.
- S. W. Poulton and D. E. Canfield. Development of a sequential extraction procedure for iron: implications for iron partitioning in continentally derived particulates. *Chemical geology*, 214(3-4):209–221, 2005.
- S. W. Poulton and D. E. Canfield. Ferruginous conditions: a dominant feature of the ocean through earth’s history. *Elements*, 7(2):107–112, 2011.
- S. W. Poulton, P. W. Fralick, and D. E. Canfield. The transition to a sulphidic ocean 1.84 billion years ago. *Nature*, 431(7005):173–177, 2004.
- S. W. Poulton, P. W. Fralick, and D. E. Canfield. Spatial variability in oceanic redox structure 1.8 billion years ago. *Nature Geoscience*, 3(7):486–490, 2010.
- S. W. Poulton, A. Bekker, V. M. Cumming, A. L. Zerkle, D. E. Canfield, and D. T. Johnston. A 200-million-year delay in permanent atmospheric oxygenation. *Nature*, 592(7853):232–236, 2021.
- A. Prave, K. Kirsimäe, A. Lepland, A. Fallick, T. Kreitsmann, Y. E. Deines, A. Romashkin, D. Rychanchik, P. Medvedev, M. Moussavou, et al. The grandest of them all: the lomagundi–jatuli event and earth’s oxygenation. *Journal of the Geological Society*, 179(1), 2022.
- Y. Qu, A. Črne, A. Lepland, and M. Van Zuilen. Methanotrophy in a paleoproterozoic oil field ecosystem, z aonega formation, k arelia, r ussia. *Geobiology*, 10(6):467–478, 2012.
- R. Raiswell. Iron transport from the continents to the open ocean: The aging–rejuvenation cycle. *Elements*, 7(2):101–106, 2011.
- R. Raiswell and D. E. Canfield. Sources of iron for pyrite formation in marine sediments. *American Journal of Science*, 298(3):219–245, 1998.
- B. Rasmussen, A. Bekker, and I. R. Fletcher. Correlation of paleoproterozoic glaciations based on u–pb zircon ages for tuff beds in the transvaal and huronian supergroups. *Earth and Planetary Science Letters*, 382:173–180, 2013.
- D. Rawlings. Stratigraphic resolution of a multiphase intracratonic basin system: the mcarthur basin, northern australia. *Australian Journal of Earth Sciences*, 46(5):703–723, 1999.
- D. Rawlings, R. Korsch, B. Goleby, G. Gibson, D. Johnstone, and M. Barlow. The 2002 southern mcarthur basin seismic reflection survey. *Geoscience Australia, Record*, 17:78, 2004.
- C. T. Reinhard, N. J. Planavsky, L. J. Robbins, C. A. Partin, B. C. Gill, S. V. Lalonde, A. Bekker, K. O. Konhauser, and T. W. Lyons. Proterozoic ocean redox and biogeochemical stasis. *Proceedings of the National Academy of Sciences*, 110(14):5357–5362, 2013.
- C. T. Reinhard, N. J. Planavsky, B. C. Gill, K. Ozaki, L. J. Robbins, T. W. Lyons, W. W. Fischer, C. Wang, D. B. Cole, and K. O. Konhauser. Evolution of the global phosphorus cycle. *Nature*, 541(7637):386–389, 2017.
- J. Rogers. *Geology and tectonic setting of the Tawallah Group, southern McArthur basin, Northern Territory*. PhD thesis, University of Tasmania,, 1996.
- D. J. Ross and R. M. Bustin. Investigating the use of sedimentary geochemical proxies for paleoenvironment interpretation of thermally mature organic-rich strata: Examples from the devonian–mississippian shales, western canadian sedimentary basin. *Chemical Geology*, 260(1-2):1–19, 2009.
- S. K. Sahoo, N. J. Planavsky, B. Kendall, X. Wang, X. Shi, C. Scott, A. D. Anbar, T. W. Lyons, and G. Jiang. Ocean oxygenation in the wake of the marinoan glaciation. *Nature*, 489(7417):546–549, 2012.

- M. Schidlowski, R. Eichmann, and C. E. Junge. Precambrian sedimentary carbonates: carbon and oxygen isotope geochemistry and implications for the terrestrial oxygen budget. *Precambrian Research*, 2(1):1–69, 1975.
- M. Schidlowski, R. Eichmann, and C. E. Junge. Carbon isotope geochemistry of the precambrian lomagundi carbonate province, rhodesia. *Geochimica et Cosmochimica Acta*, 40(4):449–455, 1976.
- S. Schmid. Sedimentological review of the barney creek formation in drillholes lv09001, bj2, mca5, mcarthur basin, 2016.
- C. Scott, T. Lyons, A. Bekker, Y.-a. Shen, S. Poulton, X.-l. Chu, and A. Anbar. Tracing the stepwise oxygenation of the proterozoic ocean. *Nature*, 452(7186):456–459, 2008.
- C. Scott, B. A. Wing, A. Bekker, N. J. Planavsky, P. Medvedev, S. M. Bates, M. Yun, and T. W. Lyons. Pyrite multiple-sulfur isotope evidence for rapid expansion and contraction of the early paleoproterozoic seawater sulfate reservoir. *Earth and Planetary Science Letters*, 389:95–104, 2014.
- D. Scott, D. Rawlings, R. Page, C. Tarlowski, M. Idnurm, M. Jackson, and P. Southgate. Basement framework and geodynamic evolution of the palaeoproterozoic superbasins of north-central australia: an integrated review of geochemical, geochronological and geophysical data. *Australian Journal of Earth Sciences*, 47(3):341–380, 2000.
- Y. Shen, D. E. Canfield, and A. H. Knoll. Middle proterozoic ocean chemistry: evidence from the mcarthur basin, northern australia. *American Journal of Science*, 302(2):81–109, 2002.
- A. Spang, J. H. Saw, S. L. J. rgensen, K. Zaremba-Niedawiedzka, J. Martijn, A. E. Lind, R. van Eijk, C. Schleper, L. Guy, and T. J. G. Ettema. Complex archaea that bridge the gap between prokaryotes and eukaryotes. *Nature*, 521:173–179, 2015.
- E. A. Sperling, G. P. Halverson, A. H. Knoll, F. A. Macdonald, and D. T. Johnston. A basin redox transect at the dawn of animal life. *Earth and Planetary Science Letters*, 371:143–155, 2013.
- E. A. Sperling, C. J. Wolock, A. S. Morgan, B. C. Gill, M. Kunzmann, G. P. Halverson, F. A. Macdonald, A. H. Knoll, and D. T. Johnston. Statistical analysis of iron geochemical data suggests limited late proterozoic oxygenation. *Nature*, 523(7561):451–454, 2015.
- S. C. Spinks, S. Schmid, A. Pagés, and J. Bluett. Evidence for sedex-style mineralization in the 1.7 ga tawallah group, mcarthur basin, australia. *Ore Geology Reviews*, 76:122–139, 2016.
- I. Sweet, J. Mendum, R. Bultitude, and C. Morgan. The geology of the southern victoria river region, northern territory. bureau of mineral resources. *Geology and Geophysics Report*, 167, 1974.
- I. Sweet, T. Powell, et al. Studies on petroleum geology and geochemistry, middle proterozoic, mcarthur basin northern australia i: Petroleum potential. *The APPEA Journal*, 28(1):283–302, 1988.
- N. Tribouvillard, T. J. Algeo, T. Lyons, and A. Riboulleau. Trace metals as paleoredox and paleoproductivity proxies: an update. *Chemical geology*, 232(1-2):12–32, 2006.
- P. Van Cappellen and E. D. Ingall. Redox stabilization of the atmosphere and oceans by phosphorus-limited marine productivity. *Science*, 271(5248):493–496, 1996.
- G. Vinnichenko, A. J. Jarrett, J. M. Hope, and J. J. Brocks. Discovery of the oldest known biomarkers provides evidence for phototrophic bacteria in the 1.73 ga wollogorang formation, australia. *Geobiology*, 18(5):544–559, 2020.
- R. Walker, M. Muir, W. Diver, N. Williams, and N. Wilkins. Evidence of major sulphate evaporite deposits in the proterozoic mcarthur group, northern territory, australia. *Nature*, 265(5594):526–529, 1977.

- B. P. Walpole. *Geology of the Katherine-Darwin region, Northern Territory*. Number 82. Bureau of Mineral Resources, Geology and Geophysics, 1968.
- C. Wang, M. A. Lechte, C. T. Reinhard, D. Asael, D. B. Cole, G. P. Halverson, S. M. Porter, N. Galili, I. Halevy, R. H. Rainbird, et al. Strong evidence for a weakly oxygenated ocean–atmosphere system during the proterozoic. *Proceedings of the National Academy of Sciences*, 119(6), 2022.
- M. R. Warke, T. Di Rocco, A. L. Zerkle, A. Lepland, A. R. Prave, A. P. Martin, Y. Ueno, D. J. Condon, and M. W. Claire. The great oxidation event preceded a paleoproterozoic “snowball earth”. *Proceedings of the National Academy of Sciences*, 117(24):13314–13320, 2020.
- K. Wedepohl. Environmental influences on the chemical composition of shales and clays. *Physics and Chemistry of the Earth*, 8:307–333, 1971.
- K. H. Wedepohl. The composition of the continental crust. *Geochimica et cosmochimica Acta*, 59(7):1217–1232, 1995.
- J. P. Wilson, W. W. Fischer, D. T. Johnston, A. H. Knoll, J. P. Grotzinger, M. R. Walter, N. J. McNaughton, M. Simon, J. Abelson, D. P. Schrag, et al. Geobiology of the late paleoproterozoic duck creek formation, western australia. *Precambrian Research*, 179(1-4):135–149, 2010.
- C. Woltz, S. Porter, H. Agić, C. Dehler, C. Junium, L. Riedman, M. Hodgskiss, S. Wörndle, and G. Halverson. Total organic carbon and the preservation of organic-walled microfossils in precambrian shale. *Geology*, 49(5):556–560, 2021.
- K. Zhang, X. Zhu, R. A. Wood, Y. Shi, Z. Gao, and S. W. Poulton. Oxygenation of the mesoproterozoic ocean and the evolution of complex eukaryotes. *Nature Geoscience*, 11(5):345–350, 2018.
- S. Zhang, Z.-X. Li, D. A. Evans, H. Wu, H. Li, and J. Dong. Pre-rodinia supercontinent nuna shaping up: A global synthesis with new paleomagnetic results from north china. *Earth and Planetary Science Letters*, 353:145–155, 2012.
- S. Zhang, X. Wang, H. Wang, C. J. Bjerrum, E. U. Hammarlund, M. M. Costa, J. N. Connelly, B. Zhang, J. Su, and D. E. Canfield. Sufficient oxygen for animal respiration 1,400 million years ago. *Proceedings of the National Academy of Sciences*, 113(7):1731–1736, 2016.
- J. A. Zumberge, D. Rocher, and G. D. Love. Free and kerogen-bound biomarkers from late tonian sedimentary rocks record abundant eukaryotes in mid-neoproterozoic marine communities. *Geobiology*, 18(3):326–347, 2020.

Appendices

A. Raw Data: Iron Speciation and Total Organic Carbon Content

Sample Depth	% N	% C	FeCarb	FeOx	FeMag	FePy	FeHR	FeT	FePy / FeHR	FeHR / FeT	Interpretation
480.37	0.03	0.04	0.05	0.37	0.04	0.02	0.47	3.71	0.03	0.13	Oxic
484.55	0.02	0.05	0.33	0.14	0.18	Below Det.	0.65	3.36	0.00	0.19	Oxic
487.47	0.02	0.27	0.38	0.10	0.04	0.06	0.57	2.32	0.10	0.25	Equivocal
497	0.02	0.21	0.03	1.48	0.12	0.05	1.68	2.97	0.03	0.57	Ferruginous
502	0.02	0.22	0.35	0.18	0.10	0.41	1.03	2.91	0.40	0.35	Equivocal
507.25	0.02	0.22	0.17	0.11	0.06	0.05	0.40	2.52	0.12	0.16	Oxic
512.86	0.02	0.26	0.23	0.13	0.12	0.04	0.52	3.10	0.07	0.17	Oxic
518.03	0.02	0.34	0.47	0.09	0.08	0.05	0.69	2.08	0.08	0.33	Equivocal
529.28	0.02	0.17	1.23	0.11	0.07	0.04	1.45	2.82	0.03	0.51	Ferruginous
537.04	0.03	0.54	0.16	0.18	0.22	0.05	0.61	3.46	0.09	0.18	Oxic
546.07	0.04	1.68	0.32	0.09	0.14	0.19	0.74	2.06	0.25	0.36	Equivocal
549.07	0.02	0.29	0.45	0.14	0.24	0.13	0.96	3.11	0.14	0.31	Equivocal
559	0.04	1.95	0.33	0.14	0.23	0.01	0.71	3.35	0.02	0.21	Equivocal
567.3	0.04	2.14	0.27	0.16	0.23	0.60	1.27	3.76	0.48	0.34	Equivocal
577	0.04	1.96	0.30	0.13	0.25	0.01	0.69	3.61	0.01	0.19	Oxic
589.42	0.04	2.02	0.39	0.26	0.23	0.07	0.95	3.10	0.07	0.31	Equivocal
592.7	0.02	0.44	0.45	0.18	0.29	0.07	0.99	4.40	0.07	0.22	Equivocal
598.17	0.03	0.80	0.33	0.14	0.22	0.10	0.79	3.57	0.13	0.22	Oxic
610.75	0.03	1.34	0.35	0.14	0.25	0.17	0.91	3.04	0.19	0.30	Equivocal
613.5	0.03	2.88	0.57	0.12	0.21	0.08	0.98	2.92	0.08	0.34	Equivocal
620.55	0.03	0.29	0.35	0.38	0.19	0.59	1.51	4.10	0.39	0.37	Equivocal
621.4	0.02	0.12	0.01	0.00	0.00	0.18	0.20	4.18	0.92	0.05	Oxic
630.8	0.02	0.12	0.30	0.15	0.22	0.02	0.69	3.93	0.03	0.18	Oxic
640.55	0.02	0.22	0.44	0.16	0.19	0.36	1.15	4.06	0.31	0.28	Equivocal
650.24	0.02	0.11	0.26	0.16	0.18	0.08	0.68	3.57	0.12	0.19	Oxic
657.13	0.02	0.22	1.66	0.17	0.05	0.14	2.02	3.89	0.07	0.52	Ferruginous
667.54	0.02	0.29	0.02	1.30	0.14	0.29	1.75	2.27	0.16	0.77	Ferruginous
678.07	0.02	0.29	1.32	0.13	0.04	0.13	1.62	2.92	0.08	0.56	Ferruginous
687.35	0.02	0.20	0.63	0.10	0.05	0.14	0.91	2.12	0.16	0.43	Ferruginous
689.2	0.02	0.19	0.95	0.13	0.06	0.06	1.20	2.88	0.05	0.42	Ferruginous
700.3	0.02	0.27	0.27	0.13	0.13	0.24	0.77	3.13	0.31	0.25	Equivocal

Table A1. Total organic carbon, raw iron speciation data, and calculations recorded in weight % for drill core GSD7 from the McArthur Basin.

Sample Depth	% N	% C	FeCarb	FeMag	FeOx	FePy	FeHR	FeT	FePy / FeHR	FeHR / FeT	Interpretation
8.73	0.02	0.15	1.03	0.26	0.00	0.00	1.30	2.58	0.00	0.50	Ferruginous
9.65	0.02	0.18	1.17	0.08	0.01	0.06	1.31	2.40	0.04	0.55	Ferruginous
17.75	0.02	0.28	1.38	0.19	0.09	0.08	1.74	3.67	0.05	0.47	Ferruginous
25.5	0.02	0.26	1.59	0.07	0.06	0.12	1.83	3.31	0.06	0.55	Ferruginous
32.55	0.03	0.94	0.50	0.11	0.08	0.38	1.06	6.07	0.36	0.18	Oxic
38.6	0.05	3.22	0.50	0.03	0.05	2.73	3.30	4.04	0.83	0.82	Euxinic
41.85	0.04	1.62	0.61	0.19	0.06	1.72	2.57	3.95	0.67	0.65	Ferruginous
54.95	0.08	4.37	0.36	0.15	0.06	1.52	2.09	2.72	0.73	0.77	Ferruginous
65.27	0.02	1.08	0.94	0.03	0.02	0.12	1.11	1.71	0.11	0.65	Ferruginous
73.35	0.02	0.20	0.44	0.10	0.21	0.05	0.80	3.20	0.06	0.25	Equivocal
86.3	0.02	0.10	0.46	0.16	0.18	0.01	0.81	3.43	0.01	0.24	Equivocal
92.32	0.02	0.06	0.41	0.28	0.18	0.01	0.89	3.80	0.02	0.23	Equivocal
96.96	0.02	0.07	0.36	0.63	0.27	Below Det.	1.26	4.53	0.00	0.28	Equivocal
215.52	0.00	0.06	1.92	1.91	0.73	0.00	4.55	7.14	0.00	0.64	Ferruginous
225.05	0.02	0.08	0.26	0.09	0.06	Below Det.	0.41	2.97	0.00	0.14	Oxic
255.85	0.02	0.07	0.05	0.07	0.03	Below Det.	0.15	3.06	0.00	0.05	Oxic
266.7	0.02	0.30	0.17	0.07	0.02	0.29	0.56	2.76	0.52	0.20	Oxic
270.9	0.02	0.10	0.22	0.11	0.08	0.08	0.48	2.78	0.16	0.17	Oxic
279.27			0.27	0.10	0.04	0.30	0.71	3.08	0.43	0.23	Equivocal
281.4	0.02	0.10	0.17	0.09	0.05	Below Det.	0.31	3.15	0.00	0.10	Oxic
289.62	0.02	0.08	0.95	0.35	0.46	0.08	1.84	3.92	0.04	0.47	Ferruginous
295.14	0.02	0.11	0.18	0.26	0.03	0.05	0.51	3.50	0.09	0.14	Oxic
304.49	0.02	0.12	0.94	0.27	0.11	0.35	1.66	3.94	0.21	0.42	Ferruginous
309.7	0.02	0.08	0.23	0.09	0.04	Below Det.	0.35	2.50	0.00	0.14	Oxic
335.47	0.02	0.06	0.49	0.12	0.04	Below Det.	0.65	2.76	0.00	0.24	Equivocal
335.9	0.02	0.09	0.24	0.09	0.02	Below Det.	0.36	2.59	0.00	0.14	Oxic
347.14	0.02	0.06	0.33	0.32	0.05	0.03	0.73	3.18	0.04	0.23	Equivocal
350.86	0.00	0.00	0.58	0.29	0.10	Below Det.	0.97	3.10	0.00	0.31	Equivocal

Table A2. Total organic carbon, raw iron speciation data, and calculations recorded in weight % for drill core MCDD0003 from the McArthur Basin.

Sample Depth	% N	% C	FeCarb	FeMag	FeOx	FePy	FeHR	FeT	FePy / FeHR	FeHR / FeT	Interpretation
8.67	0.02	0.17	0.12	0.18	0.03	Below Det.	0.33	1.91	0.00	0.17	Oxic
13.7	0.02	0.67	0.35	0.07	0.05	0.13	0.60	1.85	0.22	0.32	Equivocal
20.35	0.01	0.04	0.17	0.10	0.04	0.00	0.32	2.32	0.01	0.14	Oxic
26.55	0.02	0.06	0.16	0.69	0.05	Below Det.	0.90	3.27	0.00	0.27	Equivocal
31.96	0.00	0.04	0.08	0.15	0.03	Below Det.	0.26	2.29	0.00	0.11	Oxic
49.25	0.00	0.21	0.50	0.06	0.02	Below Det.	0.58	0.86	0.00	0.67	Ferruginous
55.97	0.00	0.14	0.73	0.09	0.00	0.02	0.85	1.38	0.02	0.61	Ferruginous
67.95	0.02	0.29	0.84	0.07	0.03	0.29	1.23	1.41	0.24	0.88	Ferruginous
77.26	0.02	0.17	0.34	0.08	0.01	0.59	1.01	1.88	0.58	0.54	Ferruginous
79.62	0.01	0.12	0.22	0.07	0.03	0.34	0.65	1.71	0.52	0.38	Equivocal
84.6	0.02	0.15	0.54	0.07	0.03	0.44	1.07	1.57	0.41	0.69	Ferruginous
95	0.02	0.54	0.88	0.06	0.01	0.14	1.08	1.20	0.13	0.90	Ferruginous
163.06	0.02	0.28	0.36	0.11	0.02	0.42	0.90	1.99	0.47	0.45	Ferruginous
177.7	0.02	0.25	0.31	0.24	0.21	Below Det.	0.76	4.32	0.00	0.18	Oxic
179.13	0.02	0.47	0.38	0.17	0.07	0.28	0.91	3.15	0.31	0.29	Equivocal
179.28	0.02	0.32	0.36	0.16	0.08	0.09	0.69	3.22	0.14	0.22	Oxic
184.3	0.01	0.08	0.69	0.23	0.11	0.24	1.27	2.95	0.19	0.43	Ferruginous
187.88	NA		0.74	0.14	0.06	NA	0.94	2.37	0.00	0.40	Ferruginous
190.84	0.02	0.14	0.47	0.18	0.12	0.06	0.83	2.93	0.08	0.28	Equivocal
194	0.02	0.11	0.43	0.13	0.07	0.02	0.64	2.15	0.03	0.30	Equivocal
196.6	0.02	0.07	0.44	0.16	0.11	0.01	0.72	2.73	0.02	0.27	Equivocal
224.3	0.01	0.09	0.27	0.10	0.03	0.00	0.40	1.73	0.01	0.23	Equivocal
243.7	0.01	0.10	0.18	0.15	0.11	0.03	0.47	1.76	0.06	0.27	Equivocal
353.12	0.02	0.06	0.21	0.15	0.14	0.02	0.52	3.01	0.03	0.17	Equivocal
502.66	0.01	0.05	0.39	0.19	0.13	Below Det.	0.72	3.00	0.00	0.24	Equivocal
516.86	0.02	0.13	0.76	0.21	0.21	NA	1.18	3.21	0.00	0.37	Ferruginous
521.12	0.01	0.11	0.82	0.18	0.07	Below Det.	1.06	2.79	0.00	0.38	Ferruginous
529.73	0.02	0.20	0.62	0.18	0.11	0.22	1.12	4.63	0.20	0.24	Equivocal
537.24	0.02	0.08	0.76	0.13	0.09	0.09	1.06	2.52	0.08	0.42	Ferruginous
554.83	0.05	2.00	0.66	0.11	0.14	3.96	4.87	7.52	0.81	0.65	Euxinic

Table A3. Total organic carbon, raw iron speciation data, and calculations recorded in weight % for drill core MCDD0005 from the McArthur Basin.

Sample Depth	% N	% C	FeCarb	FeMag	FeOx	FePy	FeHR	FeT	FePy / FeHR	FeHR / FeT	Interpretation
68.14	0.06	2.16	0.74	0.14	0.05	0.68	1.61	2.03	0.42	0.79	Ferruginous
70.78	0.05	2.45	0.74	0.30	0.04	1.02	2.10	2.20	0.49	0.95	Ferruginous
86.4	0.06	2.82	0.54	0.21	0.03	0.29	1.07	1.76	0.28	0.61	Ferruginous
128.03	0.03	0.78	0.46	0.11	0.08	0.44	1.09	2.32	0.41	0.47	Ferruginous
137.05	0.03	0.65	0.45	0.11	0.08	0.36	1.01	1.99	0.36	0.51	Ferruginous
165.9	0.03	0.50	0.45	0.12	0.08	0.45	1.10	2.01	0.41	0.55	Ferruginous
178.8	0.03	0.54	0.45	0.18	0.08	0.49	1.20	2.34	0.41	0.51	Ferruginous
190.25	0.03	0.68	0.50	0.11	0.10	0.56	1.27	2.29	0.44	0.55	Ferruginous
206.03	0.03	0.48	0.51	0.21	0.10	0.54	1.36	2.58	0.39	0.53	Ferruginous
225.5	0.03	0.68	0.47	0.14	0.09	0.60	1.31	2.52	0.46	0.52	Ferruginous
266.02	0.04	1.09	0.59	0.12	0.11	0.39	1.20	2.07	0.32	0.58	Ferruginous
276.35	0.03	0.42	0.43	0.14	0.13	0.29	0.99	2.45	0.29	0.40	Ferruginous
364.58	0.02	0.27	0.90	0.21	0.40	0.08	1.60	5.48	0.05	0.29	Equivocal
380.8	0.02	0.22	0.94	0.17	0.33	Below Det.	1.45	3.32	0.00	0.44	Ferruginous
395.8	0.01	0.19	0.95	0.12	0.14	0.01	1.22	2.32	0.01	0.53	Ferruginous
446.9	0.02	0.11	0.64	0.08	0.02	Below Det.	0.74	1.00	0.00	0.74	Ferruginous

Table A4. Total organic carbon, raw iron speciation data, and calculations recorded in weight % for drill core McA5 from the McArthur Basin.

A. Raw Data: Iron Speciation and Total Organic Carbon Content

Sample Depth	% N	% C	FeCarb	FeMag	FeOx	FePy	FeHR	FeT	FePy / FeHR	FeHR / FeT	Interpretation
112.92	0.05	0.09	0.40	0.17	0.57	Below Det	1.14	7.76	0.00	0.15	Oxic
117.3	0.04	0.08	0.33	0.08	0.25	0.04	0.71	2.83	0.06	0.25	Equivocal
122.3	0.06	0.14	0.41	0.19	0.60	0.02	1.22	8.27	0.01	0.15	Oxic
128.25	0.06	0.46	0.05	0.16	0.13	0.04	0.38	2.08	0.10	0.18	Oxic
137.45	0.05	0.36	0.29	0.11	0.28	0.02	0.71	4.71	0.03	0.15	Oxic
147.3	0.05	0.18	0.13	0.26	0.28	0.07	0.74	3.30	0.10	0.22	Equivocal
148.93	0.04	0.17	0.27	0.11	0.21	0.02	0.60	3.18	0.03	0.19	Oxic
158.1	0.03	0.12	0.44	0.14	0.25	0.05	0.87	4.10	0.05	0.21	Oxic
168.1	0.05	0.16	0.09	0.11	0.11	0.02	0.33	2.66	0.06	0.12	Oxic
178	0.04	0.20	0.32	0.11	0.16	0.06	0.65	2.85	0.10	0.23	Equivocal
187.68	0.04	0.18	0.35	0.35	0.29	0.08	1.07	3.46	0.08	0.31	Equivocal
197.85	0.04	0.22	0.28	0.11	0.21	0.01	0.62	3.46	0.02	0.18	Oxic
200.8	0.03	0.18	0.32	0.12	0.20	0.02	0.66	3.52	0.03	0.19	Oxic
206.3	0.04	0.27	0.35	0.13	0.20	0.04	0.71	3.38	0.05	0.21	Oxic
216.99	0.04	0.34	0.41	0.77	0.24	0.28	1.70	4.45	0.16	0.38	Ferruginous
230.4	0.03	0.34	0.15	1.05	0.31	0.16	1.67	3.53	0.09	0.47	Ferruginous
239.1	0.03	0.28	0.32	0.24	0.19	0.09	0.84	3.62	0.11	0.23	Equivocal
247.48	0.04	0.73	0.16	0.43	0.20	0.24	1.03	3.40	0.24	0.30	Equivocal
253.72	0.04	0.07	0.18	0.07	0.12	Below Det	0.38	3.34	0.00	0.11	Oxic
262.1	0.04	0.24	0.30	0.11	0.20	0.03	0.64	3.44	0.04	0.19	Oxic
285.76	0.04	0.27	0.16	0.10	0.10	0.04	0.41	2.78	0.11	0.15	Oxic
288.68	0.03	0.17	0.24	0.11	0.24	0.02	0.62	3.48	0.04	0.18	Oxic
291.42	0.03	0.20	0.28	0.68	0.29	0.05	1.31	4.67	0.04	0.28	Equivocal
301.7	0.03	0.15	0.40	0.15	0.25	0.02	0.81	3.97	0.03	0.20	Oxic
307.1	0.04	0.09	0.30	0.14	0.28	Below Det	0.72	5.11	0.00	0.14	Oxic
312.47	0.04	0.11	0.28	0.14	0.21	Below Det	0.64	4.54	0.00	0.14	Oxic
331.95	0.03	0.08	0.14	0.18	0.22	0.01	0.55	3.41	0.01	0.16	Oxic
335.3	0.03	0.09	0.31	0.15	0.10	Below Det	0.56	2.94	0.00	0.19	Oxic
350.2	0.03	0.08	0.08	0.15	0.14	Below Det	0.37	3.07	0.00	0.12	Oxic
373.23	0.04	0.09	0.22	0.10	0.03	Below Det	0.35	3.18	0.00	0.11	Oxic
387.03	0.04	0.10	0.17	0.11	0.03	Below Det	0.31	3.85	0.00	0.08	Oxic
403.25	0.03	0.01	0.15	0.11	0.04	Below Det	0.30	3.57	0.00	0.08	Oxic
479.55	0.03	0.04	0.08	0.10	0.03	0.04	0.25	3.19	0.16	0.07	Oxic
480.15	0.04	0.08	0.30	0.12	0.04	Below Det	0.46	3.36	0.00	0.14	Oxic
489.3	0.03	0.09	0.38	0.07	0.03	0.01	0.50	2.84	0.02	0.17	Oxic
493.64	0.03	0.17	0.68	0.10	0.03	0.03	0.84	2.23	0.03	0.36	Equivocal

Table A5. Total organic carbon, raw iron speciation data, and calculations recorded in weight % for drill core Broughton-1 from the McArthur Basin.

Sample Depth	% N	% C	FeCarb	FeMag	FeOx	FePy	FeHR	FeT	FePy / FeHR	FeHR / FeT	Interpretation
68.76	0.01	0.07	0.16	0.10	0.06	0.05	0.37	2.79	0.14	0.13	Oxic
80.9	0.01	0.10	0.15	0.17	0.03	0.07	0.42	2.02	0.17	0.21	Oxic
87.7	0.01	0.13	0.13	0.09	0.02	0.05	0.29	1.98	0.16	0.15	Oxic
92.4	0.02	0.12	0.42	0.08	0.02	0.26	0.78	2.32	0.34	0.34	Equivocal
111.1	0.02	0.27	0.33	0.18	0.01	0.45	0.98	1.62	0.46	0.60	Ferruginous
148.8	0.02	0.44	0.32	0.74	0.01	0.05	1.13	1.79	0.05	0.63	Ferruginous
150.08	0.03	0.48	0.33	0.19	0.02	0.49	1.04	1.94	0.47	0.53	Ferruginous
176.27	0.02	0.08	0.26	0.08	0.02	0.24	0.61	1.99	0.39	0.30	Equivocal
182.19	0.01	0.09	0.31	0.09	0.02	0.32	0.75	1.85	0.43	0.40	Ferruginous
190.2	0.02	0.15	0.32	0.13	0.06	0.15	0.65	2.05	0.23	0.32	Equivocal
201.64	0.02	0.06	0.13	0.12	0.06	Below Det.	0.32	2.76	0.00	0.12	Oxic
204.6	0.02	0.07	0.28	0.10	0.05	0.20	0.64	2.43	0.32	0.26	Equivocal
216.8	0.02	0.03	0.47	1.04	0.11	Below Det.	1.62	4.52	0.00	0.36	Equivocal
220.68	0.02	0.02	0.19	0.18	0.05	0.06	0.48	3.01	0.12	0.36	Equivocal
225.86	0.02	0.22	0.39	0.28	0.02	0.16	0.84	2.20	0.19	0.38	Ferruginous
256.5	0.01	0.08	0.44	0.15	0.01	0.29	0.88	1.42	0.32	0.62	Ferruginous
274.13	0.01	0.02	0.10	0.08	0.01	0.01	0.20	3.27	0.06	0.06	Oxic
288.58	0.01	0.04	0.18	0.11	0.01	0.07	0.37	2.01	0.19	0.18	Oxic

Table A6. Total organic carbon, raw iron speciation data, and calculations recorded in weight % for drill core DD90VRB2 from the Birrindudu Basin.

Sample Depth	% N	% C	FeCarb	FeMag	FeOx	FePy	FeHR	FeT	FePy / FeHR	FeHR / FeT	Interpretation
151.55	0.01	0.27	0.08	0.04	0.01	0.25	0.39	0.94	0.65	0.41	Ferruginous
157.9	0.02	1.59	0.33	0.06	0.03	0.06	0.48	1.14	0.13	0.42	Ferruginous
161.97	0.01	0.01	0.16	0.25	0.02	Below Det.	0.43	1.88	0.00	0.23	Equivocal
352.73	0.02	0.10	0.15	0.07	0.02	Below Det.	0.24	2.10	0.00	0.11	Oxic
365.4	0.02	0.03	0.31	0.13	0.06	0.12	0.63	3.46	0.20	0.18	Oxic
400.6	0.02	0.05	0.49	0.14	0.09	Below Det.	0.72	3.35	0.00	0.21	Oxic
409.65	0.02	0.10	0.21	0.13	0.08	0.11	0.53	3.32	0.20	0.16	Oxic
413.7			0.24	0.13	0.12	0.06	0.55	3.41	0.10	0.16	Oxic
417.4			0.31	0.14	0.18	Below Det.	0.63	3.56	0.00	0.18	Oxic
420.27	0.02	0.07	0.39	0.16	0.14	0.01	0.69	3.46	0.01	0.20	Oxic
428	0.02	0.09	0.32	0.15	0.15	0.00	0.62	3.39	0.01	0.18	Oxic

Table A7. Total organic carbon, raw iron speciation data, and calculations recorded in weight % for drill core DD90VRB1 from the Birrindudu Basin.

Sample Depth	% N	% C	FeCarb	FeMag	FeOx	FePy	FeHR	FeT	FePy / FeHR	FeHR / FeT	Interpretation
64.7	0.04	0.56	0.26	0.10	0.16	0.01	0.53	2.92	0.01	0.1815	Oxic
74.25	0.02	0.27	0.29	0.07	0.09	0.01	0.46	2.24	0.01	0.2049	Oxic
82.1	0.02	0.06	0.29	0.09	0.16	0.01	0.55	2.71	0.01	0.2015	Oxic
94.7	0.03	0.11	0.59	0.25	0.63	Below Det.	1.47	5.53	0.00	0.2662	Equivocal
96.8	0.03	0.22	0.39	0.15	0.32	Below Det.	0.87	3.95	0.00	0.2193	Oxic
107.62	0.03	0.35	0.37	0.16	0.37	Below Det.	0.90	4.10	0.00	0.2200	Oxic
115.6	0.03	0.10	0.46	0.21	0.45	0.01	1.13	4.71	0.00	0.2396	Equivocal
122.27	0.03	0.12	0.57	0.24	0.55	Below Det.	1.36	6.60	0.00	0.2052	Oxic
185.47	0.05	0.07	0.09	0.07	0.03	Below Det.	0.19	2.84	0.00	0.0662	Oxic
198.85	0.03	0.08	0.25	0.10	0.05	0.02	0.41	3.20	0.04	0.1283	Oxic
201.85	0.03	0.05	0.20	0.09	0.04	Below Det.	0.33	3.59	0.00	0.0933	Oxic
204.85	0.03	0.14	0.31	0.11	0.05	0.01	0.48	3.39	0.03	0.1415	Oxic
211.05	0.02	0.18	0.25	0.09	0.04	0.01	0.39	2.38	0.04	0.1629	Oxic
216.9	0.02	0.05	0.42	0.17	0.19	0.02	0.81	4.83	0.03	0.1684	Oxic
225.12	0.03	0.16	0.18	0.10	0.07	0.01	0.35	3.06	0.02	0.1150	Oxic
239.02	0.03	0.13	0.36	0.11	0.02	0.00	0.49	2.34	0.00	0.2085	Oxic
243.14	0.04	0.61	0.14	0.12	0.03	0.07	0.36	2.94	0.20	0.1242	Oxic
251.1	0.03	0.13	0.16	0.12	0.04	Below Det.	0.31	3.64	0.00	0.0850	Oxic
259	0.02	0.07	0.16	0.11	0.02	0.00	0.30	3.24	0.01	0.0914	Oxic
271.28	0.03	0.05	0.18	0.59	0.03	Below Det.	0.80	4.11	0.00	0.1953	Oxic
292.73	0.02	0.04	0.31	0.10	0.01	Below Det.	0.43	3.08	0.00	0.1381	Oxic
319.08	0.02	0.08	0.17	0.12	0.10	Below Det.	0.40	3.24	0.00	0.1228	Oxic
323.2	0.03	0.43	0.13	0.11	0.08	0.00	0.33	2.79	0.00	0.1177	Oxic
330.08	0.02	0.07	0.15	0.15	0.05	0.06	0.42	3.44	0.15	0.1228	Oxic
342.3	0.02	0.31	0.21	0.17	0.14	0.01	0.53	2.70	0.02	0.1956	Oxic

Table A8. Total organic carbon, raw iron speciation data, and calculations recorded in weight % for drill core 99VRNTGSDD2 from the Birrindudu Basin.

	Replicate G306 - 150			Replicate G155 - 83.6			Replicate G435 - 45		
	Ext. 1	Ext. 2	Ext. 3	Ext. 1	Ext. 2	Ext. 3	Ext. 1	Ext. 2	Ext. 3
	1.65	0.87	0.06	0.04	0.09	0.01	0.38	0.53	0.20
	1.73	0.70	0.07	0.03	0.07	0.02	0.32	0.44	0.19
	1.73	0.86	0.07	0.02	0.07	0.01	0.33	0.50	0.17
	1.65	0.84	0.04	0.01	0.07	0.00	0.32	0.45	0.14
Average	1.69	0.82	0.06	0.03	0.07	0.01	0.34	0.48	0.17
Std. Deviation	0.05	0.08	0.01	0.01	0.01	0.01	0.03	0.04	0.03
% Std. Deviation	2.86	9.53	19.68	36.62	11.94	72.59	9.21	8.67	15.94
% Standard Error of the Mean	2.42	3.89	0.59	0.46	0.45	0.30	1.55	2.07	1.38

Table A9. Internal replicates underwent identical sequential extraction of highly reactive iron and were analyzed alongside every sample batch. A summary of the weight percent iron at every step of extraction is shown above. Ext. 1 is the Acetate extraction of iron-carbonates, Ext. 2 represents the dithionite extraction of iron-oxides, and Ext. 3 is the extraction of iron in magnetite via oxalate. The average, standard deviation, percent standard deviation, and standard error of the mean are also shown.

B. Raw Data: Major Element Geochemistry

Sample Depth	Co ₃ O ₄	CuO	NiO	SiO ₂	Al ₂ O ₃	Fe ₂ O ₃ (T)	MnO	MgO	CaO	Na ₂ O	K ₂ O	TiO ₂	P ₂ O ₅	Cr ₂ O ₃	V ₂ O ₅	LOI	Total
480.37	< 0.005	< 0.005	< 0.003	50.89	24.49	5.3	0.013	2.4	0.28	0.21	9.15	0.87	0.16	0.01	0.023	5.89	99.71
484.55	< 0.005	< 0.005	0.005	67.86	14.48	4.8	0.008	2.31	0.2	0.14	6.91	0.57	0.11	0.02	0.006	3.23	100.7
487.47	< 0.005	0.014	0.005	58.91	15.4	3.32	0.076	3.51	2.88	0.15	6.55	0.53	0.1	0.01	0.009	7.99	99.45
497	< 0.005	0.008	< 0.003	50.44	10.12	4.25	0.188	5.79	8.19	0.18	4.54	0.4	0.08	0.01	0.007	14.42	98.6
502	< 0.005	0.045	< 0.003	63.49	15.8	4.16	0.012	2.84	0.45	0.14	6.65	0.54	0.13	0.01	0.014	5.08	99.36
507.25	< 0.005	0.007	< 0.003	62.5	16.66	3.61	0.009	2.65	0.24	0.21	6.89	0.58	0.1	0.01	0.012	5.05	98.52
512.86	< 0.005	< 0.005	< 0.003	61.37	15.72	4.43	0.013	2.76	2.26	0.13	6.24	0.55	0.17	0.01	0.014	6.25	99.91
518.03	< 0.005	< 0.005	< 0.003	44.22	11.61	2.98	0.084	2.81	15.59	0.15	4.8	0.35	0.11	< 0.01	0.008	16.34	99.04
529.28	< 0.005	< 0.005	< 0.003	48.31	11.19	4.03	0.155	6.14	9.21	0.15	5.05	0.42	0.12	< 0.01	0.007	15.34	100.1
537.04	< 0.005	< 0.005	0.005	61.55	16.68	4.95	0.013	2.69	0.44	0.12	5.98	0.54	0.11	0.02	0.017	5.48	98.58
546.07	< 0.005	0.006	0.006	34.43	8.43	2.94	0.058	1.34	25.87	0.12	2.7	0.3	0.21	0.01	0.006	22.42	98.85
549.07	< 0.005	< 0.005	< 0.003	48.32	11.45	4.45	0.071	1.9	14.32	0.12	4.02	0.45	0.13	0.01	0.01	14.53	99.78
559	< 0.005	< 0.005	0.004	54.08	14.65	4.79	0.024	2.21	6.78	0.14	5.08	0.54	0.21	0.01	0.015	10.87	99.4
567.3	< 0.005	0.01	< 0.003	50.64	14.85	5.37	0.032	2.18	7.72	< 0.01	4.86	0.53	0.23	< 0.01	0.014	11.98	97.99
577	< 0.005	< 0.005	< 0.003	56.93	17.75	5.16	0.02	2.6	2.35	0.17	5.93	0.62	0.16	0.01	0.021	8.22	99.93
589.42	< 0.005	< 0.005	< 0.003	50.73	14.91	4.58	0.034	2.16	8.55	0.09	5.09	0.57	0.23	< 0.01	0.018	12.32	99.3
592.7	< 0.005	< 0.005	0.005	60.24	15.6	6.29	0.023	2.63	1.9	0.18	5.51	0.57	0.14	0.01	0.013	5.78	98.88
598.17	< 0.005	< 0.005	0.014	61.67	17.17	5.1	0.018	2.5	0.31	< 0.01	5.89	0.58	0.14	0.02	0.017	5.48	98.83
610.75	< 0.005	0.006	0.006	46.57	13.8	4.34	0.038	2.39	12.67	0.17	4.6	0.5	0.27	0.02	0.015	14.57	99.95
613.5	< 0.005	< 0.005	0.005	54.13	11.74	4.18	0.062	2.31	9.43	0.14	3.96	0.46	0.27	0.01	0.015	13.26	99.98
620.55	< 0.005	< 0.005	0.006	59.74	16.61	5.86	0.014	2.61	0.44	0.09	5.9	0.63	0.16	0.01	0.018	6.16	98.28
621.4	< 0.005	< 0.005	0.004	63.69	12.77	5.98	0.02	2.35	2.02	0.13	5.45	0.49	0.31	< 0.01	0.015	4.98	98.21
630.8	< 0.005	< 0.005	< 0.003	61.72	16.64	5.62	0.015	2.81	0.61	0.14	5.82	0.62	0.18	0.01	0.014	5.08	99.27
640.55	< 0.005	< 0.005	< 0.003	64.31	14.4	5.81	0.01	2.7	1.46	0.23	5.14	0.61	0.14	< 0.01	0.006	4.51	99.33
650.24	< 0.005	< 0.005	< 0.003	60.57	17.22	5.11	0.01	3.16	0.5	0.14	5.84	0.58	0.25	0.01	0.02	5.4	98.8
657.13	< 0.005	0.005	< 0.003	30.78	10.3	5.56	0.568	9.8	15.11	0.07	3.14	0.37	0.14	0.01	0.006	24.27	100.1
667.54	< 0.005	< 0.005	0.013	31.08	7.78	3.25	0.258	10.75	16.06	0.1	3.2	0.36	0.19	0.02	0.005	25.43	98.5
678.07	< 0.005	0.011	0.005	37.77	10.81	4.18	0.369	8.19	12.47	0.28	3.83	0.42	0.14	0.01	0.011	20.78	99.27
687.35	< 0.005	< 0.005	< 0.003	47.98	12.26	3.03	0.163	6.56	8.29	0.14	5.17	0.47	0.18	0.01	0.011	15.29	99.55
689.2	< 0.005	0.009	< 0.003	40.99	11.34	4.12	0.326	7.84	11.01	0.1	4.06	0.43	0.12	< 0.01	0.013	19.04	99.42
700.3	< 0.005	< 0.005	< 0.003	60.41	15.01	4.48	0.044	2.71	4	0.16	5.74	0.58	0.19	< 0.01	0.016	7.07	100.4

Table A10. Major element geochemistry recorded in weight % for drill core GSD7 from the McArthur Basin.

Sample Depth	Co ₃ O ₄	CuO	NiO	SiO ₂	Al ₂ O ₃	Fe ₂ O ₃ (T)	MnO	MgO	CaO	Na ₂ O	K ₂ O	TiO ₂	P ₂ O ₅	Cr ₂ O ₃	V ₂ O ₅	LOI	Total
8.73	< 0.005	0.024	< 0.003	38.19	10.42	3.69	0.509	8.29	12.66	0.12	5.3	0.49	0.13	0.01	0.008	20.49	100.3
9.65	< 0.005	0.033	< 0.003	40.84	12.25	3.43	0.411	6.95	10.62	0.05	7.24	0.48	0.15	< 0.01	0.023	17.52	100
17.75	< 0.005	< 0.005	< 0.003	37.78	9.61	5.25	0.439	8.22	12.67	0.11	5.16	0.34	0.14	< 0.01	0.018	20	99.75
25.5	< 0.005	0.006	< 0.003	45.03	8.26	4.73	0.405	7.51	11.72	0.1	3.74	0.33	0.12	< 0.01	0.018	18.67	100.7
32.55	0.007	0.011	0.004	55.8	13.39	8.68	0.05	2.64	1.83	0.1	6.84	0.57	0.17	< 0.01	0.055	9.03	99.18
38.6	< 0.005	< 0.005	0.004	64.98	7.53	5.77	0.051	1.88	3.09	< 0.01	4.96	0.3	0.53	< 0.01	0.013	9.28	98.36
41.85	< 0.005	< 0.005	0.004	58.42	14.62	5.65	0.02	1.69	1.09	0.09	9.37	0.6	0.13	0.01	0.021	7.59	99.3
54.95	NA	NA	NA	NA	NA	NA	NA	NA	NA	NA	NA	NA	NA	NA	NA	NA	NA
65.27	< 0.005	0.068	0.005	50.16	10.02	2.45	0.214	5.95	9.24	0.17	6.63	0.41	0.19	0.02	0.009	14.81	100.3
73.35	< 0.005	< 0.005	< 0.003	49.09	14	4.58	0.228	5.86	5.72	0.09	6.24	0.47	0.14	0.01	0.013	12.25	98.7
86.3	< 0.005	< 0.005	0.005	47.17	13.24	4.9	0.169	7.88	6.62	0.07	4.28	0.45	0.15	0.02	0.013	14.28	99.24
92.32	< 0.005	< 0.005	< 0.003	53.93	14.01	5.43	0.069	9.01	2.51	0.06	3.73	0.55	0.16	< 0.01	0.013	9.19	98.67
96.96	< 0.005	< 0.005	< 0.003	52.83	17	6.47	0.014	10.05	0.39	0.09	4.23	0.66	0.23	0.01	0.019	7.19	99.17
215.52	0.007	0.016	< 0.003	64.55	6.05	10.21	0.14	9.77	1.01	0.05	0.18	0.23	0.15	0.01	0.005	6.36	98.72
225.05	< 0.005	< 0.005	0.007	46.82	18.68	4.25	0.235	5.15	4.72	0.11	7.43	0.67	0.22	0.02	0.038	11.39	99.73
255.85	< 0.005	< 0.005	< 0.003	50.18	24.43	4.37	0.006	2.52	0.26	0.19	9.33	1.11	0.16	0.02	0.034	5.87	98.47
266.7	< 0.005	< 0.005	0.008	53.98	22.18	3.95	0.004	2.24	0.25	0.14	9.18	0.92	0.15	0.02	0.044	5.43	98.5
270.9	< 0.005	0.005	< 0.003	56.48	21.27	3.98	0.006	2.01	0.37	0.16	9.2	0.94	0.23	0.02	0.03	4.58	99.28
279.27	< 0.005	< 0.005	< 0.003	56.02	20.79	4.41	0.004	1.92	0.24	0.15	8.7	1.05	0.17	0.01	0.031	5.14	98.64
281.4	< 0.005	< 0.005	0.013	55.92	21.78	4.5	0.006	2.24	0.2	0.23	9	0.86	0.13	0.01	0.028	5.35	100.3
289.62	< 0.005	0.008	< 0.003	58.93	18.5	5.61	0.009	2.07	0.29	0.17	7.61	0.85	0.16	0.01	0.028	4.82	99.06
295.14	< 0.005	< 0.005	< 0.003	54	22.02	5.01	0.006	2.05	0.2	0.18	8.96	1.23	0.13	0.02	0.04	5	98.85
304.49	< 0.005	< 0.005	0.004	63.06	15.63	5.63	0.041	2.13	0.24	0.12	6.83	0.73	0.16	0.01	0.014	4.66	99.25
309.7	< 0.005	< 0.005	0.004	62.19	17.75	3.57	0.006	1.88	0.35	0.15	7.64	0.8	0.24	0.02	0.021	4.05	98.68
335.47	< 0.005	< 0.005	< 0.003	57.28	20.34	3.94	0.01	2.11	0.47	0.16	8.32	0.9	0.25	0.01	0.019	5.29	99.11
335.9	< 0.005	< 0.005	< 0.003	60.74	19.32	3.71	0.008	1.89	0.28	0.14	8.02	0.82	0.17	0.02	0.019	4.53	99.67
347.14	< 0.005	< 0.005	0.004	60.98	17.9	4.54	0.006	1.8	0.27	0.13	7.84	0.81	0.19	0.01	0.031	4.21	98.73
350.86	< 0.005	< 0.005	< 0.003	65.64	15.17	4.43	0.012	1.95	0.52	0.12	6.81	0.79	0.15	< 0.01	0.015	4.06	99.67

Table A11. Major element geochemistry recorded in weight % for drill core MCDD0003 from the McArthur Basin.

Sample Depth	Co ₃ O ₄	CuO	NiO	SiO ₂	Al ₂ O ₃	Fe ₂ O ₃ (T)	MnO	MgO	CaO	Na ₂ O	K ₂ O	TiO ₂	P ₂ O ₅	Cr ₂ O ₃	V ₂ O ₅	LOI	Total
8.67	< 0.005	0.023	< 0.003	66.2	15.29	2.73	0.01	2.12	0.37	0.12	8.1	0.5	0.08	< 0.01	0.009	4.05	99.6
13.7	< 0.005	< 0.005	< 0.003	67.58	13.26	2.64	0.015	1.76	0.79	0.12	7.57	0.53	0.11	< 0.01	0.007	4.34	98.72
20.35	< 0.005	< 0.005	< 0.003	62.47	17.06	3.31	0.009	1.82	0.16	0.14	8.89	0.69	0.09	0.01	0.009	3.86	98.52
26.55	< 0.005	< 0.005	< 0.003	56.95	19.42	4.68	0.012	2.38	0.26	0.14	9.34	0.73	0.08	0.01	0.012	4.96	98.98
31.96	< 0.005	< 0.005	0.003	58.51	19.67	3.27	0.006	1.83	0.14	0.15	10.32	0.97	0.1	0.01	0.01	4	99.01
49.25	< 0.005	0.005	0.005	56.97	10.46	1.23	0.041	4.85	6.7	0.14	6.6	0.6	0.07	0.01	0.003	11.65	99.32
55.97	< 0.005	0.007	< 0.003	42.15	8.86	1.97	0.082	8.91	12.47	0.17	4.99	0.33	0.07	0.01	0.006	20.17	100.2
67.95	< 0.005	0.009	< 0.003	38.15	8.82	2.01	0.082	9.39	13.61	0.26	5.32	0.39	0.08	0.01	0.005	21.37	99.52
77.26	< 0.005	0.009	< 0.003	57.02	16.96	2.69	0.02	2.8	1.89	0.1	10.52	0.58	0.12	< 0.01	0.012	6.49	99.21
79.62	< 0.005	< 0.005	< 0.003	58.22	17.12	2.44	0.014	2.81	1.81	0.11	10.15	0.61	0.21	< 0.01	0.014	6.1	99.62
84.6	< 0.005	0.008	< 0.003	54.84	13.1	2.24	0.035	4.63	5.57	0.12	7.67	0.46	0.14	0.01	0.007	10.85	99.68
95	< 0.005	< 0.005	< 0.003	37.44	8.66	1.72	0.074	9.56	13.69	0.13	5.25	0.37	0.25	< 0.01	0.004	21.68	98.82
163.06	< 0.005	0.032	0.01	50.36	14.08	2.85	0.057	5.33	5.66	0.14	8.57	0.63	0.4	0.01	0.022	11.3	99.46
177.7	< 0.005	< 0.005	0.012	58.3	16.45	6.17	0.012	2.86	0.22	0.13	9.97	0.77	0.11	0.03	0.047	4.88	99.97
179.13	< 0.005	< 0.005	0.011	56.52	16.02	4.5	0.031	3.12	1.57	0.13	10.25	0.7	0.14	0.03	0.044	6.56	99.64
179.28	< 0.005	0.011	0.01	56.7	15.7	4.61	0.039	3.6	2.07	0.12	9.73	0.66	0.17	0.01	0.041	7.04	100.5
184.3	< 0.005	0.006	< 0.003	47.44	12.04	4.22	0.094	6.72	6.75	0.14	6.95	0.46	0.15	0.01	0.01	13.73	98.73
187.88	0.005	0.02	0.015	41.21	10.4	3.99	0.17	8.01	10.18	0.24	6.19	0.42	0.14	0.02	0.011	18.29	98.71
190.84	< 0.005	0.006	< 0.003	51.98	12.9	4.19	0.072	5.78	5.24	0.13	7.27	0.49	0.14	0.01	0.013	11.33	99.55
194	< 0.005	0.009	< 0.003	36.8	8.36	3.07	0.163	10.62	13.35	0.18	4.32	0.34	0.17	< 0.01	0.01	22.32	99.7
196.6	< 0.005	0.005	< 0.003	47.95	10.89	3.9	0.095	7.54	7.71	0.15	5.61	0.42	0.1	0.01	0.013	14.7	99.1
224.3	< 0.005	0.008	0.012	60.94	13.63	2.48	0.032	3.34	2.74	0.12	8.93	0.51	0.18	0.03	0.011	6.84	99.79
243.7	< 0.005	< 0.005	0.015	45.21	8.82	2.51	0.113	11.65	9.01	0.16	4.59	0.33	0.1	0.02	0.007	17.17	99.71
353.12	< 0.005	< 0.005	0.005	56.59	19.71	4.3	0.014	1.93	0.32	0.17	10.61	0.79	0.16	0.01	0.011	3.92	98.54
502.66	< 0.005	< 0.005	< 0.003	47.49	14.16	4.29	0.191	6.37	6.49	0.15	6.9	0.47	0.14	0.01	0.013	13.35	100
516.86	< 0.005	< 0.005	< 0.003	49.77	14.95	4.59	0.235	4.84	5.37	0.14	7.55	0.68	0.17	0.01	0.018	11.45	99.78
521.12	< 0.005	0.005	< 0.003	44.28	12.98	3.99	0.418	6.12	8.7	0.16	8	0.4	0.13	< 0.01	0.02	14.9	100.1
529.73	< 0.005	0.236	< 0.003	47.87	13.27	6.62	0.24	6.32	5.56	0.1	7.45	0.37	0.09	< 0.01	0.042	11.87	100
537.24	< 0.005	0.007	< 0.003	51.32	15.95	3.6	0.16	4.71	4.39	0.16	8.33	0.48	0.07	< 0.01	0.017	10.12	99.32
554.83	0.005	0.013	0.015	51.38	12.63	10.75	0.065	2.64	2.15	0.04	7.42	0.55	0.12	0.01	0.037	10.6	98.43

Table A12. Major element geochemistry recorded in weight % for drill core MCDD0005 from the McArthur Basin.

Sample Depth	Co ₃ O ₄	CuO	NiO	SiO ₂	Al ₂ O ₃	Fe ₂ O ₃ (T)	MnO	MgO	CaO	Na ₂ O	K ₂ O	TiO ₂	P ₂ O ₅	Cr ₂ O ₃	V ₂ O ₅	LOI	Total
68.14	< 0.005	0.007	0.008	46.77	7.9	2.9	0.129	7.31	10.47	0.15	4.02	0.32	0.08	0.02	0.008	18.34	98.43
70.78	< 0.005	< 0.005	< 0.003	53.05	8.92	3.15	0.062	5.45	7.67	0.15	5.14	0.36	0.2	0.01	0.011	15.69	99.86
86.4	< 0.005	0.007	< 0.003	35.82	5.95	2.51	0.065	10.47	15.74	0.15	2.6	0.23	0.16	< 0.01	0.01	24.7	98.43
128.03	< 0.005	0.008	< 0.003	50.98	10.31	3.32	0.076	6.93	8.08	0.25	4.31	0.43	0.11	0.01	0.006	15.29	100.1
137.05	< 0.005	< 0.005	< 0.003	50.92	8.86	2.84	0.105	7	8.79	0.37	3.62	0.36	0.18	0.01	0.005	15.65	98.72
165.9	< 0.005	< 0.005	< 0.003	48.29	8.07	2.87	0.05	7.38	11.18	0.34	2.94	0.32	0.08	< 0.01	0.004	17.3	98.83
178.8	< 0.005	< 0.005	< 0.003	49.06	10.01	3.35	0.05	6.97	9.3	0.45	3.75	0.38	0.1	< 0.01	0.007	15.96	99.38
190.25	< 0.005	0.006	< 0.003	48.93	8.6	3.28	0.068	7.06	10.16	0.45	3.12	0.36	0.1	< 0.01	0.008	16.85	98.99
206.03	< 0.005	< 0.005	0.003	51.22	9.97	3.69	0.064	6.12	8.14	0.43	3.72	0.42	0.1	0.01	0.008	14.71	98.61
225.5	< 0.005	< 0.005	< 0.003	51.85	10.03	3.6	0.048	6.32	8.4	0.43	3.75	0.41	0.11	0.01	0.009	14.57	99.55
266.02	0.03	< 0.005	0.01	50.99	10.16	2.96	0.066	6.16	8.59	0.59	4.28	0.41	0.14	0.01	0.018	14.18	98.6
276.35	< 0.005	< 0.005	0.007	49.42	12.13	3.51	0.061	7.65	6.93	0.51	4.57	0.42	0.11	0.01	0.021	13.68	99.03
364.58	0.007	< 0.005	0.011	56.53	10.66	7.83	1.099	4.34	4.64	< 0.01	4.18	0.48	0.26	0.02	0.006	9.64	99.71
380.8	< 0.005	< 0.005	< 0.003	41.52	8.99	4.74	0.548	8.3	11.76	0.15	4.35	0.43	0.26	0.01	0.003	19.27	100.3
395.8	< 0.005	< 0.005	< 0.003	33.49	7.2	3.31	0.334	10.46	15.43	0.17	3.68	0.27	0.16	< 0.01	0.004	25.51	100
446.9	0.011	0.007	< 0.003	53.08	12.57	1.43	0.028	5.33	6.62	0.11	9.11	0.45	0.1	0.01	0.009	11.24	100.1

Table A13. Major element geochemistry recorded in weight % for drill core McA5 from the McArthur Basin.

B. Raw Data: Major Element Geochemistry

Sample Depth	Co ₃ O ₄	CuO	NiO	SiO ₂	Al ₂ O ₃	Fe ₂ O ₃ (T)	MnO	MgO	CaO	Na ₂ O	K ₂ O	TiO ₂	P ₂ O ₅	Cr ₂ O ₃	V ₂ O ₅	LOI	Total
112.92	0.006	< 0.005	< 0.003	44.99	27.46	11.1	0.029	1.21	0.22	0.19	6.33	1.24	0.08	0.01	0.019	6.23	99.11
117.3	< 0.005	< 0.005	< 0.003	62.28	20.34	4.05	0.017	0.66	0.13	0.18	5.38	0.94	0.06	< 0.01	0.012	4.58	98.64
122.3	< 0.005	< 0.005	< 0.003	41.31	29.13	11.83	0.057	1.14	0.14	0.21	6.8	1.14	0.06	0.01	0.014	6.7	98.54
128.25	< 0.005	< 0.005	< 0.003	45.33	31.51	2.97	0.017	0.95	0.17	0.27	8.67	1.51	0.07	0.02	0.029	7.22	98.72
137.45	< 0.005	< 0.005	< 0.003	45.3	28.57	6.74	0.032	1.68	0.15	0.26	7.39	1.35	0.07	0.01	0.028	7.01	98.59
147.3	< 0.005	< 0.005	< 0.003	60.51	20.83	4.72	0.02	1.51	0.14	0.19	5.86	0.8	0.06	0.01	0.017	5.2	99.88
148.93	< 0.005	< 0.005	< 0.003	62.98	18.9	4.54	0.021	1.45	0.11	0.18	5.35	0.72	0.05	0.02	0.014	4.7	99.04
158.1	< 0.005	0.006	0.011	67.84	15.22	5.86	0.032	1.48	0.11	0.14	4.24	0.64	0.04	0.01	0.01	3.98	99.62
168.1	< 0.005	< 0.005	0.005	63.78	19.49	3.8	0.02	1.53	0.13	0.31	5.72	0.77	0.05	0.01	0.014	4.62	100.3
178	< 0.005	< 0.005	< 0.003	60.76	20.42	4.07	0.023	1.59	0.12	0.35	5.92	0.75	0.05	0.01	0.015	5.14	99.21
187.68	< 0.005	< 0.005	< 0.003	60.88	19.37	4.95	0.011	1.71	0.12	0.35	5.78	0.69	0.04	0.01	0.014	4.84	98.75
197.85	< 0.005	< 0.005	< 0.003	61.23	20.07	4.94	0.024	1.83	0.14	0.36	5.75	0.92	0.06	0.01	0.02	4.89	100.2
200.8	< 0.005	< 0.005	< 0.003	61.67	18.9	5.03	0.025	1.83	0.12	0.33	5.37	0.95	0.06	< 0.01	0.016	4.87	99.18
206.3	< 0.005	< 0.005	< 0.003	59.97	20.2	4.83	0.022	1.85	0.12	0.34	5.81	0.92	0.06	0.01	0.016	5.01	99.16
216.99	< 0.005	< 0.005	0.007	60.8	17.05	6.36	0.027	2	0.13	0.39	5.02	0.73	0.06	0.01	0.015	6.95	99.56
230.4	< 0.005	< 0.005	0.007	63.06	16.74	5.05	0.016	1.84	0.11	0.45	5.04	0.67	0.07	0.02	0.018	6.8	99.9
239.1	< 0.005	< 0.005	0.006	65.42	16.38	5.18	0.018	1.85	0.24	0.47	4.91	0.87	0.08	0.02	0.012	4.72	100.2
247.48	< 0.005	< 0.005	0.006	66.95	14.24	4.86	0.02	1.73	0.35	0.46	4.39	0.56	0.11	0.01	0.01	5	98.69
253.72	< 0.005	< 0.005	0.003	63.97	17.48	4.78	0.013	1.72	0.17	0.33	5.63	0.61	0.05	0.01	0.013	4.35	99.14
262.1	< 0.005	< 0.005	0.004	60.62	20.14	4.92	0.016	1.82	0.12	0.32	6.05	0.82	0.06	0.01	0.018	5.14	100.1
285.76	< 0.005	< 0.005	0.01	59.88	21.13	3.98	0.011	1.77	0.11	0.25	6.62	0.93	0.06	0.03	0.017	5.4	100.2
288.68	< 0.005	< 0.005	< 0.003	60.41	19.21	4.98	0.012	1.71	0.13	0.32	5.74	0.7	0.04	0.01	0.012	5.15	98.42
291.42	0.008	0.005	0.01	61.94	17.89	6.68	0.023	1.72	0.15	0.31	5.14	0.61	0.04	0.01	0.014	5.08	99.63
301.7	< 0.005	< 0.005	< 0.003	61.39	19.27	5.67	0.015	1.71	0.13	0.27	5.52	0.66	0.05	< 0.01	0.014	4.7	99.4
307.1	< 0.005	< 0.005	0.004	61.07	18.52	7.3	0.016	1.98	0.13	0.14	5.53	0.61	0.05	0.02	0.016	4.8	100.2
312.47	< 0.005	< 0.005	< 0.003	55.88	17.7	6.49	0.038	1.91	3.21	0.19	6	0.65	0.05	0.01	0.013	7.07	99.21
331.95	< 0.005	< 0.005	< 0.003	60.74	16.34	4.88	0.017	2.25	1.72	0.18	5.62	0.61	0.04	< 0.01	0.014	5.91	98.34
335.3	< 0.005	< 0.005	< 0.003	44.14	12.66	4.2	0.06	2.85	15.08	0.14	4.37	0.43	0.03	0.01	0.011	16.31	100.3
350.2	< 0.005	< 0.005	< 0.003	52.04	16.48	4.39	0.047	1.78	7.48	0.16	6.04	0.54	0.04	0.01	0.013	10.25	99.29
373.23	< 0.005	< 0.005	< 0.003	54.85	15.85	4.54	0.057	2.88	4.67	0.19	6.01	0.57	0.04	0.01	0.015	8.91	98.59
387.03	< 0.005	< 0.005	< 0.003	56.23	17.68	5.51	0.066	3.03	2.18	0.2	6.77	0.63	0.06	0.01	0.016	7.35	99.73
403.25	< 0.005	< 0.005	< 0.003	57.82	18.2	5.1	0.133	2.59	1.42	0.2	6.88	0.66	0.05	0.01	0.02	6.55	99.64
479.55	< 0.005	< 0.005	< 0.003	57.8	19.99	4.56	0.011	2.43	0.27	0.18	7.57	0.71	0.16	< 0.01	0.015	5.63	99.33
480.15	< 0.005	< 0.005	< 0.003	52.77	16.38	4.8	0.072	4.47	4	0.15	6.37	0.58	0.13	< 0.01	0.013	10.38	100.1
489.3	< 0.005	< 0.005	< 0.003	45.57	16.22	4.06	0.1	6.12	6.36	0.15	6.43	0.57	0.09	0.01	0.008	13.7	99.38
493.64	< 0.005	< 0.005	< 0.003	40.92	13.81	3.19	0.122	7.67	9.73	0.17	5.4	0.47	0.13	< 0.01	0.008	18.13	99.77

Table A14. Major element geochemistry recorded in weight % for drill core Broughton-1 from the McArthur Basin.

Sample Depth	Co ₃ O ₄	CuO	NiO	SiO ₂	Al ₂ O ₃	Fe ₂ O ₃ (T)	MnO	MgO	CaO	Na ₂ O	K ₂ O	TiO ₂	P ₂ O ₅	Cr ₂ O ₃	V ₂ O ₅	LOI	Total
151.55	< 0.005	< 0.005	0.006	54.93	19.86	1.34	0.001	4.02	0.52	0.07	9.28	0.42	0.1	< 0.01	0.005	7.81	98.36
157.9	< 0.005	< 0.005	< 0.003	54.77	10.69	1.63	0.03	5.31	6.76	0.13	6.91	0.46	0.21	0.01	0.02	13.42	100.3
161.97	< 0.005	< 0.005	< 0.003	64.7	16.01	2.69	0.009	1.96	0.31	0.15	8.83	0.6	0.05	0.01	0.007	3.77	99.1
352.73	< 0.005	< 0.005	< 0.003	56.19	15.27	3	0.025	4.11	3.23	0.15	7.39	0.53	0.07	0.01	0.014	8.86	98.85
365.4	0.013	0.005	0.009	50.79	18.14	4.95	0.042	4.03	2.99	0.19	8.54	0.58	0.08	0.02	0.011	8.78	99.18
400.6	< 0.005	< 0.005	< 0.003	58.16	16.29	4.79	0.081	3.14	2.07	0.21	7.58	0.43	0.07	< 0.01	0.009	7.12	99.95
409.65	< 0.005	< 0.005	< 0.003	59.1	18.46	4.75	0.015	2.41	0.12	0.21	8.34	0.41	0.05	0.01	0.012	4.9	98.78
413.7	< 0.005	< 0.005	< 0.003	60.67	17.57	4.88	0.016	2.37	0.11	0.29	8.04	0.46	0.06	0.01	0.013	4.77	99.26
417.4	< 0.005	< 0.005	< 0.003	62.75	16.95	5.09	0.015	2.38	0.15	0.23	7.87	0.48	0.07	0.02	0.012	4.44	100.5
420.27	< 0.005	< 0.005	< 0.003	61.89	16.75	4.95	0.016	2.43	0.16	0.21	7.23	0.52	0.08	0.01	0.009	4.27	98.54
428	< 0.005	< 0.005	< 0.003	63.62	16.13	4.85	0.017	2.24	0.14	0.18	7.29	0.51	0.07	0.01	0.008	4.21	99.29

Table A15. Major element geochemistry recorded in weight % for drill core DD90VRB2 from the Birrindudu Basin.

Sample Depth	Co ₃ O ₄	CuO	NiO	SiO ₂	Al ₂ O ₃	Fe ₂ O ₃ (T)	MnO	MgO	CaO	Na ₂ O	K ₂ O	TiO ₂	P ₂ O ₅	Cr ₂ O ₃	V ₂ O ₅	LOI	Total
68.76	< 0.005	< 0.005	< 0.003	60.24	18.1	3.99	0.006	1.9	0.14	0.08	9.25	0.62	0.06	0.01	0.01	4.66	99.06
80.9	< 0.005	0.163	< 0.003	63.19	16.32	2.89	0.003	1.47	0.17	0.07	10.1	0.51	0.06	0.01	0.009	3.86	98.83
87.7	< 0.005	< 0.005	0.006	61.26	17.66	2.83	0.005	1.74	0.1	0.09	9.78	0.57	0.04	0.02	0.012	4.44	98.57
92.4	< 0.005	< 0.005	0.006	56.45	12.27	3.32	0.041	4.84	5	0.1	5.78	0.46	0.12	0.02	0.01	11.28	99.69
111.1	< 0.005	< 0.005	< 0.003	50.82	14.25	2.31	0.026	4.92	5.22	0.11	8.17	0.48	0.08	< 0.01	0.007	12	98.41
148.8	< 0.005	< 0.005	< 0.003	60.42	16.89	2.56	0.004	2.01	0.26	0.09	10.12	0.53	0.05	0.01	0.011	6.21	99.16
150.08	< 0.005	< 0.005	< 0.003	51.68	11.28	2.77	0.043	6.42	7.25	0.11	4.96	0.46	0.15	< 0.01	0.011	14.52	99.65
176.27	< 0.005	< 0.005	< 0.003	55.16	14.56	2.85	0.032	4.71	3.5	0.11	8.76	0.46	0.14	< 0.01	0.009	8.88	99.19
182.19	< 0.005	< 0.005	< 0.003	51.61	12.67	2.64	0.05	5.92	6.02	0.12	7.23	0.49	0.15	< 0.01	0.009	12.16	99.08
190.2	< 0.005	0.01	< 0.003	39.24	8	2.93	0.067	12.61	11.72	0.18	3.08	0.34	0.19	< 0.01	0.009	21.01	99.38
201.64	< 0.005	< 0.005	< 0.003	55	12.84	3.94	0.039	7.32	3.86	0.13	6.59	0.65	0.61	0.01	0.012	9.42	100.4
204.6	< 0.005	0.006	< 0.003	52.91	12.84	3.48	0.058	6.42	5.64	0.12	6.7	0.47	0.13	< 0.01	0.01	11.57	100.4
216.8	< 0.005	< 0.005	0.008	52.93	13.16	6.46	0.046	5.93	3.42	0.11	6.86	0.46	0.14	0.01	0.01	9.93	99.47
220.68	< 0.005	< 0.005	< 0.003	60.04	12.66	4.3	0.037	4.57	2.64	0.13	6.37	0.46	0.1	< 0.01	0.008	7.87	99.19
225.86	0.006	0.01	< 0.003	54.06	14.52	3.15	0.043	4.46	4.33	0.12	7.						

Sample Depth	Co ₃ O ₄	CuO	NiO	SiO ₂	Al ₂ O ₃	Fe ₂ O ₃ (T)	MnO	MgO	CaO	Na ₂ O	K ₂ O	TiO ₂	P ₂ O ₅	Cr ₂ O ₃	V ₂ O ₅	LOI	Total
64.7	< 0.005	< 0.005	< 0.003	66.39	15.3	4.18	0.022	1.95	0.21	0.19	4.38	0.56	0.03	< 0.01	0.008	5.72	98.93
74.25	< 0.005	< 0.005	< 0.003	61.3	20.6	3.2	0.016	1.36	0.15	0.18	4.27	0.9	0.05	0.01	0.016	6.69	98.74
82.1	< 0.005	< 0.005	0.007	60.2	20.85	3.88	0.018	1.56	0.26	0.19	4.65	0.85	0.05	0.02	0.019	6.55	99.1
94.7	< 0.005	< 0.005	0.005	57.09	19.97	7.9	0.039	2.23	0.25	0.18	4.4	0.84	0.05	0.02	0.015	6.58	99.57
96.8	< 0.005	< 0.005	0.01	57.26	21.3	5.65	0.029	1.93	0.3	0.18	4.71	0.86	0.05	0.02	0.017	6.99	99.33
107.62	< 0.005	< 0.005	< 0.003	60.84	18.61	5.86	0.035	2.27	0.36	0.21	4.8	0.66	0.12	0.01	0.015	6.23	100
115.6	< 0.005	0.008	< 0.003	64.03	14.69	6.73	0.041	2.73	0.28	0.18	3.9	0.59	0.07	< 0.01	0.01	5.36	98.61
122.27	< 0.005	< 0.005	0.005	59.36	17.07	9.44	0.067	3.22	0.25	0.19	4.12	0.67	0.05	0.01	0.008	5.71	100.2
185.47	< 0.005	< 0.005	0.012	51.42	22.95	4.06	0.047	3.38	1.37	0.29	7.02	1.1	0.77	0.02	0.014	6.52	98.97
198.85	< 0.005	< 0.005	0.008	60.32	17.73	4.58	0.12	2.68	0.9	0.26	6.3	0.76	0.05	0.02	0.013	6.25	99.99
201.85	< 0.005	< 0.005	< 0.003	58.51	17.82	5.13	0.123	2.69	0.88	0.25	6.31	0.67	0.04	0.02	0.011	6.21	98.66
204.85	< 0.005	< 0.005	< 0.003	57.63	18.37	4.84	0.222	2.89	1.44	0.21	6.3	0.8	0.05	0.02	0.015	7.2	100
211.05	< 0.005	< 0.005	< 0.003	68.49	14.85	3.4	0.074	1.94	0.56	0.2	5.4	0.61	0.04	< 0.01	0.012	4.39	99.96
216.9	< 0.005	< 0.005	0.009	64.83	14.34	6.91	0.047	2.92	0.26	0.16	4.55	0.74	0.04	0.01	0.012	4.28	99.11
225.12	< 0.005	< 0.005	< 0.003	59.29	19.26	4.38	0.023	2.45	0.31	0.21	6.54	0.73	0.05	0.02	0.016	5.46	98.72
239.02	< 0.005	< 0.005	< 0.003	45	16.59	3.35	0.062	2.21	11.62	0.27	5.83	0.6	0.05	0.01	0.015	14.12	99.73
243.14	< 0.005	< 0.005	< 0.003	58.32	20.75	4.2	0.007	1.86	0.17	0.33	7.64	0.72	0.05	0.01	0.021	6.1	100.2
251.1	< 0.005	< 0.005	< 0.003	59.97	19.39	5.21	0.01	1.82	0.16	0.31	7.41	0.71	0.05	0.01	0.014	4.84	99.9
259	< 0.005	< 0.005	< 0.003	58.05	19.56	4.63	0.026	2.03	0.61	0.31	7.37	0.72	0.07	0.01	0.015	5.71	99.12
271.28	< 0.005	< 0.005	< 0.003	59.43	18.49	5.88	0.011	1.68	0.16	0.29	7.05	0.75	0.06	0.01	0.019	4.78	98.63
292.73	< 0.005	< 0.005	< 0.003	50.91	14.77	4.4	0.196	4.66	5.42	0.24	5.61	0.62	0.08	0.01	0.007	11.69	98.62
319.08	< 0.005	< 0.005	< 0.003	58.92	20.31	4.63	0.006	1.74	0.18	0.27	7.33	0.61	0.09	0.01	0.017	4.68	98.79
323.2	< 0.005	< 0.005	0.007	56.95	21.69	3.99	0.004	1.76	0.16	0.12	7.73	0.57	0.08	0.02	0.019	5.68	98.78
330.08	< 0.005	< 0.005	0.005	56.24	21.32	4.92	0.008	2	0.41	0.29	7.94	0.63	0.14	0.01	0.018	5.8	99.73
342.3	< 0.005	< 0.005	< 0.003	56.94	22.5	3.86	0.004	1.8	0.12	0.25	7.39	0.68	0.06	< 0.01	0.02	5.56	99.19

Table A17. Major element geochemistry recorded in weight % for drill core 99VRNTGSDD2 from the Birrindudu Basin.

B. Raw Data: Major Element Geochemistry

	Co3O4	CuO	NiO	SiO2	Al2O3	Fe2O3(T)	MnO	MgO	CaO	Na2O	K2O	TiO2	P2O5	Cr2O3	V2O5
AN-G Meas				46.78	29.93	3.38	0.04	1.89	16.36	1.72	0.14	0.23	0.02	0.01	0.01
AN-G Cert				46.30	29.80	3.36	0.04	1.79	15.90	1.63	0.13	0.22	0.01	0.01	0.01
% Error				1.04	0.44	0.60	7.50	5.59	2.89	5.52	7.69	4.55	100.00	0.00	8.33
FK-N Meas				65.22	18.60	0.06	< 0.0001		0.14	2.57	12.91	0.01	0.02		
FK-N Cert				65.00	18.60	0.09	0.01		0.11	2.58	12.80	0.02	0.02		
% Error				0.34	0.00	33.33	90.00		27.27	0.39	0.86	50.00	16.67		
BE-N Meas	0.01	0.01	0.03	38.04	9.99	13.00	0.20	13.10	14.05	3.10	1.36	2.66	1.09	0.04	0.04
BE-N Cert	0.01	0.01	0.03	38.20	10.10	12.80	0.20	13.10	13.90	3.18	1.39	2.61	1.05	0.05	0.04
% Error	12.50	11.11	14.71	0.42	1.09	1.56	0.00	0.00	1.08	2.52	2.16	1.92	3.81	20.00	11.90
DR-N Meas				52.27	17.21	9.72	0.22	4.28	6.96	2.95	1.69	1.06	0.24		
DR-N Cert				52.85	17.52	9.70	0.22	4.40	7.05	2.99	1.70	1.09	0.25		
% Error				1.10	1.77	0.21	2.27	2.73	1.28	1.34	0.59	2.75	4.00		
GBW 07238 (NCS DC 70006) Meas				34.06	3.47	22.14	1.40	0.91	31.12	0.09	0.02	0.13			
GBW 07238 (NCS DC 70006) Cert				34.10	3.46	21.30	1.40	0.86	31.40	0.08	0.05	0.13			
% Error				0.12	0.29	3.94	0.14	5.81	0.89	20.00	56.52	0.00			
GS-N Meas				65.97	14.67	3.77	0.05	2.20	2.49	3.84	4.70	0.69	0.30		
GS-N Cert				65.80	14.67	3.75	0.06	2.30	2.50	3.77	4.63	0.68	0.28		
% Error				0.26	0.00	0.53	14.29	4.35	0.40	1.86	1.51	1.47	7.14		
PM-S Meas				46.80	17.03	10.19	0.16	9.38	12.52	2.09	0.14	1.12	0.03		
PM-S Cert				47.00	17.15	10.10	0.16	9.34	12.48	2.08	0.14	1.10	0.03		
% Error				0.43	0.70	0.89	1.88	0.43	0.32	0.48	0.00	1.82	0.00		
WS-E Meas				51.34	13.78	13.41	0.18	5.62	9.12	2.52	1.01	2.46	0.31		
WS-E Cert				50.70	13.78	13.15	0.17	5.55	8.95	2.47	1.00	2.40	0.30		
% Error				1.26	0.00	1.98	2.94	1.26	1.90	2.02	1.00	2.50	3.33		
NCS DC19014 Meas				3.20	2.65	75.90	0.34	3.80	0.42			11.81		1.79	0.60
NCS DC19014 Cert				3.27	2.57	77.11	0.34	3.81	0.42			11.85		1.88	0.56
% Error				2.14	3.11	1.57	2.69	0.26	0.24			0.34		4.79	7.14
AMIS 0563 (XRF) Meas				8.31	0.87	37.04	0.19	10.55	21.21			1.32	7.43		
AMIS 0563 (XRF) Cert				8.46	0.76	37.09	0.19	10.90	21.08			1.33	7.44		
% Error				1.77	14.47	0.13	2.69	3.21	0.62			0.75	0.13		
BR-1 112.92 Orig	0.01	< 0.005	< 0.003	44.99	27.46	11.10	0.03	1.21	0.22	0.19	6.33	1.24	0.08	0.01	0.02
BR-1 112.92 Meas	0.01	< 0.005	< 0.003	44.99	27.46	11.10	0.03	1.21	0.22	0.19	6.33	1.24	0.08	0.01	0.02
% Error	0.00	0.00	0.00	0.00	0.00	0.00	0.00	0.00	0.00	0.00	0.00	0.00	0.00	0.00	0.00
BR-1 493.64 Orig	< 0.005	< 0.005	< 0.003	40.92	13.81	3.19	0.12	7.67	9.73	0.17	5.40	0.47	0.13	< 0.01	0.01
BR-1 493.64 Meas	< 0.005	< 0.005	< 0.003	40.92	13.81	3.19	0.12	7.67	9.73	0.17	5.40	0.47	0.13	< 0.01	0.01
% Error	0.00	0.00	0.00	0.00	0.00	0.00	0.00	0.00	0.00	0.00	0.00	0.00	0.00	0.00	0.00
MCDD3 335.9 Orig	< 0.005	< 0.005	< 0.003	60.74	19.32	3.71	0.01	1.89	0.28	0.14	8.02	0.82	0.17	0.02	0.02
MCDD3 335.9 Meas	< 0.005	< 0.005	< 0.003	60.74	19.32	3.71	0.01	1.89	0.28	0.14	8.02	0.82	0.17	0.02	0.02
% Error	0.00	0.00	0.00	0.00	0.00	0.00	0.00	0.00	0.00	0.00	0.00	0.00	0.00	0.00	0.00
McA5 86.4 Orig	< 0.005	0.01	< 0.003	35.82	5.95	2.51	0.07	10.47	15.74	0.15	2.60	0.23	0.16	< 0.01	0.01
McA5 86.4 Meas	< 0.005	0.01	< 0.003	35.82	5.95	2.51	0.07	10.47	15.74	0.15	2.60	0.23	0.16	< 0.01	0.01
% Error	0.00	0.00	0.00	0.00	0.00	0.00	0.00	0.00	0.00	0.00	0.00	0.00	0.00	0.00	0.00
99NT 319.08 Orig	< 0.005	< 0.005	< 0.003	58.92	20.31	4.63	0.01	1.74	0.18	0.27	7.33	0.61	0.09	0.01	0.02
99NT 319.08 Meas	< 0.005	< 0.005	< 0.003	58.92	20.31	4.63	0.01	1.74	0.18	0.27	7.33	0.61	0.09	0.01	0.02
% Error	0.00	0.00	0.00	0.00	0.00	0.00	0.00	0.00	0.00	0.00	0.00	0.00	0.00	0.00	0.00
GSD7 700.3 Orig	< 0.005	< 0.005	< 0.003	60.41	15.01	4.48	0.04	2.71	4.00	0.16	5.74	0.58	0.19	< 0.01	0.02
GSD7 700.3 Meas	< 0.005	< 0.005	< 0.003	60.41	15.01	4.48	0.04	2.71	4.00	0.16	5.74	0.58	0.19	< 0.01	0.02
% Error	0.00	0.00	0.00	0.00	0.00	0.00	0.00	0.00	0.00	0.00	0.00	0.00	0.00	0.00	0.00

Table A18. Reference materials and sample duplicates with associated % error for major element geochemical analyses.

C. Correlation of Major Elements

	% N	% TOC	Fe-Py / FeHR	FeHR/FeT	Co3O4	CuO	NiO	SiO2	Al2O3	Fe2O3(T)	MnO	MgO	CaO	Na2O	K2O	TiO2	P2O5	Cr2O3	V2O5	
% N	1.00																			
% TOC	0.57	1.00																		
Fe-	0.18	0.48	1.00																	
Py/FeHR				1.00																
FeHR/FeT	0.01	0.44	0.47	1.00																
Co3O4	0.03	0.07	0.08	0.16	1.00															
CuO	-0.12	0.00	0.06	0.07	0.24	1.00														
NiO	0.07	0.13	0.12	0.03	0.24	-0.03	1.00													
SiO2	-0.03	-0.14	-0.03	-0.43	-0.04	-0.07	0.04	1.00												
Al2O3	0.25	-0.32	-0.28	-0.67	-0.10	-0.12	-0.03	0.39	1.00											
Fe2O3(T)	0.32	-0.02	-0.13	-0.30	0.10	0.00	0.12	0.18	0.31	1.00										
MnO	-0.14	-0.04	-0.14	0.27	0.08	0.12	0.03	-0.51	-0.41	0.07	1.00									
MgO	-0.26	0.03	0.08	0.56	0.08	0.10	-0.02	-0.71	-0.72	-0.27	0.49	1.00								
CaO	-0.04	0.30	0.12	0.57	0.04	0.07	-0.05	-0.84	-0.73	-0.36	0.48	0.69	1.00							
Na2O	0.36	-0.08	-0.06	-0.09	0.17	-0.14	0.00	0.09	0.16	-0.02	-0.20	-0.10	-0.09	1.00						
K2O	-0.27	-0.25	0.02	-0.30	-0.06	0.11	0.01	0.28	0.52	-0.16	-0.30	-0.44	-0.50	-0.22	1.00					
TiO2	0.26	-0.27	-0.25	-0.53	-0.08	-0.16	0.03	0.31	0.88	0.30	-0.33	-0.61	-0.63	0.18	0.40	1.00				
P2O5	-0.07	0.26	0.26	0.18	0.04	-0.02	0.17	-0.15	-0.22	-0.10	0.12	0.20	0.18	-0.27	-0.03	-0.06	1.00			
Cr2O3	0.05	-0.07	-0.18	-0.19	0.05	-0.07	0.56	0.11	0.25	0.04	-0.02	-0.16	-0.20	0.01	0.17	0.30	0.04	1.00		
V2O5	0.14	0.05	0.04	-0.29	0.04	0.15	0.21	0.07	0.43	0.31	-0.14	-0.29	-0.32	-0.04	0.41	0.48	0.05	0.25	1.00	

Table A19. Correlation coefficients of major element oxides as well as highly reactive iron ratios and TOC for the entire Greater McArthur Basin.